

University of Windsor

## Scholarship at UWindor

---

Electronic Theses and Dissertations

Theses, Dissertations, and Major Papers

---

2008

### Doubly-fed induction generator used in wind energy

Hany M. Jabr Soloumah  
*University of Windsor*

Follow this and additional works at: <https://scholar.uwindsor.ca/etd>

---

#### Recommended Citation

Soloumah, Hany M. Jabr, "Doubly-fed induction generator used in wind energy" (2008). *Electronic Theses and Dissertations*. 8103.

<https://scholar.uwindsor.ca/etd/8103>

This online database contains the full-text of PhD dissertations and Masters' theses of University of Windsor students from 1954 forward. These documents are made available for personal study and research purposes only, in accordance with the Canadian Copyright Act and the Creative Commons license—CC BY-NC-ND (Attribution, Non-Commercial, No Derivative Works). Under this license, works must always be attributed to the copyright holder (original author), cannot be used for any commercial purposes, and may not be altered. Any other use would require the permission of the copyright holder. Students may inquire about withdrawing their dissertation and/or thesis from this database. For additional inquiries, please contact the repository administrator via email ([scholarship@uwindsor.ca](mailto:scholarship@uwindsor.ca)) or by telephone at 519-253-3000ext. 3208.

# Doubly-Fed Induction Generator Used in Wind Energy

By

Hany M. Jabr Soloumah

A Dissertation

Submitted to the Faculty of Graduate Studies

through Electrical Engineering

in Partial Fulfillment of the Requirements for

the Degree of Doctor of Philosophy at the

University of Windsor

Windsor, Ontario, Canada

2008

© 2008 Hany M. Jabr Soloumah



Library and  
Archives Canada

Bibliothèque et  
Archives Canada

Published Heritage  
Branch

Direction du  
Patrimoine de l'édition

395 Wellington Street  
Ottawa ON K1A 0N4  
Canada

395, rue Wellington  
Ottawa ON K1A 0N4  
Canada

*Your file    Votre référence*

*ISBN: 978-0-494-47106-7*

*Our file    Notre référence*

*ISBN: 978-0-494-47106-7*

#### NOTICE:

The author has granted a non-exclusive license allowing Library and Archives Canada to reproduce, publish, archive, preserve, conserve, communicate to the public by telecommunication or on the Internet, loan, distribute and sell theses worldwide, for commercial or non-commercial purposes, in microform, paper, electronic and/or any other formats.

The author retains copyright ownership and moral rights in this thesis. Neither the thesis nor substantial extracts from it may be printed or otherwise reproduced without the author's permission.

#### AVIS:

L'auteur a accordé une licence non exclusive permettant à la Bibliothèque et Archives Canada de reproduire, publier, archiver, sauvegarder, conserver, transmettre au public par télécommunication ou par l'Internet, prêter, distribuer et vendre des thèses partout dans le monde, à des fins commerciales ou autres, sur support microforme, papier, électronique et/ou autres formats.

L'auteur conserve la propriété du droit d'auteur et des droits moraux qui protège cette thèse. Ni la thèse ni des extraits substantiels de celle-ci ne doivent être imprimés ou autrement reproduits sans son autorisation.

---

In compliance with the Canadian Privacy Act some supporting forms may have been removed from this thesis.

Conformément à la loi canadienne sur la protection de la vie privée, quelques formulaires secondaires ont été enlevés de cette thèse.

While these forms may be included in the document page count, their removal does not represent any loss of content from the thesis.

Bien que ces formulaires aient inclus dans la pagination, il n'y aura aucun contenu manquant.



# Canada

## **Author's Declaration of Originality**

I hereby certify that I am the sole author of this thesis and that parts of this thesis have been published or submitted for publication. I also certify that I have the right to use all or part of the published work in other work.

I certify that, to the best of my knowledge, my thesis does not infringe upon anyone's copyright nor violate any proprietary rights and that any ideas, techniques, quotations, or any other material from the work of other people included in my thesis, published or otherwise, are fully acknowledged in accordance with the standard referencing practices.

I declare that this is a true copy of my thesis, including any final revisions, as approved by my thesis committee and the Graduate Studies office, and that this thesis has not been submitted for a higher degree to any other University or Institution.

## **Abstract**

Wound-rotor induction generator has numerous advantages in wind power generation over other generators. One scheme for wound-rotor induction generator is realized when a converter cascade is used between the slip-ring terminals and the utility grid to control the rotor power. This configuration is called the doubly-fed induction generator (DFIG). In this work, a novel induction machine model is developed. This model includes the saturation in the main and leakage flux paths. It shows that the model which considers the saturation effects gives more realistic results. A new technique, which was developed for synchronous machines, was applied to experimentally measure the stator and rotor leakage inductance saturation characteristics on the induction machine.

A vector control scheme is developed to control the rotor side voltage-source converter. Vector control allows decoupled or independent control of both active and reactive power of DFIG. These techniques are based on the theory of controlling the d- and q- axes components of voltage or current in different reference frames. In this work, the stator flux oriented rotor current control, with decoupled control of active and reactive power, is adopted. This scheme allows the independent control of the generated active and reactive power as well as the rotor speed to track the maximum wind power point. Conventionally, the controller type used in vector controllers is of the PI type with a fixed proportional and integral gain. In this work, different intelligent schemes by which the controller can change its behavior are proposed. The first scheme is an adaptive gain scheduler which utilizes different characteristics to generate the variation in the proportional and the integral gains. The second scheme is a fuzzy logic gain scheduler and the third is a neuro-fuzzy controller. The transient responses using the above mentioned schemes are compared analytically and experimentally. It has been found that although the fuzzy logic and neuro-fuzzy schemes are more complicated and have many parameters; this complication provides a higher degree of freedom in tuning the controller which is evident in giving much better system performance. Finally, the simulation results were experimentally verified by building the experimental setup and implementing the developed control schemes.

**Dedication**

*To My Parents*

*&*

*My Wife*

## **Acknowledgement**

I owe so many thanks, first of all, I thank god for giving me the patience and enthusiasm to get my dissertation to its final form.

I would like to express my gratitude and appreciation to all those who helped and inspired me in various ways to start, continue and complete this dissertation.

My special thanks go to Dr. Kar, my advisor, for his continuance guidance and support, Dr. Sid-Ahmed for his support and advice. I would like to thank my doctoral committee for their valuable suggestions and comments.

I also would like to thank my master's advisors Dr. Ashraf Megahed, Dr. Fathy Mabrouk and Dr. Mahmoud Elbakry for believing in me and their continued support and encouragement. Special thanks to Dr. Ashraf Megahed as he inspired me and taught me all the skills I need to succeed.

Special thanks go to my father, mother, brother and sister for their constant love and prayers which made this journey possible. Their continuance encouragement and support kept me focused even in the toughest moments.

My special appreciation goes to my wife for her support, patience, prayers and sacrifice throughout all the rough times to achieve this goal.

# Table of Contents

<b>AUTHOR'S DECLARATION OF ORIGINALITY .....</b>	<b>III</b>
<b>ABSTRACT .....</b>	<b>IV</b>
<b>DEDICATION .....</b>	<b>V</b>
<b>ACKNOWLEDGEMENT .....</b>	<b>VI</b>
<b>LIST OF FIGURES.....</b>	<b>X</b>
<b>LIST OF TABLES.....</b>	<b>XIV</b>
<b>NOMENCLATURE .....</b>	<b>XV</b>
<b>1 INTRODUCTION .....</b>	<b>1</b>
1.1 BACKGROUND .....	1
1.2 GENERATORS USED IN WIND ENERGY .....	2
1.2.1 DC Generators .....	2
1.2.2 Synchronous Generators .....	3
1.2.3 Induction Generators .....	4
1.3 DOUBLY-FED MACHINES AND APPLICATIONS .....	4
1.4 RESEARCH OBJECTIVES .....	6
1.5 DISSERTATION OUTLINE .....	7
1.6 REFERENCES .....	8
<b>2 INDUCTION GENERATORS USED IN WIND POWER.....</b>	<b>9</b>
2.1 FIXED SPEED AND VARIABLE SPEED WIND TURBINES .....	10
2.2 DOUBLY-FED INDUCTION GENERATOR IN WIND POWER .....	13
2.3 REFERENCES .....	14
<b>3 INDUCTION MACHINE MODELING .....</b>	<b>17</b>
3.1 INTRODUCTION .....	17
3.2 STEADY-STATE INDUCTION MACHINE MODEL .....	18
3.3 INDUCTION MACHINE DYNAMIC MODEL .....	21
3.4 SATURATION IN INDUCTION MACHINE .....	25
3.4.1 Main flux saturation .....	26
3.4.2 Leakage flux saturation.....	26
3.5 EXPERIMENTAL DETERMINATION OF MACHINE PARAMETERS AND SATURATION	
CHARACTERISTICS .....	26
3.5.1 Unsaturated machine parameters .....	26



3.5.2	<i>Main flux saturation characteristics</i>	28
3.5.3	<i>Stator and rotor leakage flux saturation characteristics</i>	29
3.6	REFERENCES	34
<b>4</b>	<b>FIELD ORIENTATION CONTROL</b>	<b>37</b>
4.1	INTRODUCTION	37
4.2	VECTOR CONTROL OF DFIG	41
4.3	CONTROL OF LINE SIDE CONVERTER	42
4.4	STRUCTURE OF IMPLEMENTATION	44
4.5	REFERENCES	45
<b>5</b>	<b>ADAPTIVE CONTROLLER</b>	<b>47</b>
5.1	INTRODUCTION	47
5.2	ADAPTIVE PI GAIN SCHEDULER	48
5.3	IMPLEMENTATION OF THE ADAPTIVE PI GAIN SCHEDULER	50
5.4	SIMULATION AND RESULTS	53
5.5	REFERENCES	57
<b>6</b>	<b>FUZZY LOGIC CONTROLLER</b>	<b>58</b>
6.1	INTRODUCTION	58
6.2	OVERVIEW ON FUZZY LOGIC	58
6.2.1	<i>Membership functions</i>	58
6.2.2	<i>Logical operations</i>	60
6.2.3	<i>If-then rules</i>	61
6.3	FUZZY INFERENCE SYSTEM	62
6.3.1	<i>Step 1: Fuzzify inputs</i>	62
6.3.2	<i>Apply fuzzy operator</i>	63
6.3.3	<i>Apply implication method</i>	63
6.3.4	<i>Aggregate all outputs</i>	63
6.3.5	<i>Defuzzify</i>	64
6.4	IMPLEMENTATION OF FUZZY GAIN SCHEDULER	64
6.4.1	<i>System configuration</i>	69
6.5	SIMULATION AND RESULTS	71
6.6	REFERENCES	76
<b>7</b>	<b>NEURO-FUZZY CONTROL SYSTEM</b>	<b>80</b>
7.1	INTRODUCTION	80
7.1.1	<i>Mamdani fuzzy model</i>	80
7.1.2	<i>Sugeno fuzzy mode l</i>	81

7.2 ANFIS ARCHITECTURE .....	83
7.3 HYBRID LEARNING ALGORITHM .....	86
7.4 IMPLEMENTATION OF NEURO-FUZZY GAIN SCHEDULER .....	87
7.5 SIMULATION AND RESULTS .....	92
7.6 SIMULATION AND RESULTS FOR ANOTHER SYSTEM .....	96
7.7 REFERENCES .....	102
<b>8 EXPERIMENTAL SETUP AND SYSTEM IMPLEMENTATION.....</b>	<b>104</b>
8.1 INTRODUCTION .....	104
8.2 DETERMINATION OF MACHINE PARAMETERS .....	104
8.2.1 <i>DC test results</i> .....	105
8.2.2 <i>No load test results</i> .....	105
8.2.3 <i>Locked rotor test results</i> .....	106
8.2.4 <i>Main flux saturation characteristic</i> .....	107
8.2.5 <i>Stator and rotor leakage flux saturation characteristic</i> .....	108
8.3 POWER ELECTRONICS SYSTEM COMPONENTS .....	109
8.3.1 <i>The microprocessor or microcontroller</i> .....	111
8.3.2 <i>The isolation</i> .....	119
8.3.3 <i>The power electronic components</i> .....	121
8.3.4 <i>Gate drivers</i> .....	125
8.3.5 <i>Feedback</i> .....	128
8.4 PUTTING IT ALL TOGETHER .....	133
8.5 EXPERIMENTAL RESULTS .....	138
8.6 REFERENCES .....	146
<b>9 CONCLUSION AND FUTURE WORK.....</b>	<b>147</b>
9.1 CONCLUSION .....	147
9.2 FUTURE WORK .....	148
<b>10 VITA AUCTORIS.....</b>	<b>149</b>

## List of Figures

FIG. 2.1: ROTOR POWER COEFFICIENT VERSUS TIP-SPEED RATIO HAS A SINGLE MAXIMUM.....	10
FIG. 2.2: WIND TURBINE POWER FOR DIFFERENT WIND SPEEDS SHOWING MAXIMUM POWER POINT CURVE. .	11
FIG. 2.3: DIFFERENT CONFIGURATIONS FOR WIND-DRIVEN INDUCTION GENERATORS. ....	13
FIG. 3.1: STATOR SIDE OF THE PER-PHASE EQUIVALENT CIRCUIT OF A THREE-PHASE INDUCTION MACHINE. .	18
FIG. 3.2: ROTOR SIDE OF THE PER-PHASE EQUIVALENT CIRCUIT OF A THREE-PHASE INDUCTION MACHINE. ..	19
FIG. 3.3: ROTOR SIDE OF THE INDUCTION MACHINE WITH ADJUSTMENT. ....	19
FIG. 3.4: PER-PHASE EQUIVALENT CIRCUIT OF THREE-PHASE INDUCTION MACHINE NEGLECTING CORE LOSS.	20
FIG. 3.5: PER-PHASE EQUIVALENT CIRCUIT OF THREE-PHASE INDUCTION MACHINE INCLUDING CORE LOSS. .	20
FIG. 3.6: D-Q AXIS REPRESENTATION OF INDUCTION MACHINE. ....	21
FIG. 3.7: EQUIVALENT CIRCUITS OF THE INDUCTION MACHINE IN AN ARBITRARY ROTATING REFERENCE FRAME. ....	23
FIG. 3.8: EQUIVALENT CIRCUITS OF THE INDUCTION GENERATOR IN A SYNCHRONOUSLY ROTATING REFERENCE FRAME.....	24
FIG. 3.9: EXPERIMENTAL SETUP FOR DETERMINING THE INDUCTION MACHINE PARAMETERS. ....	27
FIG. 3.10: MEASURED MAIN FLUX SATURATION CHARACTERISTICS.....	29
FIG. 3.11: DETERMINATION OF THE LEAKAGE REACTANCE.....	30
FIG. 3.12: PHASOR DIAGRAM OF AN UNLOADED UNEXCITED SYNCHRONOUS MACHINE. ....	32
FIG. 3.13: THE FLOWCHART OF THE PROGRAM USED FOR CALCULATING THE LEAKAGE REACTANCE OF WOUND-ROTOR INDUCTION MACHINE. ....	33
FIG. 3.14: MEASURED LEAKAGE REACTANCE SATURATION CHARACTERISTICS. ....	33
FIG. 4.1: PHASOR DIAGRAM OF THE VECTOR CONTROLLER.....	40
FIG. 4.2: DOUBLY-FED INDUCTION GENERATOR.....	43
FIG. 4.3: VECTOR CONTROLLER IMPLEMENTATION OF THE DOUBLY-FED INDUCTION GENERATOR.....	45
FIG. 5.1: AUTO TUNING ADAPTIVE CONTROLLER.....	47
FIG. 5.2: SELF TUNING ADAPTIVE CONTROLLER. ....	48
FIG. 5.3: WIND-DRIVEN DFIG SYSTEM CONFIGURATION. ....	51
FIG. 5.4: WIND TURBINE POWER FOR DIFFERENT WIND SPEEDS SHOWING MAXIMUM POWER POINT CURVE. .	51
FIG. 5.5: VECTOR CONTROL CONFIGURATION FOR SLIP ENERGY RECOVERY USING THE PI GAIN SCHEDULER.	52
FIG. 5.6: PI GAIN SCHEDULER CHARACTERISTICS. (A) PROPORTIONAL GAIN ( $K_p$ ). (B) INTEGRAL GAIN ( $K_i$ )...	54
FIG. 5.7: SYSTEM SPEED RESPONSE USING THE PROPOSED ADAPTIVE CONTROLLER COMPARED TO FIXED PI CONTROLLERS.....	55
FIG. 5.8: STATOR ACTIVE AND REACTIVE POWER GENERATED. ....	55
FIG. 5.9: D- AND Q- AXIS ROTOR CURRENT COMPONENTS. ....	56
FIG. 5.10: ROTOR ACTIVE AND REACTIVE POWER FLOW. ....	56
FIG. 6.1: TRIANGULAR AND TRAPEZOIDAL MEMBERSHIP FUNCTIONS.....	59

FIG. 6.2: GAUSSIAN, TWO-SIDED COMPOSITE GAUSSIAN AND GENERALIZED BELL MEMBERSHIP FUNCTIONS.	59
FIG. 6.3: SIGMOIDAL BASED MEMBERSHIP FUNCTIONS. ....	60
FIG. 6.4: Z, S AND PI MEMBERSHIP FUNCTIONS. ....	60
FIG. 6.5: GRAPHIC INTERPRETATION OF THE FUZZY LOGIC OPERATIONS. ....	61
FIG. 6.6: FUZZY PI GAIN SCHEDULER. ....	66
FIG. 6.7: MEMBERSHIP FUNCTIONS FOR THE SPEED ERROR INPUT. ....	66
FIG. 6.8: MEMBERSHIP FUNCTIONS FOR THE ACTIVE AND REACTIVE POWER ERROR INPUTS. ....	66
FIG. 6.9: MEMBERSHIP FUNCTIONS FOR THE PROPORTIONAL GAIN, $K_p$ OF THE SPEED CONTROLLER. ....	67
FIG. 6.10: MEMBERSHIP FUNCTIONS FOR THE INTEGRAL GAIN, $K_i$ OF THE SPEED CONTROLLER. ....	67
FIG. 6.11: MEMBERSHIP FUNCTIONS FOR $K_p$ OF THE ACTIVE AND REACTIVE POWER CONTROLLERS. ....	67
FIG. 6.12: MEMBERSHIP FUNCTIONS FOR $K_i$ OF THE ACTIVE AND REACTIVE POWER CONTROLLERS. ....	68
FIG. 6.13: PROPORTIONAL AND INTEGRAL GAINS VS. ERROR FOR THE SPEED CONTROLLER. ....	68
FIG. 6.14: PROPORTIONAL AND INTEGRAL GAINS VS. ERROR FOR THE ACTIVE AND REACTIVE POWER CONTROLLERS. ....	69
FIG. 6.15: VECTOR CONTROL CONFIGURATION USING THE PROPOSED FUZZY PI GAIN SCHEDULER. ....	70
FIG. 6.16: SPEED RESPONSE FOR SUB-SYNCHRONOUS OPERATION. ....	71
FIG. 6.17: STATOR ACTIVE POWER FOR SUB-SYNCHRONOUS OPERATION. ....	72
FIG. 6.18: STATOR REACTIVE POWER FOR SUB-SYNCHRONOUS OPERATION. ....	72
FIG. 6.19: D-AXIS ROTOR CURRENT FOR SUB-SYNCHRONOUS OPERATION. ....	73
FIG. 6.20: Q-AXIS ROTOR CURRENT FOR SUB-SYNCHRONOUS OPERATION. ....	73
FIG. 6.21: ROTOR ACTIVE POWER FOR SUB-SYNCHRONOUS OPERATION. ....	74
FIG. 6.22: ROTOR REACTIVE POWER FOR SUB-SYNCHRONOUS OPERATION. ....	74
FIG. 6.23: SPEED RESPONSE FOR SUPER-SYNCHRONOUS OPERATION. ....	75
FIG. 6.24: ROTOR ACTIVE POWER FOR SUPER-SYNCHRONOUS OPERATION. ....	75
FIG. 7.1: THE MAMDANI FUZZY INFERENCE SYSTEM USING MIN AND MAX FOR T-NORM AND T-CONORM OPERATORS RESPECTIVELY. ....	81
FIG. 7.2: THE SUGENO FUZZY MODEL. ....	82
FIG. 7.3: A-TWO INPUT FIRST-ORDER SUGENO FUZZY MODEL WITH TWO RULES. ....	83
FIG. 7.4: EQUIVALENT ANFIS ARCHITECTURE. ....	83
FIG. 7.5: ANFIS ARCHITECTURE FOR THE SUGENO FUZZY MODEL, WHERE WEIGHT NORMALIZATION IS PERFORMED AT THE VERY LAST LAYER. ....	85
FIG. 7.6: ANFIS ARCHITECTURE FOR A TWO-INPUT SUGENO FUZZY MODEL WITH NINE RULES. ....	85
FIG. 7.7: THE INPUT SPACE THAT ARE PARTITIONED INTO NINE FUZZY REGIONS. ....	86
FIG. 7.8: SIMPLE STRUCTURE OF A SINGLE UNIT OF THE NEURO-FUZZY GAIN SCHEDULER. ....	88
FIG. 7.9: THE TRAINING ERROR FOR THE SPEED NEURO-FUZZY GAIN TUNER. ....	89
FIG. 7.10: INPUT MEMBERSHIP FUNCTIONS FOR THE PROPORTIONAL GAIN TUNERS. (A) ACTIVE POWER CONTROLLER. (B) SPEED CONTROLLER. ....	89

FIG. 7.11: NEURO-FUZZY GAIN SCHEDULER FOR VECTOR CONTROL OF WIND DRIVEN DFIG. ....	91
FIG. 7.12: SYSTEM SPEED RESPONSE. ....	93
FIG. 7.13: STATOR POWER. (A) ACTIVE POWER. (B) REACTIVE POWER. ....	94
FIG. 7.14: ROTOR CURRENTS. (A) D- AXIS ROTOR CURRENT. (B) Q- AXIS ROTOR CURRENT. ....	95
FIG. 7.15: SPEED RESPONSE FOR SUB-SYNCHRONOUS OPERATION. ....	97
FIG. 7.16: STATOR CURRENT FOR SUB-SYNCHRONOUS OPERATION. ....	97
FIG. 7.17: ROTOR LINE VOLTAGE FOR SUB-SYNCHRONOUS OPERATION. ....	98
FIG. 7.18: ROTOR PHASE VOLTAGE FOR SUB-SYNCHRONOUS OPERATION. ....	98
FIG. 7.19: ROTOR CURRENT FOR SUB-SYNCHRONOUS OPERATION. ....	99
FIG. 7.20: SPEED RESPONSE FOR SUPER-SYNCHRONOUS OPERATION. ....	99
FIG. 7.21: STATOR CURRENT FOR SUPER-SYNCHRONOUS OPERATION. ....	100
FIG. 7.22: ROTOR LINE VOLTAGE FOR SUPER-SYNCHRONOUS OPERATION. ....	100
FIG. 7.23: ROTOR PHASE VOLTAGE FOR SUPER-SYNCHRONOUS OPERATION. ....	101
FIG. 7.24: ROTOR CURRENT FOR SUPER-SYNCHRONOUS OPERATION. ....	101
FIG. 8.1: DFIG COUPLED TO THE DC MOTOR IN THE EXPERIMENTAL SETUP. ....	105
FIG. 8.2: MAIN FLUX SATURATION CHARACTERISTIC. ....	107
FIG. 8.3: STATOR LEAKAGE FLUX SATURATION CHARACTERISTIC. ....	108
FIG. 8.4: ROTOR LEAKAGE FLUX SATURATION CHARACTERISTIC. ....	109
FIG. 8.5: POWER ELECTRONICS SYSTEM SHOWING THE INTERACTION BETWEEN VARIOUS SUBSYSTEMS. ...	110
FIG. 8.6: MICROCONTROLLER BASED CONTROL SYSTEM. ....	111
FIG. 8.7: POWER ELECTRONICS CONVERTER. ....	112
FIG. 8.8: QUADRATURE ENCODER OUTPUT SIGNAL. ....	113
FIG. 8.9: PIC®18F4431 MODULES. ....	117
FIG. 8.10: OPTO-COUPLER PIN AND INTEGRAL CONNECTION DIAGRAM. ....	120
FIG. 8.11: MOSFET AND IGBT TURN-OFF BEHAVIOR. ....	123
FIG. 8.12: MOSFET AND IGBT OPERATING RANGE. ....	123
FIG. 8.13: SHUNT RESISTORS AS CURRENT FEEDBACK SENSORS. ....	130
FIG. 8.14: SIMPLIFIED BLOCK DIAGRAM OF QUADRATURE ENCODER. ....	132
FIG. 8.15: SCHEMATIC OF THE DEVELOPED POWER ELECTRONIC CONVERTER. ....	134
FIG. 8.16: PCB LAYOUT OF THE DEVELOPED POWER ELECTRONIC CONVERTER. ....	135
FIG. 8.17: COMPLETED POWER ELECTRONIC CONVERTER. ....	136
FIG. 8.18: PWM COMPLEMENTARY OUTPUT. ....	137
FIG. 8.19: PWM OUTPUTS SHIFTED 120°. ....	137
FIG. 8.20: OUTPUT LINE VOLTAGE FOR RESISTIVE LOAD. ....	138
FIG. 8.21: OUTPUT PHASE VOLTAGE FOR RESISTIVE LOAD. ....	138
FIG. 8.22: SPEED RESPONSE FOR SUB-SYNCHRONOUS OPERATION. ....	140
FIG. 8.23: STATOR CURRENT FOR SUB-SYNCHRONOUS OPERATION. ....	141

FIG. 8.24: ROTOR LINE VOLTAGE FOR SUB-SYNCHRONOUS OPERATION. ....	141
FIG. 8.25: ROTOR PHASE VOLTAGE FOR SUB-SYNCHRONOUS OPERATION. ....	142
FIG. 8.26: ROTOR CURRENT FOR SUB-SYNCHRONOUS OPERATION. ....	142
FIG. 8.27: SPEED RESPONSE FOR SUPER-SYNCHRONOUS OPERATION. ....	143
FIG. 8.28: STATOR CURRENT FOR SUPER-SYNCHRONOUS OPERATION. ....	144
FIG. 8.29: ROTOR LINE VOLTAGE FOR SUPER-SYNCHRONOUS OPERATION. ....	145
FIG. 8.30: ROTOR PHASE VOLTAGE FOR SUPER-SYNCHRONOUS OPERATION. ....	145
FIG. 8.31: ROTOR CURRENT FOR SUPER-SYNCHRONOUS OPERATION. ....	146

## List of Tables

TABLE 3.1: PARAMETERS OF THE WOUND-ROTOR INDUCTION MOTOR USED IN THE INVESTIGATIONS .....	28
TABLE 5.1: DFIG PARAMETERS USED IN THE SIMULATION .....	50
TABLE 6.1: TRUTH TABLES FOR FUZZY LOGICAL OPERATIONS. ....	61
TABLE 6.2: FUZZY RULES FOR THE PROPOSED PI GAIN SCHEDULER.....	68
TABLE 6.3: FIXED CONTROLLERS' GAINS. ....	76
TABLE 7.1: TWO PASSES IN THE HYBRID LEARNING PROCEDURE FOR ANFIS. ....	87
TABLE 7.2: PARAMETERS OF THE LINEAR OUTPUT MEMBERSHIP FUNCTIONS OF THE SPEED CONTROLLER. ....	90
TABLE 7.3: PARAMETERS OF THE LINEAR OUTPUT MEMBERSHIP FUNCTIONS OF THE ACTIVE AND REACTIVE POWER CONTROLLERS.....	90
TABLE 8.1: OPTO-COUPLER ABSOLUTE MAXIMUM RATINGS. ....	121
TABLE 8.2: OPTO-COUPLER ELECTRICAL AND OPTICAL CHARACTERISTICS. ....	121
TABLE 8.3: MOSFET ELECTRICAL CHARACTERISTICS. ....	125
TABLE 8.4: MOSFET DRIVER ELECTRICAL CHARACTERISTICS. ....	128
TABLE 8.5: CURRENT FEEDBACK SCHEMES. ....	129
TABLE 8.6: QUADRATURE ENCODER TRUTH TABLE. ....	133
TABLE 8.7: CONTROLLERS' PERFORMANCE FOR SUB-SYNCHRONOUS OPERATION. ....	140
TABLE 8.8: CONTROLLERS' PERFORMANCE FOR SUPER-SYNCHRONOUS OPERATION. ....	144

## Nomenclature

Generally symbols are defined locally. The list of principal symbols is given below

$v_{ds}, v_{qs}$	d- and q- axis stator voltages respectively.
$v_{dr}, v_{qr}$	d- and q- axis rotor voltages respectively.
$i_{ds}, i_{qs}$	d- and q- axis stator currents respectively.
$i_{dr}, i_{qr}$	d- and q- axis rotor currents respectively.
$\lambda_{ds}, \lambda_{qs}$	d- and q- axis stator flux linkages respectively.
$\lambda_{dr}, \lambda_{qr}$	d- and q- axis rotor flux linkages respectively.
$R_s, R_r$	Stator and rotor resistances respectively.
$L_s, L_r$	Stator and rotor inductances respectively.
$L_{sl}, L_{rl}$	Stator and rotor leakage inductances respectively.
$L_m, L_{ms}$	Unsaturated and saturated magnetizing inductances respectively.
$X_s, X_r$	Stator and rotor reactances respectively.
$X_{sl}, X_{rl}$	Stator and rotor leakage reactances respectively.
$X_m, X_{ms}$	Unsaturated and saturated magnetizing reactances respectively.
$\omega_o, \omega_m$	Synchronous and rotor speeds respectively.
$i_m$	Magnetizing current.
$i_{md}, i_{mq}$	d- and q-axis magnetizing currents respectively.
$T_e, T_m$	Air-gap torque and mechanical torque respectively.
$H$	Combined inertia of rotor and mechanical load.
$B$	Friction coefficient in pu.



# **1 Introduction**

## **1.1 Background**

Wind power is the fastest growing source of electrical energy in the world today due to the increasing awareness of the environmental problems together with the rapid increase in the fuel cost and the power demand. Increasing by approximately 32% a year globally over the last five years, wind energy has proven to be a clean, abundant and completely renewable source of energy. With a total installed capacity of wind generation worldwide now is almost 95 GW; this figure is expected to reach 160 GW by 2012 [1]. The use of wind turbines to generate electricity can be traced back to the late nineteenth century with the 12 kW DC windmill generator constructed by Brush in the USA and the research undertaken by LaCour in Denmark. However, for much of the twentieth century there was little interest in using wind energy other than for battery charging for remote dwellings and these low-power systems were quickly replaced once access to the electricity grid became available. One notable exception was the 1250 kW Smith-Putnam wind turbine constructed in the USA in 1941. This remarkable machine had a steel rotor 53 m in diameter, full-span pitch control and flapping blades to reduce loads. Although a blade spar failed catastrophically in 1945, it remained the largest wind turbine constructed for some 40 years.

The sudden increase in the price of oil stimulated a number of substantial government-funded programs of research, development and demonstration. In the USA this led to the construction of a series of prototype turbines starting with the 38 m diameter 100 kW Mod-0 in 1975 and culminating in the 97.5 m diameter 2.5 MW Mod-5B in 1987. Similar programs were pursued in the UK, Germany and Sweden. There was considerable uncertainty as to which architecture might prove most cost-effective and several innovative concepts were investigated at full scale. In Canada, a 4 MW vertical-axis Darrieus wind turbine was constructed and this concept was also investigated in the 34 m diameter Sandia Vertical Axis Test Facility in the USA. In the UK, an alternative vertical-axis design using straight blades to give an 'H' type rotor was proposed by Dr

Peter Musgrove and a 500 kW prototype was constructed. In 1981 an innovative horizontal-axis 3 MW wind turbine was built and tested in the USA. This used hydraulic transmission and, as an alternative to a yaw drive, the entire structure was orientated into the wind. The best choice for the number of blades remained unclear for some time and large turbines were constructed with one, two or three blades.

The so-called 'Danish' wind turbine concept emerged from a three-bladed, stall-regulated rotor and a fixed-speed, induction machine drive train. This deceptively simple architecture has proved to be remarkably successful and has now been implemented on turbines as large as 60 m in diameter and at ratings of 1.5 MW. However, as the sizes of commercially available turbines now approach that of the large prototypes of the 1980s it is interesting to see that the concepts investigated then of variable-speed operation, full-span control of the blades, and advanced materials are being used increasingly by designers.

## ***1.2 Generators used in wind energy***

### **1.2.1 DC Generators**

The classical DC generator consists of a spinning armature and a surrounding stationary and constant field winding, which induces an output or load current in the armature winding. (This is the reverse of AC generators used today and described above, in which the load current is induced in the stator. However, the same physics applies.) Depending on the number of poles, one or more cycles of alternating voltage are induced per armature revolution. The output of this turning armature must be continuously mechanically switched so that the output current will always be flowing in the same direction. The switch used is of course the well-known commutator with its copper segments insulated from each other and carbon brushes pressing against them. When these rotating machines are used as generators, they may provide their own field current.

These types of generators were used in factories, machine shops and vehicles from the early part of the 20<sup>th</sup> century on. The addition of commutators and brushes makes DC designs more expensive and less reliable than comparable AC generators. A classical example of an early variable-speed DC turbine is the machine mentioned above [2].

### **1.2.2 Synchronous Generators**

Essentially, all primary generators employed by electric utilities belong to the synchronous class. They are sometimes called alternators. The fundamental characteristic of synchronous motors and generators is that their rotor speed is always locked in with and is exactly proportional to the frequency of the interconnected power grid. If a synchronous machine is the only generator on the grid, the grid frequency is determined by its speed. If the grid includes other generators, that grid will probably be much more powerful (stiff) and will therefore force any added synchronous generator to turn at exactly the grid synchronous speed. If the torques or currents necessary to accomplish this exceed the added machine's rating, either circuit breakers will open or the generator and its prime mover will be damaged. Changes in load will cause the synchronous machine rotor to advance or drop back a few degrees from the spinning magnetic field of the stator supplied by the utility. Thus we see that, if a wind turbine using a synchronous generator is directly connected to a stiff grid, this turbine will necessarily become a constant-speed machine. On the other hand, if this turbine stands alone, its voltage and frequency will be determined by the wind, assuming that there is no control system. However, if a wind turbine is connected to a power grid through appropriate electronic power-processing modules, not only will the grid be supplied with power at constant voltage and frequency, but also the power (and therefore speed) demanded of the turbine can be determined from an algorithm programmed into the turbine control system.

The source of the magnetic field in such a generator determines to which of several subclasses a synchronous machine belongs. Nearly all the largest machines belong to the conventional class in which slip rings or other means on the rotor feed direct current (DC) into wire-wound magnetic pole pieces. Not only do these magnets provide the essential magnetic field for generator action, but the amount of reactive power (kilovars or kVAs) supplied by the machine to a stiff grid is controlled by the magnitude of this field current. As this field current is increased, the generator passes from consuming to producing volt-amperes reactive (VARs).

In a similar but rapidly developing subclass the electromagnets of the conventional synchronous machine are replaced by permanent magnets (PMs). Advantages of the PM subclass of machines are simplicity and no need to waste DC power to create the

magnetic field. The disadvantages are expense of permanent magnets, and no means to control the strength of the magnetic field and therefore reactive power. With the introduction of power electronics between a synchronous machine stator and the electrical grid, a synchronous machine can run at variable speed [2].

### **1.2.3 Induction Generators**

The simplest form of AC generator (after the PM type) and the type that has most often been used in wind turbines is the induction generator. It depends on an external voltage source (e.g. the electric utility) to produce a magnetic field in the stator, which is to say that this device consumes VARs in order that it may produce watts. In this case the current in the rotor is induced by the differential speed of the spinning rotor coils with respect to the spinning stator magnetic field. The simplest form of induction generator is the squirrel cage, in which the rotor is formed from welded copper bars, rods or copper castings embedded in a soft iron cylindrical rotor. Induction generators are also constructed using wound rotors, in which rotor currents are induced in windings of copper or aluminum wire. When wound rotors are externally accessible through slip rings, a variable resistance can be inserted. This can control the electrical torque and will control the percentage of slip. Recall that slip measures the difference in speed between the spinning magnetic field of the stator and the mechanical speed of the rotor. Its numerical value is the ratio of this speed difference to the synchronous speed and is thus dimensionless.

Alternatively, a power electronics module can be substituted for the external resistance, thus allowing the injection of currents of appropriate frequency into the rotor windings. For example, this allows an induction machine to act as a generator at sub-synchronous speeds [2].

## **1.3 Doubly-Fed Machines and Applications**

Developments in solid-state power converter controlled AC variable speed drives have been very intensive in recent years. Squirrel cage induction motor drives have been the major focus of development, achieving high performance through vector control methods. Variable speed drives using synchronous motors, brushless DC motors,

synchronous reluctance motors and switched reluctance motors are also under enthusiastic development.

Doubly-fed machines are another alternative for variable speed drives. They include wound rotor induction machines, self-cascaded induction machines and doubly excited brushless reluctance machines. Doubly-fed machines generally refer to a class of electric machines that have two separately controlled AC circuits on different sides or the same side of the air-gap. Therefore, synchronous machines and DC machines are not categorized as doubly-fed machines, even though they do have two different circuits, one of them being the DC excitation circuit. A common feature for doubly-fed machines is that one of the circuits is usually fed from the 60Hz power line, while the other controlled circuit has slip frequency voltage and current.

The original doubly-fed machine is the wound rotor induction machine, having been in use for a long time as a means of speed control through the rotor side circuit. Slip power recovery systems employing wound rotor induction machines have been used in high horse-power applications requiring a narrow speed range.

Another doubly-fed machine, the self-cascaded induction machine, features dual sets of three phase windings of different pole numbers wound in a common stator core with a cage rotor. Due to the simple cage rotor structure without brushes or slip rings, reliability and costs are improved while speed can be controlled through one of the stator windings. However, its applications are rare and progress has been slow, only in recent years it received interest under the name of brushless doubly-fed machine.

The doubly excited brushless reluctance machine was developed from the self-cascaded induction machine, with a reluctance rotor to replace the short-circuit cage rotor. Efficiency was improved by eliminating the rotor copper losses. Still, applications are rare, due to the lack of understanding of its principles and dynamics with an unusual structure.

Compared to the more conventional electrical machines, these doubly-fed machines have many attractive advantages for variable speed drive applications, the most important one being the significant cost reduction with a reduced power converter rating. Furthermore, these doubly-fed machines have greater potential for applications in

variable speed power generation, as has already been widely recognized in the case of the slip power recovery wind power generators with the wound rotor induction machine.

Benefiting from the rapid developments in power switching devices, microelectronics, computer aided design, control technologies and microcomputers, the many potential advantages of the doubly-fed machines can now be realized. With a better understanding, improved machine design, flexible power converters and innovated controllers, the doubly-fed machines could favorably compete for many applications.

#### **1.4 Research Objectives**

Most induction machines in the world are cage-type machines. However, a special class of induction machines with a three-phase wound rotor, called doubly-fed induction generators (DFIG), has become very popular for use as wind generators.

The theory, analysis, characteristics, and control of a DFIG are covered in depth in the next two chapters. However, briefly stated, the main advantages of a DFIG are variable speed operation and reactive power control. These advantages are made possible by explicit control of the rotor currents via a converter connection to the three-phase rotor windings. The present research aims to find a way to exploit the rotor control capabilities of the DFIG to compensate for the problems caused by wind speed changes, while providing the standard variable speed (active power control) and reactive power control.

The main objective of this research or is to design an intelligent, effective and stable control topology for a DFIG that can achieve:

- Variable speed control: that can control the generator speed above and below synchronous speed according to the random change in wind speed.
- Active power control: by operating the generator at variable speed, the system can track the maximum power point curve of the wind turbine and extract more power.
- Reactive power control: decoupled control of active and reactive power allows the operation at unity power factor or even at a leading power factor.

To achieve those targets, field orientation technique is employed together with three intelligent control methods which are adaptive, fuzzy and neuro-fuzzy control.

## **1.5 Dissertation outline**

This dissertation is organized as follows:

- Chapter 2:** This chapter demonstrates the history and the state of the art usage of induction generators in wind power generation.
- Chapter 3:** This chapter discusses in detail the induction machine modeling. First, the steady-state model is presented, then the dynamic model. Next, a new induction machine dynamic model that incorporates both main and leakage flux saturation is developed. Finally, a novel experimental procedure to determine the induction machines' saturation characteristics is illustrated.
- Chapter 4:** In this chapter, the vector control technique is investigated, then it is implemented to control the DFIG.
- Chapter 5:** This chapter explains the adaptive control theory then demonstrates the implementation of an adaptive PI gain scheduler to control the DFIG. Finally, it shows the numerical investigation of a DFIG model that incorporates the proposed adaptive PI gain scheduler and compares its performance to the conventional PI controller with fixed gains.
- Chapter 6:** This chapter starts by introducing the concepts of the fuzzy logic and fuzzy inference system building blocks. Then, a new fuzzy gain scheduler is developed. Finally, the developed fuzzy gain scheduler is used to control the DFIG wind power generator. A system using the developed fuzzy gain scheduler is simulated and its performance is evaluated.
- Chapter 7:** This chapter introduces the neuro-fuzzy theory which is a relatively new concept based on the fuzzy logic reasoning and benefitted of the powerful learning capabilities of the neural networks. Then, a neuro-fuzzy gain scheduler is developed and employed in a wind driven DFIG. Next, the performance of the system utilizing the developed neuro-fuzzy gain scheduler is simulated and analyzed.
- Chapter 8:** In this chapter, a practical experimental system is built using a DFIG and a DC motor as a prime mover. A power electronic back-to-back converter system is developed and microcontroller is programmed to control the power flow through the rotor circuit. The previously developed vector

control technique is utilized and the various controllers, formerly developed, are programmed into the microcontroller. Finally, the performance of the system using different controllers is evaluated and compared.

## **1.6 References**

- [1] World Wind Energy Association website ([http:// www.wwindea.org/](http://www.wwindea.org/)).
- [2] P. W. Carlin, A. S. Laxson and E. B. Muljadi, "The History and State of the Art of Variable-Speed wind Turbine Technology," *Journal of Wind Energy*, vol. 6, pp. 129-159, 2003.



## **2 Induction Generators used in Wind Power**

The simplest form of AC generator and the type that has most often been used in wind turbines is the induction generator. The induction generators (particularly squirrel-cage induction generators) have robust construction, lower initial and run-time cost (due to brushless construction), and lower maintenance cost. The induction generators are suitable for grid-connected as well as standalone applications. Most of the wind power plants are using a fairly straightforward power conversion technique with induction generator directly connected to the grid. However, this system is capable of converting power efficiently, in a limited range of wind speed only, and draws large amount of reactive power from the grid [1].

In the fixed-speed system, turbine is coupled to a squirrel-cage induction generator through a gearbox and the stator of the generator is connected to the grid through a step-up transformer. Therefore, the grid frequency determines the speed of the generator and the turbine shaft, as the slip being nominally of the order of 5%. This scheme is simple and reliable. However, it severely limits the turbine utilization and feeds power with poor power factor to the grid [2]. In grid-connected mode, the excitation current to the induction generator is supplied from the grid. Also, a mechanical arrangement is used to maintain the rotor speed above the synchronous speed. In self-excitation mode, when the generator operates as stand-alone, the excitation current is supplied by a local source. The simplest way of self-excitation is the use of fixed capacitors connected across the induction generator terminals. The excitation capacitor value is chosen so as to regulate the generated voltage with changing speed and load. The excitation capacitance value can be changed by switching capacitor banks or using a thyristor-controlled reactor for smooth variation [3].

The fact that the induction generators did not, for a long time, find many practical applications has mostly been due to the inability of controlling its terminal voltage and frequency under varying operating conditions. The ability to control the generator terminal voltage and frequency is extremely important in stand-alone operation, but when connected to the grid, terminal voltage and frequency controls are not required since they

are determined by the grid itself and the reactive power demand can be also met by the grid.

## **2.1 Fixed speed and variable speed wind turbines**

Wind turbine rotors develop their peak efficiency at one particular tip speed ratio (see Figure 2.1), so fixed speed machines operate sub-optimally, except at the wind speed corresponding to this tip speed ratio. Energy capture can clearly be increased by varying the rotational speed in proportion to the wind speed so that the turbine is always running at optimum tip speed ratio, or alternatively a slightly reduced improvement can be obtained by running the turbine at one of two fixed speeds so that the tip speed ratio is closer to the optimum than with a single fixed speed.

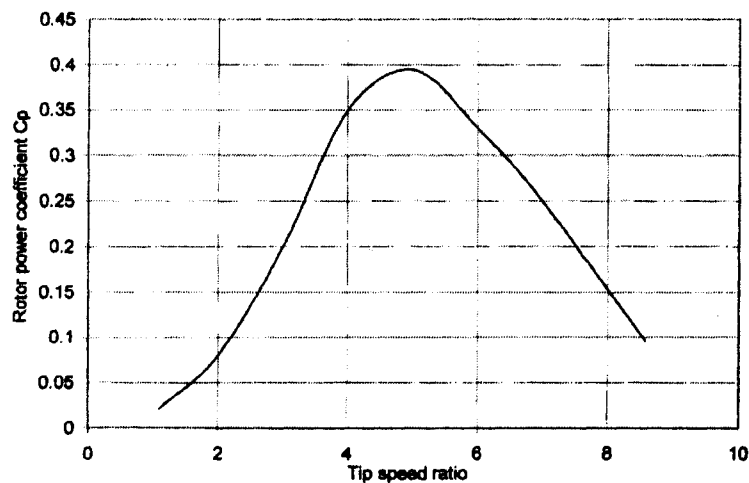


**Fig. 2.1: Rotor power coefficient versus tip-speed ratio has a single maximum [4].**

Because wind turbine mechanical power at the rotor hub depends on both rotor speed and wind speed, harvested power can be represented on a three-dimensional surface. Figure 2.2 is an example of the characteristic power surface of a small turbine. Blade pitch is assumed constant. As expected, output power rises with increasing wind and increasing rotor speed for low and moderate values.

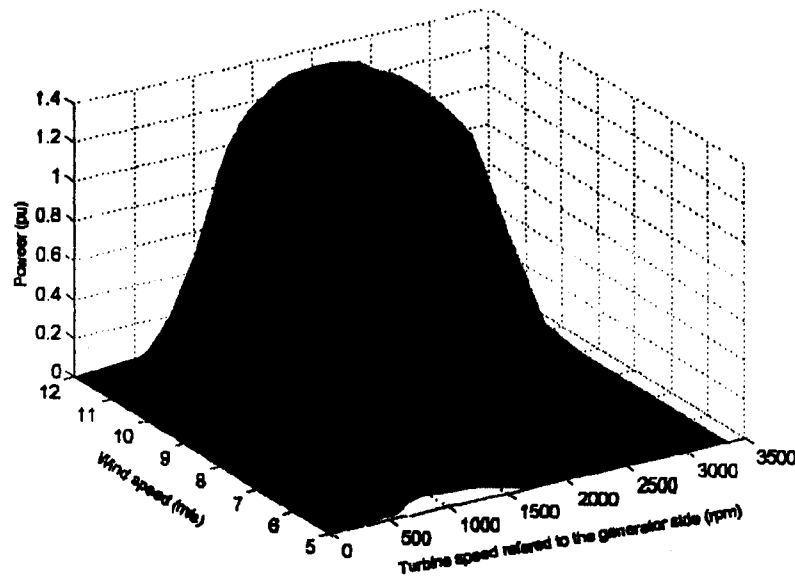


Fig. 2.2: Wind turbine power for different wind speeds showing maximum power point curve [4].

In general, there are two types of wind turbines (WTs): fixed-speed and variable-speed. With relatively simple design, the fixed-speed WT provided a cost efficient opportunity for entrepreneurs to explore the viability of pollution-free generation in the early days. However, the poor mechanical isolation and narrow operating speed range inherited from the direct connection of a turbine driven squirrel-cage induction machine has limited the generation yield. Another problem impairing the fixed-speed WT was the frequent shut-off caused by high wind speed, disturbance in the grid, or excess reactive power consumption. Although many remedies, such as stall/pitch control and supporting capacitor bank, were proposed, the fixed-speed design is being phased out of the market particularly in the area requiring high capacity WTs. The introduction of the variable-speed WTs has bred new life into the wind generation sector. The addition of the power electronic driven variable-speed drive has drastically improved the performance of WTs in virtually every aspect [5-9]. Among the major variants, Fig. 2.3, the doubly-fed configuration has gained the most popularity owing mainly to its economical design. Instead of having high-cost full scale converter at the mains, the power electronic drive connected between the stator and rotor of the wound rotor induction machine (WRIM) is required to handle only fraction of the total generation capacity, In spite of the more expensive WRIM, savings from the lower rating power electronics has placed the doubly-

fed induction generator (DFIG) based WT in a very competitive position [9]. In the current market, generation capacity of the DFIG-based WTGs has already reached MW range. When the capacity and number of the DFIG-based WTGS continuously increase in the network, it is no longer appropriate to model them as simple negative loads [11]. To help reflect their actual impact on the existing system under various operating conditions, the WTGs need to be modeled with sufficient details.

Variable speed generators have numerous advantages over the fixed speed generators such as [12]-[14]:

- Maintain maximum power transfer conditions for shaft speed variations over a wide range of wind speed and, hence, to maximize the annual energy production.
- Reduce the mechanical stresses and acoustic noise.
- Dynamically compensate for torque and power pulsations.
- Improving power quality.
- Improve system efficiency as the turbine speed can be adjusted as a function of wind speed to maximize output power.

A variable-speed system can extract more power by operating with a controlled tip-speed ratio, which will enable maximum power tracking. Moreover, such system keeps the system power factor almost unity at all wind speed condition through the ability of controlling the active and reactive power generated. Various systems with varied control strategies are used in variable speed wind generation system as shown in Fig.2.3.

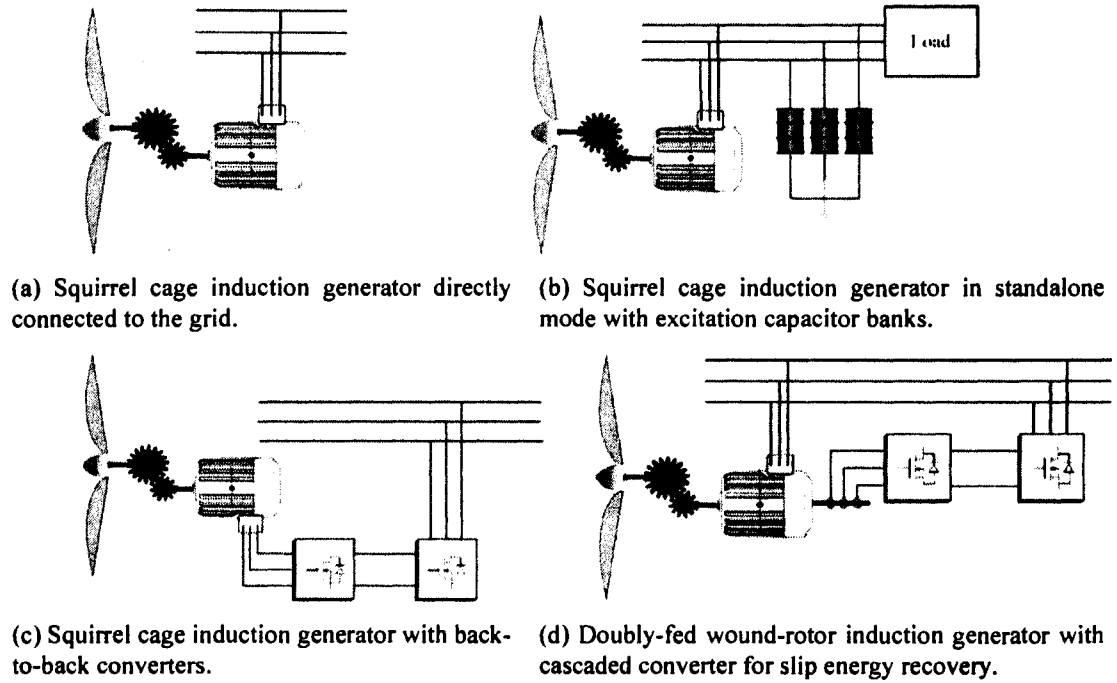


Fig. 2.3: Different configurations for wind-driven Induction generators.

## 2.2 Doubly-fed induction generator in wind power

Both squirrel-cage and wound-rotor induction machines could be used as variable speed generator. Wound rotor induction machine has many advantages in wind energy conversion application compared to squirrel-cage machine. One scheme for wound rotor induction machine is shown in Fig. 2.3(d). In this scheme, a converter cascade is used between the slip-ring terminals and the utility grid to control the rotor power. This scheme is called the doubly-fed induction generator (DFIG) scheme, because the power output is tapped from both the stator and the rotor circuits. This allows fixed-frequency electric power to be extracted from the generator stator. Consequently, the use of doubly-fed induction machines is receiving increasing attention for wind generation purposes [15]-[21]. The DFIG has the ability to operate at sub-synchronous as well as super-synchronous speed. The power flow in the rotor circuit depends on the operating speed. If the DFIG operates at a sub-synchronous speed, the rotor will draw power from the grid while if the DFIG operates at a super-synchronous speed, the rotor will supply power to the grid. Therefore, the DFIG is the only known scheme in which the generator gives more than its rated power without being overheated and the power generation can be

realized in a wide range of wind. Thus, the use of DFIG as wind electric generator has numerous advantages such as [12]-[14]:

- Reduced inverter cost: Inverter rating is typically 25%-30% of the total system power in the case of wound-rotor while in the case of squirrel-cage the rating of inverter should be equal to the whole system power rating.
- Reduced cost of the inverter filters and EMI filters: Filters are rated for 25%-30% of total system power, and inverter harmonics represent a smaller fraction of total system harmonics.
- Improved system efficiency: Less inverter loss and, also, power production is maximized by tracking the maximum power point of the wind turbine speed characteristics.
- Improved power factor: Independent control of the active and reactive power is achievable which facilitate the operation at or near unity power factor.

The control of the generator speed to track the wind's maximum power is desired in order to maximize the annual power generation and also since any mismatch will give rise to mechanical stress, on the turbine parts, which reduces its lifetime as well as increasing the acoustic noise. Using an efficient and fast way to control the turbine speed will reduce the need for other mechanical control systems such as blade angle control and will reduce the mechanical stress on the gear box and other mechanical parts.

### **2.3 References**

- [1] R. Zavadil, N. Miller, A. Ellis, and E. Muljadi, "Making connections," *IEEE Power and Energy Magazine*, vol. 3, no. 6, pp. 26 – 37, Nov.-Dec. 2005.
- [2] G. Poddar, A. Joseph, and A.K. Unnikrishnan, "Sensorless variable-speed controller for existing fixed-speed wind power generator with unity-power-factor operation," *IEEE Trans. on Industrial Electronics*, vol. 50, pp. 1007-1015, 2003.
- [3] S. Wekhande and V. Agarwal, "Simple control for a wind-driven induction generator," *IEEE Industry Applications Magazine*, vol. 7, pp. 44-53, March-April 2001.
- [4] T. Ackermann, *Wind Power in Power Systems*, John Willy & Sons, Chichester, England, 2005.

- [5] P.B. Eriksen, T. Ackermann, H. Abilgaard, P. Smith, W. Winter, and J. R. García, "System operation with high wind penetration," *IEEE Power and Energy Magazine*, vol. 3, no. 6, pp. 65-75, 2005.
- [6] D. S. Zinger, E. Muljadi, "Annualized wind energy improvement using variable speeds", *IEEE Transactions on Industry Applications*, vol. 33, no. 6, pp. 1444-1447, Nov.-Dec. 1997.
- [7] R. Datta, and V. T. Ranganathan, "Variable-speed wind power generation using doubly fed wound rotor induction machine - A comparison with alternative schemes," *IEEE Transactions on Energy Conversion*, vol. 17, no. 3, pp. 414-420, Sept. 2002.
- [8] S. Heier, *Grid Integration of Wind Energy Conversion Systems*, Chincester, UK, John Wiley & Sons Ltd., 1998
- [9] I. M. Rodriguez, L. Fernandez, D. Beato, R. Iturbe, I. Usaola, P. Ledesma, and J. R. Wilhelmi, "Incidence on power system dynamics of high penetration of fixed speed and doubly fed wind energy systems: study of the spanish case," *IEEE Transactions on Power Systems*, vol. 17, no. 4, pp. 1089-1095, Nov. 2002.
- [10] P. Pourbeik, *Integration of Wind Energy into the Alberta Electric System Stages 2 Er 3: Planning ana Interconnection Criteria Electric Systems Consulting ABB Inc.*, Report Number: 2004-10803-2.R01.4, Dec. 2003.
- [11] J. Ekanauake, L. Holdsworth, and N. Jenkins, "Control of DFIG wind turbines," *IEEE Power Engineering Magazine*, vol. 17, pp. 28-32, Feb. 2003.
- [12] S. Muller, M. Deicke and R.W. De Doncker, "Doubly fed induction generator systems for wind turbines," *IEEE Industry Applications Magazine*, vol. 8, pp. 26-33, 2002.
- [13] V. Akhmatov, "Variable-speed wind turbines with doubly-fed induction generatrors Part I: Modelling in dynamic simulation tools," *Wind Engineering*, vol. 26, pp. 85-108, 2002.
- [14] A. D. Hasen, P. Sørensen, F. Iov, and F. Blaabjerg, "Control of variable speed wind turbines with doubly-fed induction generators," *Wind Engineering*, vol. 28, pp. 411-434, 2004.

- [15] R. Spee, S. Bhowmik, and J. H. R. Enslin, "Novel control strategies for variable-speed doubly fed wind power generation systems," *Renewable Energy*, vol. 6, pp. 907-915, 1995.
- [16] D. J. Atkinson, R. A. Lakin, and R. Jones, "A vector-controlled doubly-fed induction generator for a variable-speed wind turbine application," *Trans. Inst. Meas. Contr.*, vol. 19, pp. 2-12, 1997.
- [17] R. S. Peña, J. C. Clare, and G. M. Asher, "Doubly fed induction generator using back-to-back PWM converters and its application to variable-speed wind-energy generation," *IEE Proc. Electric Power Applications*, vol. 143, no. 3, pp. 231-341, 1996.
- [18] A. Tapia, G. Tapia, J. X. Ostolaza and J.R. Sáenz, "Modeling and control of a wind turbine driven doubly fed induction generator," *IEEE Trans. on Energy Conversion*, vol. 18, pp.194-204, 2003.
- [19] M. Y. Uctug, I. Eskandarzadeh, and H. Ince, "Modelling and output power optimization of a wind turbine driven double output induction generator," *IEE Proc. on Electric Power Applications*, vol. 141, pp. 33-38, 1994.
- [20] T. Brekken and N. Mohan, "A novel doubly-fed induction wind generator control scheme for reactive power control and torque pulsation compensation under unbalanced grid voltage conditions," *IEEE 34th Annual Power Electronics Specialist Conf.*, vol. 2, pp.760-764, 2003.
- [21] Y. Tang and L. Xu, "A flexible active and reactive power control strategy for a variable speed constant frequency generating system," *IEEE Trans. on Power Electronics*, vol. 10, pp. 472-478, 1995.



### 3 Induction Machine Modeling

#### 3.1 Introduction

The main aspect which distinguishes the induction machine from other types of electric machines is that the secondary currents are created solely by induction, as in a transformer, instead of being supplied by a DC exciter or other external power source, through slip rings or a commutator, as in synchronous and DC machines. Depending on the condition of operation, the induction machine can be used as a motor or generator.

When the stator is excited from a balanced three-phase supply, the three phases together create a constant magnitude, synchronously revolving mmf or field in the air gap with a crest value  $3/2$  times the peak value of the alternating field due to one phase alone [1].

This field rotates around the air-gap at synchronous speed  $N_e$ , which can be calculated as

$$N_e = \frac{120f_e}{P} \quad (3.1)$$

Where

$f_e$  excitation frequency in cycles per second (Hz).

$P$  number of pole pairs.

$N_e$  synchronous speed in revolutions per minute (rpm).

$N_e$  is also expressed as the rotational speed of the stator magnetic field, or mmf.

The slip of a motor,  $s$ , which is defined as the slip of the rotor with respect to the stator magnetic field, can be given as

$$s = \frac{N_e - N_r}{N_e} \quad (3.2a)$$

where

$N_r$  the rotational speed of the rotor in rpm.

If the speeds are expressed in radians per second the slip is given by

$$s = \frac{\omega_e - \omega_r}{\omega_e} \quad (3.2b)$$

where

$\omega_e$  synchronous speed in radians per second (rad/sec).

$\omega_r$  rotor speed in rad/sec.

### 3.2 Steady-state induction machine model

The relative speed between the synchronous speed and the rotor speed is expressed in its equivalent electrical speed as  $\omega_e - \omega_r$  or  $s\omega_e$ , where the electrical rotor speed is the product of the mechanical speed and the number of pole pairs.

Rotation of the rotor changes the relationships between stator and rotor emfs. However, it does not directly change the inductance and resistance parameters. The angular frequency of the induced current in the rotor is  $s\omega_e$  and the induced voltage in the rotor will be  $sE_r$ , where  $E_r$  is the induced voltage in the rotor when the rotor is stationary.

This is based on the assumption that the induction machine is only supplied from the stator terminals. Assuming that the winding is distributed sinusoidally in angular space around the stator to produce a sinusoidally distributed magnetic field [2] and the rotor winding is similar in form to the stator winding, then the per-phase equivalent circuit of the stator side of the three-phase induction machine can be represented as follows

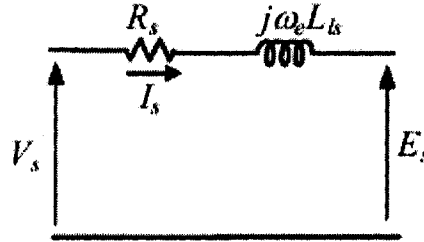


Fig. 3.1: Stator side of the per-phase equivalent circuit of a three-phase induction machine.

where

$V_s$  stator voltage, V.

$I_s$  stator current, A.

$R_s$  stator winding resistance,  $\Omega$ .

$L_{ls}$  stator leakage inductance, H.

$E_s$  induced emf in the stator winding due to the rotating magnetic field that links the stator and rotor windings, V.

$\omega_e$  stator current angular frequency, rad/sec.

For constant stator flux the voltage induced in the rotor depends solely on the slip, which is the relative speed between the stator flux rotating at synchronous speed and rotor speed. Maximum induced voltage occurs in the rotor when the rotor is stationary.

Without any external input on the rotor side, the rotor circuit is given by

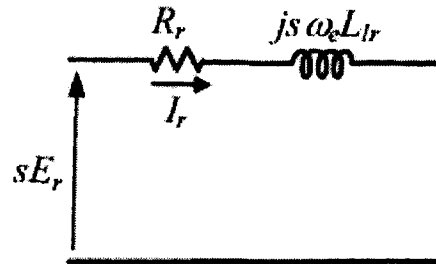


**Fig. 3.2: Rotor side of the per-phase equivalent circuit of a three-phase induction machine.**

where

$sE_r$  induced voltage in the rotor, V.

$I_r$  rotor current, A.

$R_r$  rotor winding resistance,  $\Omega$ .

$L_{lr}$  rotor leakage inductance, H.

$s\omega_e$  rotor current angular frequency, rad/sec.

If all the terms in the rotor side are divided by the slip,  $s$ , a modified circuit is obtained as shown in Fig. 3.3.

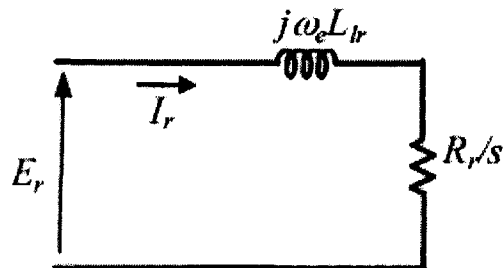


**Fig. 3.3: Rotor side of the induction machine with adjustment.**

Using the appropriate voltage transformation ratio between the stator and rotor, the rotor voltage,  $E_r$ , referred to the stator is then equal to  $E_s$ , in Fig. 3.1. The stator and rotor circuits are linked because of the mutual inductance  $L_m$ . When all circuit parameters are

referred to the stator, the stator and rotor circuits can be combined to give the circuit shown in Fig. 3.4.

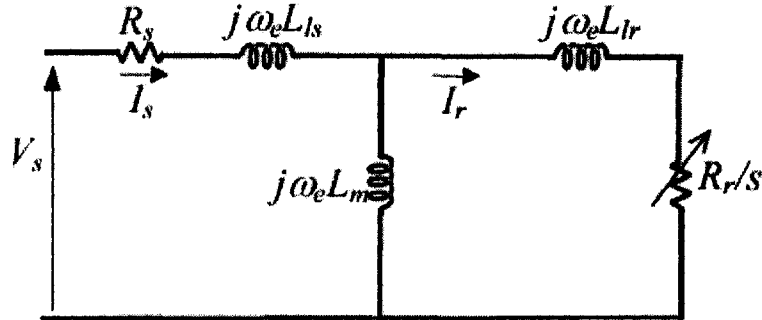


**Fig. 3.4: Per-phase equivalent circuit of three-phase induction machine neglecting core loss.**

In Fig. 3.4 the core loss, which is due to hysteresis and eddy current losses, is neglected. It can be compensated by deducting the core loss from the internal mechanical power at the same time as the friction and windage losses are subtracted [3]. The no load current in three-phase induction machines consists of the iron loss or core loss component and the magnetizing component. From the iron loss current component and from the applied voltage the equivalent resistance for the excitation loss can easily be calculated. There is also some core loss in the rotor. Under operating conditions, however, the rotor frequency is so low that it may reasonably be assumed that all core losses occur in the stator only [4].

The core loss can be accounted for by a resistance  $R_m$  in the equivalent circuit of the induction machine [5].  $R_m$  is dependent on the flux in the core and frequency of excitation. For constant flux and frequency  $R_m$  remains unchanged. As  $R_m$  is independent of load current it is connected in parallel with the magnetizing inductance  $L_m$ . The equivalent circuit including  $R_m$  is shown in Fig. 3.5.

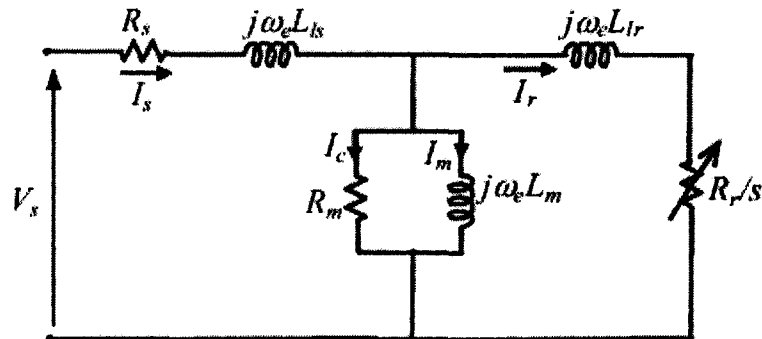


**Fig. 3.5: Per-phase equivalent circuit of three-phase induction machine including core loss.**

### 3.3 Induction machine dynamic model

Using the D-Q representation, the induction machine can be modeled as shown in Fig. 3.6. This representation is a general model based on the assumption that the supply voltage can be applied to both the stator and/or rotor terminals. In squirrel cage induction machines voltage is supplied only to the stator terminals. In general power can be supplied to the induction machine (induction motor) or power can be extracted from the induction machine (induction generator). It all depends on the precise operation of the induction machine. If electrical power is applied to the stator of the induction machine then the machine will convert electrical power to mechanical power.

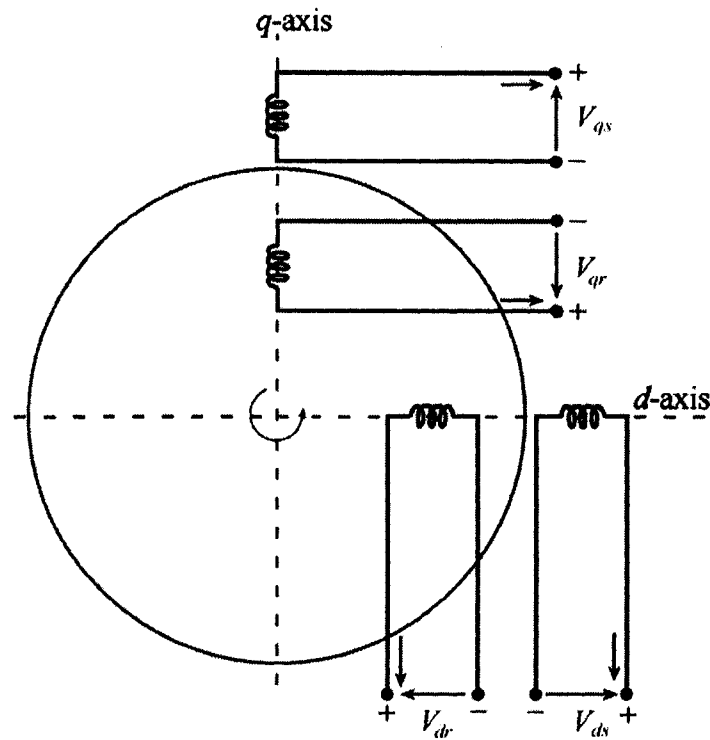


Fig. 3.6: D-Q axis representation of induction machine.

As a result the rotor will start to rotate and the machine is operating as a motor. On the other hand, if mechanical power is applied to the rotor of the induction machine then the machine will convert mechanical power to electrical power. In this case the machine is operating as an induction generator. When the induction machine operating as a generator is connected to the grid or supplying an isolated load, driven by an external prime mover, then the rotor should be driven above synchronous speed. When the machine is operated as a motor, power flows from the stator to the rotor, crossing the air

gap. However, in the generating mode of operation, power flows from the rotor to the stator. Only these two modes of operation are dealt with in this investigation. The braking region, where the rotor rotates opposite to the direction of the rotating magnetic field, is not dealt with here.

The conventional model and the d-q (or D-Q) axes model are the same for steady state analysis. The advantage of the d-q axes model is that it is powerful for analyzing the transient and steady state conditions, giving the complete solution of any dynamics.

The general equations for the d-q representation of an induction machine, in the stationary stator reference frame, are given as [6]:

$$\begin{bmatrix} V_{ds} \\ V_{qs} \\ V_{dr} \\ V_{qr} \end{bmatrix} = \begin{bmatrix} R_s + pL_s & 0 & pL_m & 0 \\ 0 & R_s + pL_s & 0 & pL_m \\ pL_m & \omega_r L_m & R_r + pL_r & \omega_r L_r \\ -\omega_r L_m & pL_m & -\omega_r L_r & R_r + pL_r \end{bmatrix} \begin{bmatrix} I_{ds} \\ I_{qs} \\ I_{dr} \\ I_{qr} \end{bmatrix} \quad (3.3a)$$

where

$R_s$  stator winding resistance,  $\Omega$ .

$R_r$  rotor winding resistance,  $\Omega$ .

$L_m$  magnetizing inductance, H.

$L_s$  stator leakage inductance, H.

$L_r$  rotor leakage inductance, H.

$\omega_r$  electrical rotor angular speed in rad/sec.

$p$   $d/dt$ , the differential operator.

Equation (3.3a) can be written in a first order differential equation form in an arbitrary rotating reference frame as given in the following matrix equation

$$\begin{bmatrix} V_{ds} \\ V_{qs} \\ V_{dr} \\ V_{qr} \end{bmatrix} = \begin{bmatrix} R_s & 0 & 0 & 0 \\ 0 & R_s & 0 & 0 \\ 0 & 0 & R_r & 0 \\ 0 & 0 & 0 & R_r \end{bmatrix} \begin{bmatrix} I_{ds} \\ I_{qs} \\ I_{dr} \\ I_{qr} \end{bmatrix} + \begin{bmatrix} p & -\omega_c & 0 & 0 \\ \omega_c & p & 0 & 0 \\ 0 & 0 & p & -(\omega_c - \omega_m) \\ 0 & 0 & (\omega_c - \omega_m) & p \end{bmatrix} \begin{bmatrix} \lambda_{ds} \\ \lambda_{qs} \\ \lambda_{dr} \\ \lambda_{qr} \end{bmatrix} \quad (3.3b)$$

and the equivalent circuit is shown in Fig. 3.7.

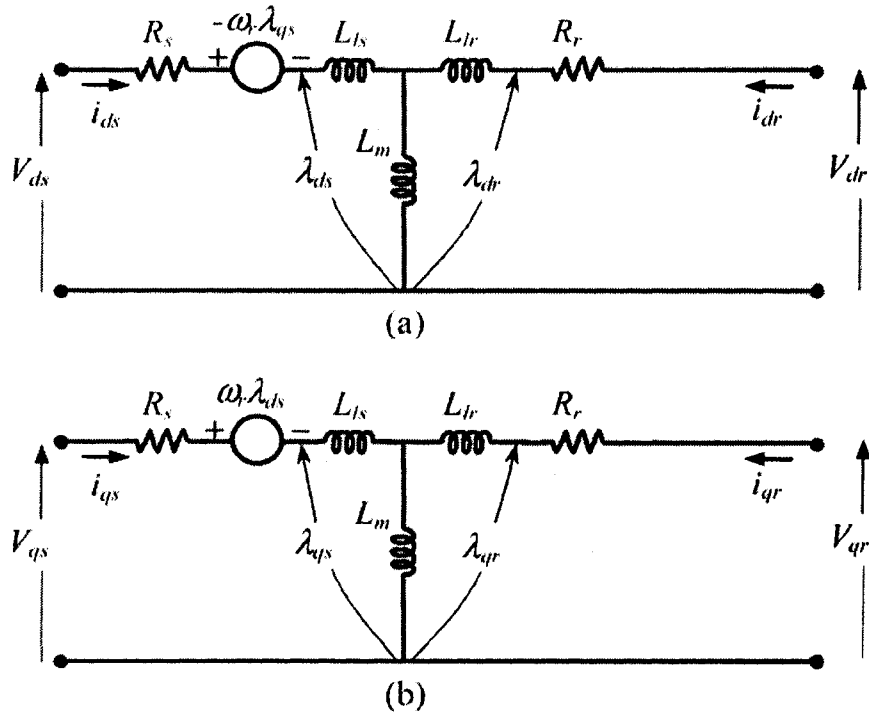


**Fig. 3.7: Equivalent circuits of the induction machine in an arbitrary rotating reference frame.**  
**(a) d-axis equivalent circuit. (b) q-axis equivalent circuit**

These four first order differential equations are solved with the well known fourth-order Runge-Kutta method to obtain the d- and q- axis leakage fluxes. These fluxes are related to the machine currents by the following equations

$$\begin{aligned}
 \lambda_{ds} &= L_s I_{ds} + L_m I_{dr} \\
 \lambda_{qs} &= L_s I_{qs} + L_m I_{qr} \\
 \lambda_{dr} &= L_m I_{ds} + L_r I_{dr} \\
 \lambda_{qr} &= L_m I_{qs} + L_r I_{qr}
 \end{aligned} \tag{3.4}$$

From which the machine currents are obtained as follows

$$\begin{aligned}
 I_{ds} &= \frac{1}{\Delta} (L_r \lambda_{ds} - L_m \lambda_{dr}) \\
 I_{qs} &= \frac{1}{\Delta} (L_r \lambda_{qs} - L_m \lambda_{qr}) \\
 I_{dr} &= \frac{1}{\Delta} (-L_m \lambda_{ds} + L_s \lambda_{dr}) \\
 I_{qr} &= \frac{1}{\Delta} (-L_m \lambda_{qs} + L_s \lambda_{qr})
 \end{aligned} \tag{3.5}$$

where,

$$\begin{aligned}
\Delta &= (L_s L_r - L_m^2) \\
L_s &= L_{ls} + L_m \\
L_r &= L_{lr} + L_m
\end{aligned} \tag{3.6}$$

In the previous discussion, the motoring convention was assumed, i.e. current direction is flowing toward the machine. If the generator convention was assumed, the dynamic equations as well as the equivalent circuit of the induction machine in the synchronous reference frame will be as in (3.7) and Fig. 3.8.

$$\begin{aligned}
V_{ds} &= -R_s I_{ds} + \lambda_{qs} - p\lambda_{ds} \\
V_{qs} &= -R_s I_{qs} - \lambda_{ds} - p\lambda_{qs} \\
V_{dr} &= -R_r I_{dr} + (1 - \omega_m)\lambda_{qr} - p\lambda_{dr} \\
V_{qr} &= -R_r I_{qr} - (1 - \omega_m)\lambda_{dr} - p\lambda_{qr}
\end{aligned} \tag{3.7}$$

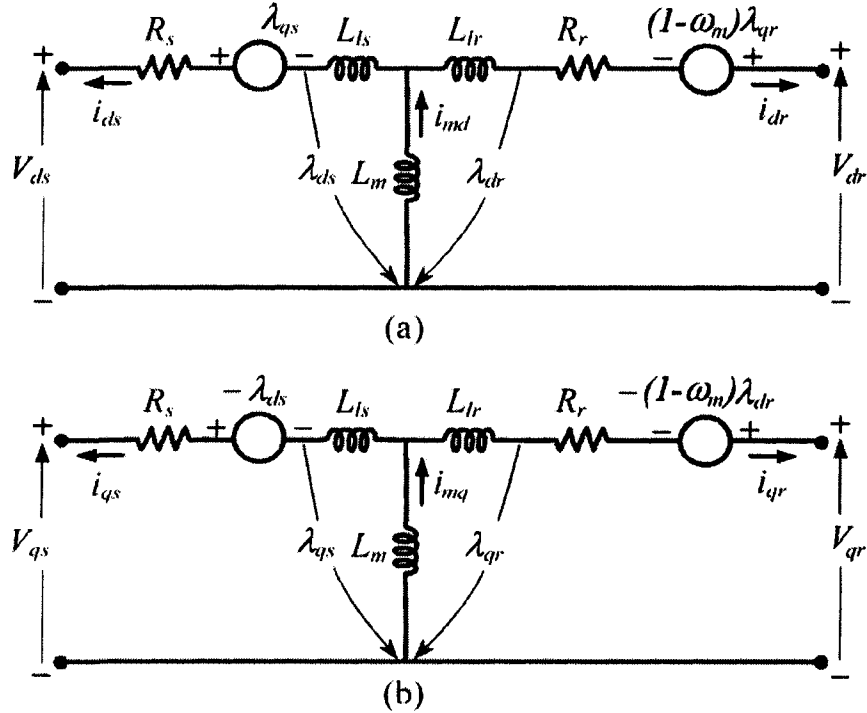


**Fig. 3.8: Equivalent circuits of the induction generator in a synchronously rotating reference frame.**

**(a) d-axis equivalent circuit. (b) q-axis equivalent circuit.**

The stator electrical input power to the induction machine during motoring operation or the stator electrical output power in generating mode is given by

$$P_e = \frac{3}{2} (I_{ds} V_{ds} + I_{qs} V_{qs}) \tag{3.8}$$

The electromagnetic torque developed by the machine is given by



$$T_e = \frac{3}{2} \frac{P}{2} \bar{\lambda}_m \times \bar{I}_r \quad (3.9)$$

where

$\bar{\lambda}_m$  air gap flux linkage

$\bar{I}_r$  rotor current vector

$P$  number of poles of the induction machine.

Equation (3.9) can be rewritten as

$$T_e = \frac{3}{2} \frac{P}{2} L_m (I_{qs} I_{dr} - I_{ds} I_{qr}) \quad (3.10)$$

The mechanical equation in the motoring region is

$$T_e = J \frac{d\omega_m}{dt} + B\omega_m + T_m \quad (3.11)$$

and in the generating region it is given as

$$T_m = J \frac{d\omega_m}{dt} + B\omega_m + T_e \quad (3.12)$$

where

$T_m$  mechanical torque in the shaft, Nm.

$T_e$  electromagnetic torque, Nm.

$\omega_m$  mechanical shaft speed, rad/sec.

$B$  friction coefficient, Nm/rad/sec.

$J$  inertia coefficient, Kg.m<sup>2</sup>.

### 3.4 Saturation in induction machine

It is well known that saturation takes place in almost all electrical machines and induction machines are no exception. In order to achieve a better representation of the induction machines, saturation should be included in the machine model. The performance of saturated induction machines and the accurate calculation of the stator and rotor parameters depend significantly on the saturation conditions of their main flux and leakage flux paths. It has been found that the inclusion of the saturation effects gives more accurate and realistic results [7]-[13].

### 3.4.1 Main flux saturation

A model of induction motors considering the main flux saturation can be developed using the unsaturated model developed in the previous section. In this approach, the unsaturated magnetizing inductance  $L_m$  in (3.5)-(3.7) is replaced by its corresponding saturated value. The saturated magnetizing inductance,  $L_{ms}$ , is obtained by modifying the corresponding unsaturated value,  $L_m$ , with a saturation factor,  $K_m$ , corresponding to the saturation condition. The total magnetizing current,  $i_m$ , is used to locate the operating point on the saturation characteristic. This total magnetizing current can be calculated using:

$$i_m = \sqrt{i_{md}^2 + i_{mq}^2} \quad (3.13)$$

where  $i_{md} = i_{ds} + i_{dr}$ ,  $i_{mq} = i_{qs} + i_{qr}$ .

### 3.4.2 Leakage flux saturation

For better representation of the induction machine, saturation representation should also include the variation in the stator and rotor leakage inductances due to saturation in the leakage flux paths. To represent the effect of saturation in the leakage flux paths, the stator and rotor leakage inductances ( $L_{ls}$ ,  $L_{lr}$ ) are separated into their saturated components ( $L_{ls-s}$ ,  $L_{lr-s}$ ) and unsaturated components ( $L_{ls-u}$ ,  $L_{lr-u}$ ). The saturated components of the inductances represent leakage flux that concentrate in the slot tooth tips which saturate and limit the magnetic field at the slot mouth. The unsaturated portions of the inductances represent end leakage and peripheral leakage [14], [15].

## 3.5 Experimental determination of machine parameters and saturation characteristics

### 3.5.1 Unsaturated machine parameters

The machine used in the investigations of this paper is a laboratory 3-phase wound-rotor type induction motor rated at ¼ hp, 208 V, 60 Hz. The unsaturated machine parameters have been obtained by performing the no-load and locked rotor tests using method 4 as described in the impedance tests section in IEEE Std. 112-2004 [16]. The no-load test is performed by running the machine as a motor at rated voltage and

frequency with no connected load. Since the impedance of a wound-rotor motor varies with the position of the rotor relative to the stator, it is therefore necessary to determine the rotor position that results in an average value of impedance when performing a locked-rotor impedance test. The rotor of a wound-rotor motor shall be blocked so that it cannot rotate freely, but can be moved; and the impressed voltage shall be increased gradually until a current of approximately rated value is obtained. Voltage and current on all phases shall be read and recorded, and the voltage in the different phases shall be balanced. Holding the same voltage, the rotor shall be turned slowly and the minimum and maximum values of current during a complete cycle shall be recorded. The rotor shall then be blocked for the impedance test on the position that gives a current equal to the average of the minimum and maximum values previously recorded. The experimental setup configuration for determining the machine parameters is as shown in Fig. 3.9. The parameters of the laboratory wound-rotor induction machine used in the investigations are obtained from these tests and are presented in Table 3.1. The test results confirm with the ones provided by the manufacturer.

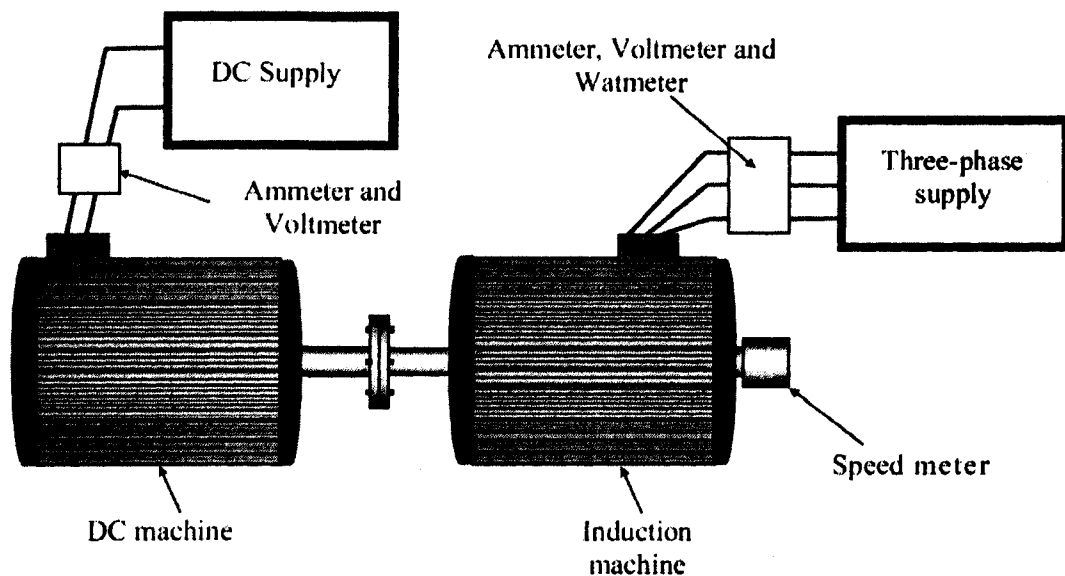


**Fig. 3.9: Experimental setup for determining the induction machine parameters.**

**Table 3.1: Parameters of the Wound-Rotor Induction Motor Used in the Investigations**

Rated power	0.25 hp
Rated voltage	120/208 V
Rated current	1.3 A
Rated frequency	60 Hz
Number of poles	4
$R_s$	12.5 $\Omega$
$R_r$	3.9 $\Omega$
$L_{ls}$	0.086 H
$L_{lr}$	0.15 H
$L_m$	0.849 H
Rated load torque	1.1 N.m
Rotor inertia	0.0024 kg.m <sup>2</sup>

### 3.5.2 Main flux saturation characteristics

In order to obtain the main flux saturation characteristics of the wound-rotor induction motor, the no-load generator test at synchronous speed is carried out. In the no-load generator test, the machine is fed by a three-phase controllable amplitude power source at rated frequency and driven at synchronous speed. The amplitude of the voltage source is varied and terminal voltage, current and active power are measured. It should be noted that, at this test condition the magnetizing current,  $i_m$  equals the stator current,  $i_s$ , since the rotor current,  $i_r$ , equals zero because the machine is driven at synchronous speed, the rotor circuit is considered as open circuit. This can be put in equations as follows:

$$\begin{aligned}
 \bar{I}_m &= \bar{I}_s + \bar{I}_r \\
 \bar{I}_r &= 0 \\
 \therefore I_m &= I_s
 \end{aligned} \tag{3.14}$$

Ignoring the stator leakage inductance, the magnetizing inductance is obtained by:

$$L_m = \frac{1}{\omega_o} \text{Im} \left( \frac{\bar{V}_t}{\bar{I}_s} \right) \tag{3.15}$$

The main flux saturation characteristics can be obtained by plotting  $L_m$  [using (3.15)] as a function of the magnetizing current  $i_m$  as shown in Fig. 3.10.

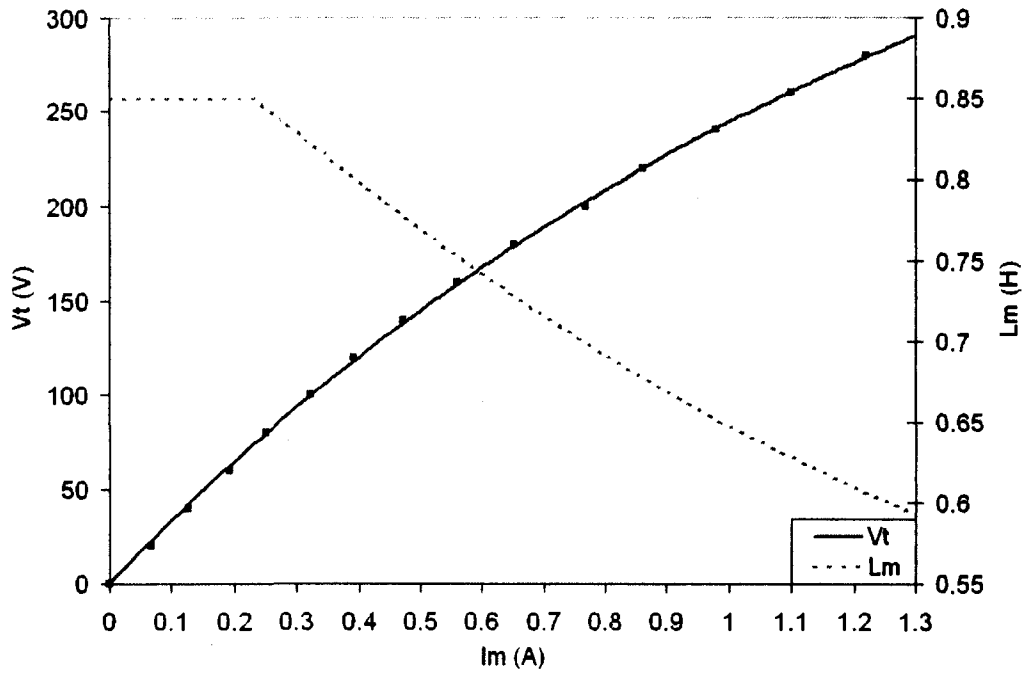


Fig. 3.10: Measured main flux saturation characteristics.

### 3.5.3 Stator and rotor leakage flux saturation characteristics

Experimental determination of the induction machine leakage inductances is very difficult. The wound-rotor type particularly has an advantage that it can be treated as a synchronous machine. This is achieved by connecting two of the three phases in series to form the field winding and excited by a dc voltage source. In this case, the leakage inductance  $L_l$  can be approximated by the Potier inductance  $L_p$ . However, it has been found in previous investigations that Potier inductance  $L_p$  measured at rated terminal voltage is usually higher than the unsaturated leakage inductance. This discrepancy could be as high as 100% [17]-[19]. Such a value of Potier inductance could not be a good approximation of the value of the leakage inductance.

To obtain accurate values of the leakage inductance  $L_l$ , an alternative testing method is adopted which was proposed in [18], [19]. In this proposed method, the terminal voltage/armature current characteristic curve ( $V_t/I_a$  curve) with the machine unloaded and unexcited is needed together with the d-axis open-circuit characteristic curve of the machine as shown in Fig. 3.11. When the machine is unloaded and unexcited, the armature current equals approximately its d-axis component since its q-axis component is nearly equal to zero. Neglecting the effect of the armature resistance of

the machine, which is usually very small, the machine phasor diagram can be drawn as shown in Fig. 3.12. This figure shows that the terminal voltage  $V_t$ , in this case, is equal to the d-axis synchronous inductance voltage drop  $I_a L_d$ . The difference between the terminal voltage  $V_t$  and the internal emf  $E_i$  is the armature leakage inductance voltage drop, namely  $I_a L_l$ . Thus,

$$\bar{V}_t = \bar{E}_i + \bar{I}_a \bar{X}_l \quad (3.16)$$

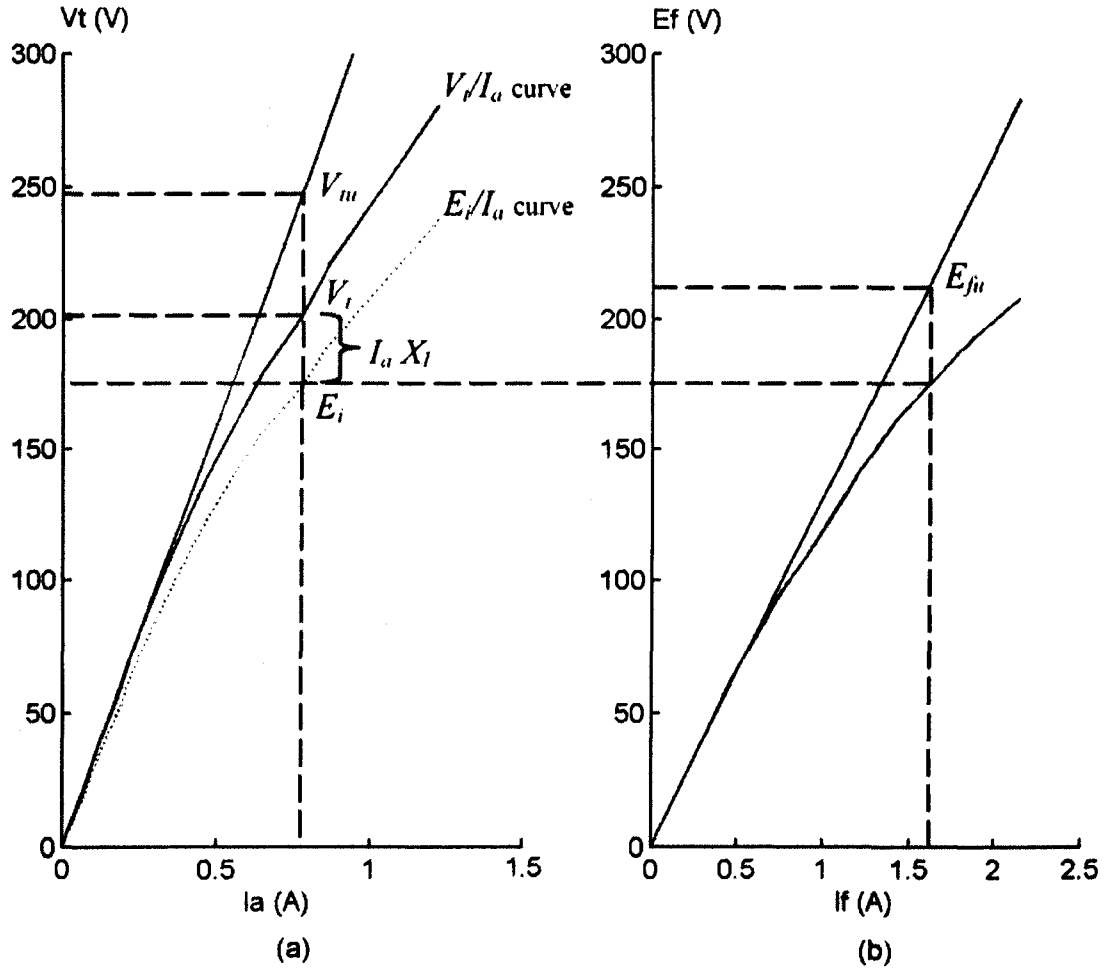


Fig. 3.11: Determination of the leakage reactance.

(a) The terminal voltage/armature current characteristic curve with the machine unloaded and unexcited. (b) The open circuit characteristic curve.

The internal emf  $E_i$  could be obtained from the d-axis open-circuit characteristic curve of this machine. In the “ $X_{md}$ -base” per unit system [20], the induced emf due to a certain armature current in per unit is by definition equal to the generated emf due to the

field current which has the same per unit value as this armature current. Thus, (3.16) could be rewritten as follows:

$$\bar{V}_t = \bar{E}_f + \bar{I}_a \bar{X}_l \quad (3.17)$$

where  $E_f$  can be found from the d-axis open-circuit characteristic curve of the machine if the field current is specified in per unit value. The field current  $I_f$  which has the same per unit value of the armature current  $I_a$  can be expressed as follows:

$$I_f = \frac{E_{fu}}{k} = \frac{V_{tu} - I_a X_l}{k} = \frac{I_a X_{du} - I_a X_l}{k} = \frac{I_a}{k} (X_{du} - X_l) \quad (3.18)$$

where  $k = \tan^{-1} \alpha$  is the slope of the air-gap line of the d-axis open-circuit characteristic curve and  $X_{du}$  and  $X_l$  are the unsaturated d-axis synchronous reactance and the armature leakage reactance respectively. Equation (3.18) shows that  $I_f$  is a function of  $X_l$ . In order to obtain a simpler expression for the armature leakage reactance, the following saturation factors can be used:

$$S_t = \frac{V_t}{V_{tu}} \quad (3.19)$$

$$S = \frac{E_f}{E_{fu}}$$

where  $S_t$  and  $S$  are the saturation factors found from the terminal voltage/armature current and the d-axis open-circuit characteristic curves respectively. Since  $V_{tu}$  can be substituted by  $I_a X_{du}$  and  $E_{fu}$  can be substituted by  $I_f k$ , (3.17) can be rewritten as

$$V_t = S_t V_{tu} = S_t I_a X_{du} \quad (3.20)$$

and

$$E_f = S E_{fu} = S I_f k \quad (3.21)$$

By substituting (3.16) into (3.19), it can be found that

$$E_f = S I_a (X_{du} - X_l) \quad (3.22)$$

By substituting (3.18) and (3.20) into (3.15), it results

$$S_t I_a X_{du} = S I_a (X_{du} - X_l) + I_a X_l \quad (3.23)$$

Equation (21) gives the following expression for  $X_l$

$$X_l = \frac{S_t - S}{1 - S} X_{du} \quad (3.24)$$

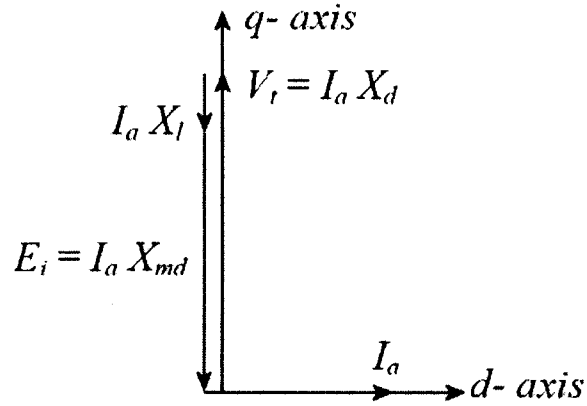


**Fig. 3.12: Phasor diagram of an unloaded unexcited synchronous machine.**

In (3.22),  $X_{du}$  is a constant. For a specific value of the armature current  $I_a$ ,  $S_t$  can be found from the terminal voltage/armature current characteristic curve. To find the corresponding value of  $S$  from the d-axis open-circuit characteristic curve, the field current  $I_f$  should be determined. As can be seen from (3.16), the value of this field current can be determined only if the armature leakage reactance  $X_l$  is known. Thus, an iterative technique has to be applied to calculate  $X_l$ . Figure 3.13 gives the flowchart of the program used for calculating the armature leakage reactances of a synchronous machine using (3.16) and (3.22). It should be noted that, in the linear regions of the open-circuit and the terminal voltage/armature current characteristic curves,  $X_l$  cannot be calculated by the proposed method since both  $S$  and  $S_t$  are equal to 1.



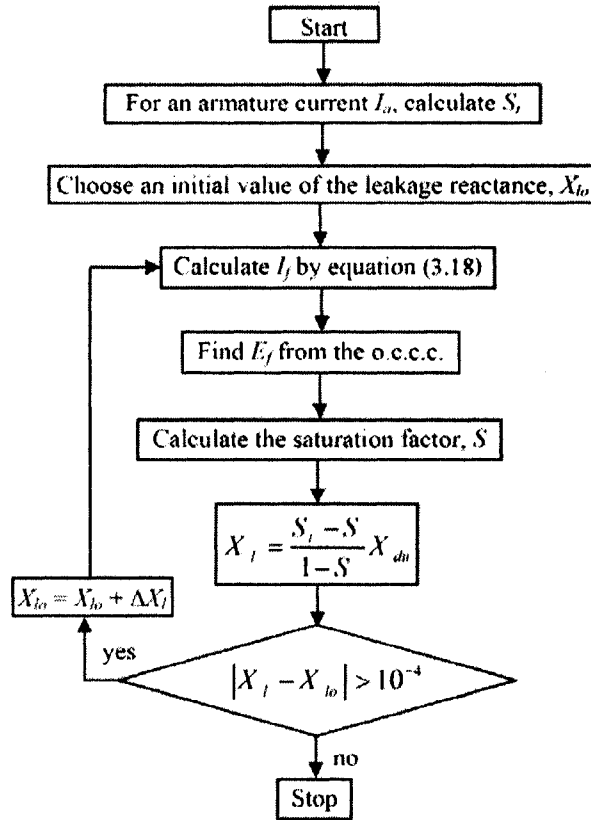


**Fig. 3.13: The flowchart of the program used for calculating the leakage reactance of wound-rotor Induction machine.**

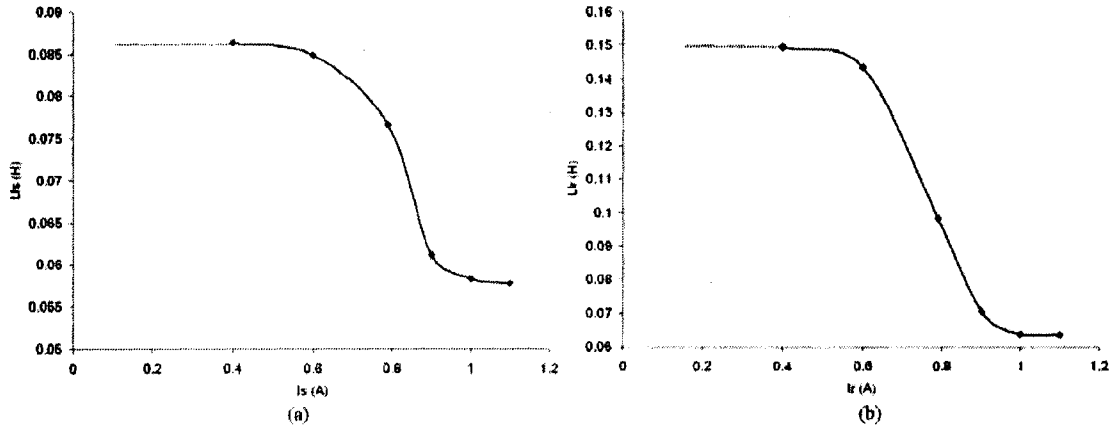


**Fig 3.14: Measured leakage reactance saturation characteristics.**

**(a) Stator leakage reactance. (b) Rotor leakage reactance.**

The experimental method discussed above is applied to the laboratory wound-rotor induction motor to obtain its stator and rotor leakage flux saturation characteristics. To obtain the stator leakage flux saturation characteristics, two phases of the rotor windings are connected in series and used as a field winding and the experimental method

discussed above is applied. Then, to obtain the rotor leakage flux saturation characteristics, two windings of the stator are connected in series and used as a field winding and the experimental method is carried out. The measured stator and rotor leakage flux saturation characteristics are shown in Fig. 3.14.

The machine model developed in this chapter, which includes the effect of both main and leakage saturation, is used in an ongoing research. It was used to investigate the effect of both main and leakage saturation on the dynamic performance of wind driven induction generator and the results were published in [21, 22]. It was also used to explore the effect of main and leakage saturation effect on the transient performance of induction motors and the results were published in [23, 24]. Two papers were published in the *Electric Power Systems Research Journal*, one was published in the *Journal of Wind Engineering* and another was published in the *IEEE PES General Meeting*.

### 3.6 References

- [1] P. L. Alger, The nature of induction machines, Gordon and Breach Inc., New York, 1965.
- [2] G. R. Slemon, Electric Machines and Drives, Addison-Wesley Publishing Company, New York, 1992.
- [3] A. E. Fitzgerald and JR. Charles Kingsley, Electric Machinery, McGraw-Hill Book Company, New York, 1961.
- [4] J. Rosenblatt, and M. H. Friedman, Direct and Alternating Current machinery CBS Publishers and Distributors, New Delhi, 2000.
- [5] M.G. Say, Alternating current machines, Pitman, London, 1983, pp. 260-262.
- [6] N. N. Hancock, Matrix Analysis of Electrical Machinery, Pergamon Press, New York, 1974.
- [7] P. Vas, "Generalized transient analysis of saturated a.c. machines," *Archiv Für Elektrotechnik*, vol. 63, pp. 57-62, 1981.
- [8] J. Robert, "On the transient performance of saturated electrical machines with cylindrical rotor," *Proceedings of the International Conference on Electrical Machines*, pp. 469-471, 1986.

- [9] J. M. F. de Jesus, "A model for saturation in induction machines," *IEEE Transactions on Energy Conversion*, vol. 3, pp. 682-688, 1988.
- [10] K. E. Hallenius, "On the theory of main flux saturation in smooth-air-gap electrical machines," *Archiv Für Elektrotechnik*, vol. 69, pp. 137-142, 1986.
- [11] E. Levi, "A unified approach to main flux saturation modelling in D-Q axis models of induction machines," *IEEE Transactions on Energy Conversion*, vol. 10, pp. 455-461, 1995.
- [12] P. Vas, W. Deleroi, and J. E. Brown, "Transient analysis of smooth-air-gap machines incorporating the effects of main and leakage flux saturation," *Proceedings of the International Conference on Electrical Machines*, pp. 269-272, 1984.
- [13] D. Bispo, L. Martins, Neto, J. T. de Resende, and D. A. de Andrade, "A new strategy for induction machine modeling taking into account the magnetic saturation," *IEEE Transactions on Industry Applications*, vol. 37, pp. 1710-1719, 2001.
- [14] P. Kundur, *Power System Stability and Control*, New York: McGraw-Hill, 1993.
- [15] G. J. Rogers and D. S. Benaragama, "An induction motor model with deep-bar effect and leakage inductance saturation," *Archiv Für Elektrotechnik*, vol. 60, pp. 193-201, 1978.
- [16] *IEEE Standard Test Procedure for Polyphase Induction Motors and Generators*, IEEE Standard 112-2004, 2004.
- [17] L. A. March, and S. B. Crary, "Armature leakage reactance of synchronous machines," *AIEE Transactions*, vol. 54, pp. 378-381, 1935.
- [18] J. Wu, "Theoretical and experimental investigations of the cross-magnetizing phenomenon in saturated synchronous machines," Masters thesis, University of Saskatchewan, 1989.
- [19] A. M. El-Serafi, and J. Wu, "A new method for determining the armature leakage reactance of synchronous machines," *IEEE Transactions on Energy Conversion*, vol. 6, no. 1, pp. 120-125, March 1991.
- [20] A. W. Rankin, "Per unit impedances of synchronous machines," *AIEE Transactions*, vol. 64, pp. 839-841, 1945.

- [21] Hany M. Jabr, Narayan C. Kar, "Effects of main and leakage flux saturation on the transient performances of doubly-fed wind driven induction generator," *Electric Power Systems Research Journal*, vol.77, no.8, pp.1019-1027, 2007
- [22] Hany M. Jabr, Narayan C. Kar, "Fuzzy logic based vector control of a doubly-fed induction generator in wind power application," *Journal of Wind Engineering*, vol. 30, no. 3, pp. 201-224, May 2006.
- [23] Hany M. Jabr, Narayan C. Kar, "Leakage flux saturation effects on the transient performance of wound-rotor induction motor," paper accepted for publication in the *Electric Power Systems Research Journal*, doi:10.1016/j.epsr.2007.11.004.
- [24] Hany M. Jabr, Narayan C. Kar, "Starting performance of saturated induction motors," *Proc. of the IEEE PES General Meeting*, Tampa, Fl. USA, 2007.

## **4 Field Orientation Control**

### **4.1 Introduction**

Separately excited dc drives are simpler in control because they independently control flux, which, when maintained constant, contributes to an independent control of torque. This is made possible with separate control of field and armature currents which, in turn, control the field flux and the torque independently.

Moreover, the dc motor control requires only the control of the field or armature current magnitudes, providing a simplicity not possible with ac machine control. By contrast, ac induction motor drives require a coordinated control of stator current magnitudes, frequencies, and their phases, making it a complex control. As with the dc drives, independent control of the flux and torque is possible in ac drives. The stator current phasor can be resolved, say, along the rotor flux linkages. The component along the rotor flux linkages is the field-producing current, but this requires the position of the rotor flux linkages at every instant; note that this is dynamic, unlike in the dc machine. If this is available, then the control of ac machines is very similar to that of separately-excited dc machines. The requirement of phase, frequency, and magnitude control of the currents and hence of the flux phasor is made possible by inverter control. The control is achieved in field coordinates (hence the name of this control strategy, field-oriented control); sometimes it is known as vector control, because it relates to the phasor control of the rotor flux linkages.

Vector control made the ac drives equivalent to dc drives in the independent control of flux and torque and superior to them in their dynamic performance. These developments positioned the ac drives for high performance applications, hitherto reserved for separately-excited dc motor drives. This chapter describes the basic principles, derivation and design and implementation of the vector control scheme.

The objective of field-oriented or vector control is to establish and maintain an angular relationship between the stator current space vector and one internal field vector, usually rotor flux or stator flux. This angular relationship may be achieved by regulating

the slip of the machine to a particular value that will fix the orientation through feed-forward on-line calculations. In this approach, often called indirect vector control (IVC), rotor flux is aligned with the d-axis. IVC is very popular for industrial drives: it is inherently four-quadrant work until zero speed and is suitable for speed-control loop but highly dependent on machine parameters. Under flux-aligned conditions along the d-axis of the synchronous rotating reference frame, the stator current is decoupled into two components;  $i_{qs}$  is proportional to machine electrical torque whereas  $i_{ds}$  is proportional to the machine flux, similarly to a DC machine control. Therefore, field orientation implies that on-line transformation of machine variables take into account a hypothetical rotating frame equivalent to a DC machine. By real-time transformation back to the three-phase stationary frame, impressed stator currents will impose a DC-like transient response.

Field orientation may also be achieved by on-line estimation of the field vector position, and usually the stator-flux will be aligned with the d-axis. Under this approach, called direct vector control (DVC), the control is less sensitive to parameters. It is dependent only on the stator resistance, which is easier to correct. It is very robust due to real-time tracking of machine parameter variation with temperature and core saturation, but it typically does not work at zero shaft speed. For induction generator applications, DVC seems to be a more effective approach because zero speed operation is not required.

To explain the principle of vector control, an assumption is made that the position of the rotor flux linkages phasor,  $\lambda_r$ , is known.  $\lambda_r$  is at  $\theta_f$  from a stationary reference,  $\theta_f$  is referred to as field angle hereafter, and the three stator currents can be transformed into d and q axes currents in the synchronous reference frames by using the transformation

$$\begin{bmatrix} i_{ds} \\ i_{qs} \end{bmatrix} = \frac{2}{3} \begin{bmatrix} \cos \theta_f & \cos \left( \theta_f - \frac{2\pi}{3} \right) & \cos \left( \theta_f + \frac{2\pi}{3} \right) \\ \sin \theta_f & \sin \left( \theta_f - \frac{2\pi}{3} \right) & \sin \left( \theta_f + \frac{2\pi}{3} \right) \end{bmatrix} \begin{bmatrix} i_{as} \\ i_{bs} \\ i_{cs} \end{bmatrix} \quad (4.1)$$

from which the stator current phasor,  $i_s$ , is derived as

$$i_s = \sqrt{i_{ds}^2 + i_{qs}^2} \quad (4.2)$$

and the stator phasor angle is

$$\theta_s = \tan^{-1} \left( \frac{i_{qs}}{i_{ds}} \right) \quad (4.3)$$

where  $i_{ds}$  and  $i_{qs}$  are the d and q axes currents in the synchronous reference frames that are obtained by projecting the stator current phasor on the d and q axes, respectively. That is evident from Fig. 4.1 which shows that the current phasor magnitude remains the same regardless of the reference frame chosen to view it. The current phasor  $i_s$  produces the rotor flux  $\lambda_r$ , and the torque  $T_e$ . The component of current producing the rotor flux phasor has to be in phase with  $\lambda_r$ . Therefore, resolving the stator current phasor along  $\lambda_r$ , reveals that the component  $i_f$  is the field-producing component, shown in Fig. 4.1. The perpendicular component  $i_T$  is hence the torque-producing component. By writing rotor flux linkages and torque in terms of these components as

$$\begin{aligned}\lambda_r &\propto i_f \\ T_e &\propto \lambda_r i_T \propto i_f i_T\end{aligned}\tag{4.4}$$

it can be seen that  $i_f$  and  $i_T$  have only dc components in steady state, because the relative speed with respect to that of the rotor field is zero: the rotor flux-linkages phasor has a speed equal to the sum of the rotor and slip speeds, which is equal to the synchronous speed. Orientation of  $\lambda_r$  amounts to considering the synchronous reference frames, and hence the flux- and torque-producing components of current are dc quantities. Because they are dc quantities, they are ideal for use as control variables; the bandwidth of the computational control circuits will have no effect on the processing of these dc control signals [1, 2].

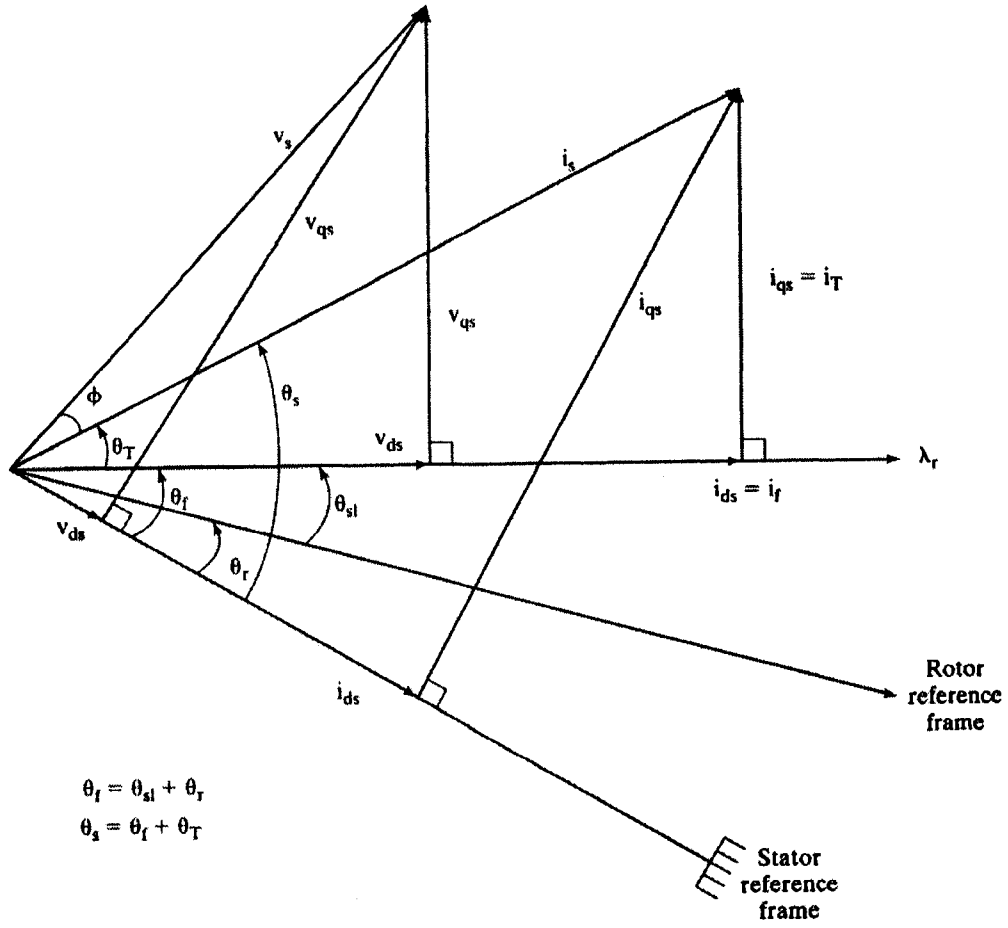


Fig. 4.1: Phasor diagram of the vector controller.

Then, the acquiring of the instantaneous rotor flux phasor position,  $\theta_f$ , is crucial to the implementation of vector control. This field angle can be written as

$$\theta_f = \theta_r + \theta_{sl} \quad (4.5)$$

where  $\theta_r$  is the rotor position and  $\theta_{sl}$  is the slip angle. In terms of the speeds and time, the field angle is written as

$$\theta_f = \int (\omega_r + \omega_{sl}) dt = \int \omega_s dt \quad (4.6)$$

Vector-control schemes are classified according to how the field angle is acquired. If the field angle is calculated by using terminal voltages and currents or Hall sensors or flux-sensing windings, then it is known as direct vector control. The field angle can also be obtained by using rotor position measurement and partial estimation with only machine parameters but not any other variables, such as voltages or currents; using this field angle leads to a class of control schemes known as indirect vector control.



## 4.2 Vector control of DFIG

The vector control techniques allow decoupled or independent control of both active and reactive power. These techniques are based on the concept of d-q controlling in different reference frames, where the current and the voltage are decomposed into distinct components related to the active and reactive power. In this work, the stator flux oriented rotor current control, with decoupled control of active and reactive power, is adopted.

The control schemes for the doubly-fed induction machine are expected to track a prescribed maximum power curve, for maximum power capturing and to be able to control the reactive power generation. These control objectives must be achieved with adequate stability of the system which also includes the power converter and the dc link [3, 4]. The total active and reactive power generated can be obtained from the stator voltage and current and can be expressed as

$$P_s = \frac{3}{2} |V_s| I_{qs} \quad (4.7.a)$$

$$Q_s = \frac{3}{2} |V_s| I_{ds} \quad (4.7.b)$$

The field orientation control is based on the field d-q model, where the reference frame rotates synchronously with respect to the stator flux linkage, with the d-axis of the reference frame instantaneously overlaps the axis of the stator flux. In short,  $\omega = \omega_e$  and  $\lambda_{qs} = 0$ . In such case the following expressions are obtained:

$$\begin{aligned} \lambda_{qs} &= X_s I_{qs} + X_m I_{qr} = 0 \\ \therefore I_{qs} &= -\frac{X_m}{X_s} I_{qr} \end{aligned} \quad (4.8)$$

Using (4.8) and the active power equation (4.7.a), the equation of the active power can be expressed as follows:

$$P_s = -\frac{3}{2} |V_s| \frac{X_m}{X_s} I_{qr} \quad (4.9)$$

The d-axis component of the stator current can be written as

$$\begin{aligned}
I_{ds} &= I_{md} - I_{dr} \\
&= \frac{|V_s|}{2\pi f_s X_m} - I_{dr}
\end{aligned} \tag{4.10}$$

Using (4.10) and the reactive power equation (4.7.b), the equation of the reactive power can be expressed as follows:

$$Q_s = \frac{3}{2} |V_s| \left( \frac{|V_s|}{2\pi f_s X_m} - I_{dr} \right) \tag{4.11}$$

Therefore, the d-axis component of the rotor current,  $i_{dr}$  can be controlled to regulate the stator reactive power while the q-axis component of the rotor current,  $i_{qr}$  can be controlled to regulate the stator active power and the generator speed. As a result, the control of the stator active power  $P_s$  via  $i_{qr}$  and the control of the stator reactive power  $Q_s$  via  $i_{dr}$  are essentially decoupled, and so a separate decoupler is not necessary to implement field orientation control for the slip power recovery. Flux control is generally unnecessary, (since it would maintain a constant level, restricted by the constant magnitude and frequency of the line voltage), while the control of reactive power becomes possible [4].

### 4.3 Control of line side converter

Through field oriented control of the machine side converter, the maximum power-speed profile can be tracked and stator output reactive power can be separately controlled. The dc link capacitor provides dc voltage to the machine side converter and any attempt to store active power in the capacitor would raise its voltage level. Thus to ensure stability of the system, power flow of the line side converter, as indicated in Fig. 4.2, should guarantee the following control objective:

$$P_l = P_r \tag{4.12}$$

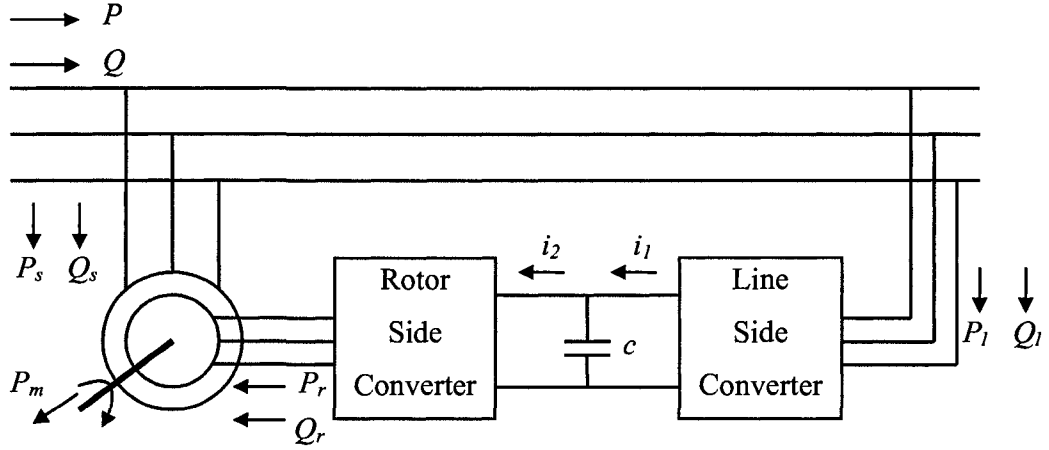


Fig. 4.2: Doubly-fed induction generator.

The dc link dynamic equation can be written as

$$c \frac{dV_{dc}}{dt} = i_1 - i_2 \quad (4.13)$$

in which  $V_{dc}$  is the dc bus voltage and  $c$  is the capacitance. Assuming no power losses for the converters,  $i_1$  and  $i_2$  can be derived as

$$i_1 = \frac{P_l}{V_{dc}} \quad (4.14)$$

$$i_2 = \frac{P_r}{V_{dc}} \quad (4.15)$$

Then from Eq. 4.13 through 4.15, as long as Eq. 4.12 is satisfied, the dc link voltage maintains stable, though small ripples might be present due to the instantaneous inequality between  $P_l$  and  $P_r$ , and a small variation may occur during transient as a result of energy transferring. As can be seen from Fig. 4.2, another result of Eq. 4.12 is that the overall generated active power equals to the electromagnetic active power, i.e.,

$$P = P_m = -\frac{3}{2} \frac{P}{2} \omega_r \lambda_{ds} i_{qr} \quad (4.16)$$

Reactive power flow constitutes another control objective

$$Q_l = Q^* - Q_s \quad (4.17)$$

where  $Q^*$  is the overall reactive power command required by the power network.

In the stator flux dq reference frame,

$$P_l = \frac{3}{2} (v_{qs} i_{dl} + v_{ds} i_{ql}) \quad (4.18)$$

$$Q_l = \frac{3}{2}(v_{qs}i_{dl} - v_{ds}i_{ql}) \quad (4.19)$$

Since  $v_{ds} \approx 0$ ,  $v_{qs} \approx v_m$ ,  $P_l$  and  $Q_l$  can be controlled by  $i_{ql}$  and  $i_{dl}$  respectively. In the same reference frame as determined by the stator flux,  $i_{ql}$  and  $i_{dl}$  are also field oriented currents, produced by the line side current regulated PWM converter.

#### 4.4 Structure of implementation

Based on the control strategy discussed above, Fig. 4.3 shows an implementation of the overall control system, which enables the slip power recovery system to function as both a VSCF generating system or variable speed drive system, and a reactive power compensator. Individual control of the machine side converter and of the line side converter and related feedback between the two converters are shown. For speed control purpose, a PID type speed loop generates the torque command; for position control purpose, another loop with position errors precedes the speed loop.

A current-regulated pulse-width-modulation (CRPWM) voltage source converter provides field oriented currents  $i_{dr}$  and  $i_{qr}$  to the rotor circuit, controlling stator reactive power and electromagnetic torque, respectively. Torque command is given by the turbine optimal torque-speed profile.

Another CRPWM voltage source converter is used to interface with the power network, possibly through a transformer. In the same dq reference frame as determined by the stator flux, its currents  $i_{ql}$  and  $i_{dl}$  are also field oriented, controlling  $P_l$  and  $Q_l$ , respectively. As discussed earlier,  $P_l$  is controlled through  $i_{ql}$  to stabilize the dc bus voltage and  $Q_l$  is controlled through  $i_{dl}$  to meet the overall reactive power command.

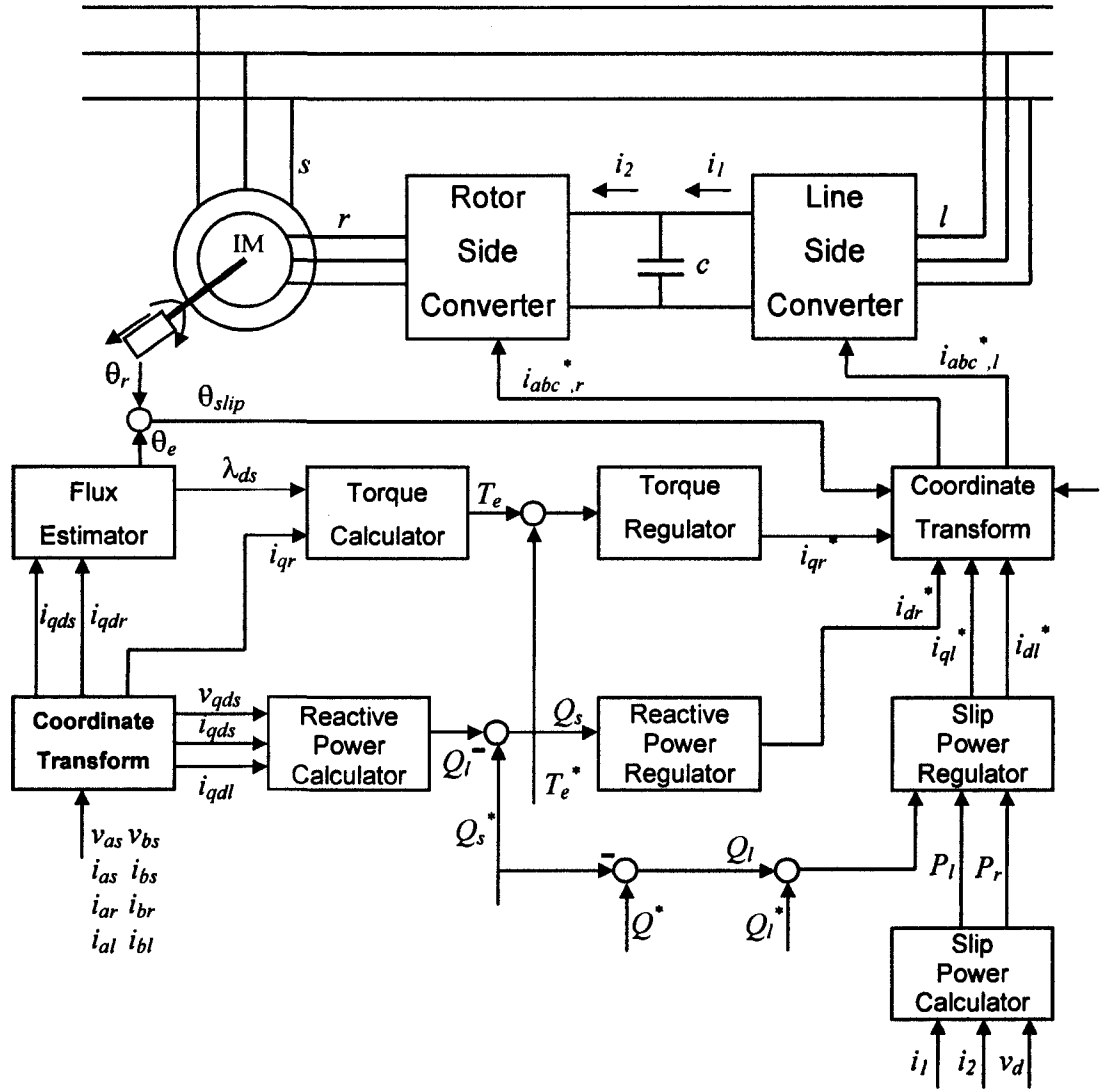


Fig. 4.3: Vector controller implementation of the doubly-fed induction generator.

## 4.5 References

- [1] M. G. Simões and F. A. Farret, *Renewable Energy Systems: Design and Analysis with Induction Generators*, CRC Press, 2004.
- [2] R. Krishnan, *Electric Motor Drives: Modeling, Analysis and Control*, Prentice Hall, New York, 2001.
- [3] Peter Vas, *Vector Control of AC Machines*, Oxford University Press, 1990.

- [4] Y. Tang and L. Xu, "A flexible active and reactive power control strategy for a variable speed constant frequency generating system," *IEEE Trans. on Power Electronics*, vol. 10, pp. 472-478, 1995.

## 5 Adaptive Controller

### 5.1 Introduction

The history of adaptive control goes back nearly 50 years [1]. The development of adaptive control started in the 1950's with the aim of developing adaptive flight control systems, although that problem was eventually solved by gain scheduling. Among the various solutions that were proposed for the flight control problem, the one that would have the most impact on the field was the so-called model-reference adaptive system (MRAS). Figure 5.1 depicts a typical MRAS where the specifications are in terms of a reference model and the parameters of the controller are adjusted directly to achieve those specifications. Although the original algorithm proved unstable, it led to the development during the 1970's and 1980's of algorithms with guaranteed stability, convergence and robustness properties.

There are two types of adaptive control, auto tuning, as shown in Fig. 5.1, and self tuning, as shown in Fig 5.2. In this work, the first was employed which is typically used for time invariant or very slowly varying processes. The proposed adaptive gain tuner is of the type shown in Fig. 5.1 in which simple adjustment mechanisms are employed.

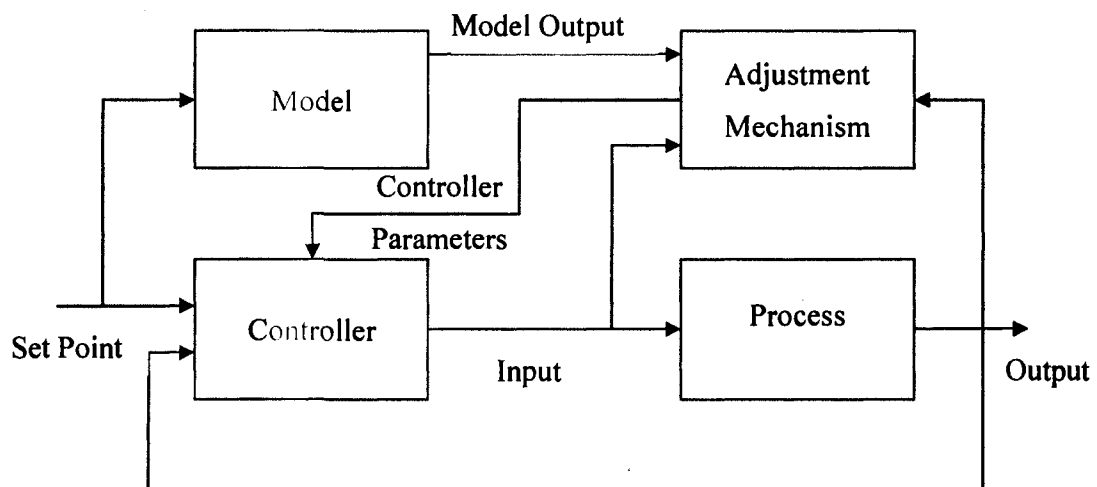


Fig. 5.1: Auto tuning adaptive controller.

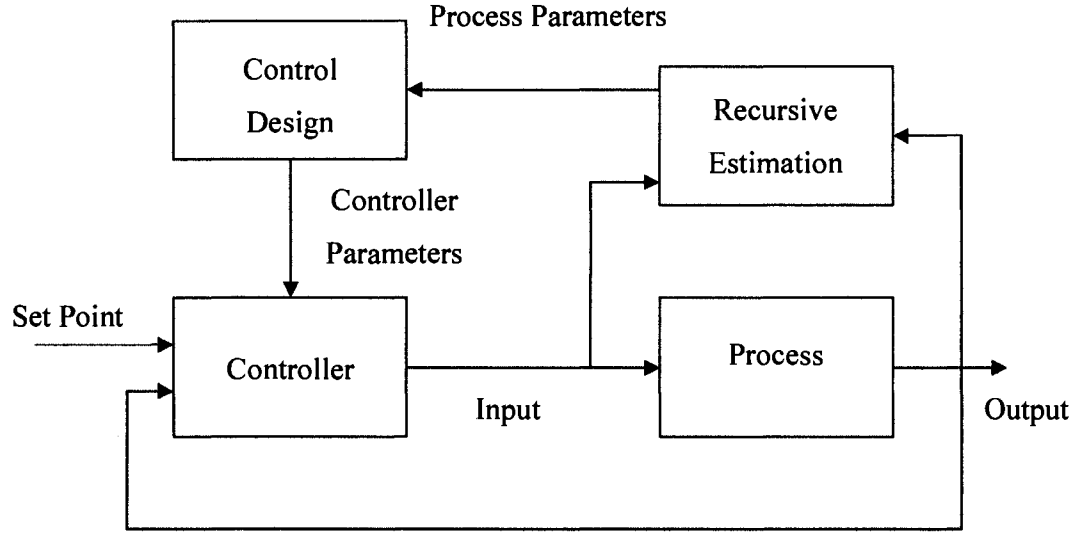


Fig. 5.2: Self tuning adaptive controller.

## 5.2 Adaptive PI gain scheduler

Traditional vector controllers, as used in [2,3], utilize a conventional PI controller with fixed proportional and integral gains determined by the zero/pole placement. Such controller gives a predetermined dynamic response and can't be changed easily. In this work, an adaptive controller is proposed which can schedule both the proportional and the integral gains depending on the value of the error signal.

In the proposed controller, the error signal is the difference between the set speed of the DFIG and the actual speed. The set speed is computed based on the measurement of the wind speed to track the maximum power curve. Then the absolute value of the error is used as the independent variable to compute both the integral and proportional gains. Different characteristics representing the variation in the proportional and the integral gains as a function of the absolute value of the error are used. The characteristics used in the investigations are described below.

The linear characteristics are expressed by the following equation:

$$K_{p,i} = a_1 |e(t)| + b_1 \quad (5.1)$$

where  $a_1$  and  $b_1$  are the coefficients of the linear function. The exponential characteristic has been expressed by the equation:

$$K_{p,i} = e^{b_2 |e(t)| + c_2} \quad (5.2)$$



where  $b_2$  and  $c_2$  are the coefficients of the exponential function. The piece wise linear function can be expressed as

$$K_{p,i} = \begin{cases} a_3 & |e(t)| < \gamma_1 \\ b_3 & \gamma_1 < |e(t)| < \gamma_2 \\ c_3 & |e(t)| > \gamma_2 \end{cases} \quad (5.3)$$

where  $a_3, b_3, c_3$  are the coefficients of the piece wise function and  $\gamma_1$  and  $\gamma_2$  are the threshold values that divide the error space. The second order characteristics are expressed by:

$$K_{p,i} = a_4 |e(t)|^2 + b_4 |e(t)| + c_4 \quad (5.4)$$

where  $a_4, b_4, c_4$  are the second order characteristics' coefficients. The fourth order characteristics are expressed by:

$$K_{p,i} = a_5 |e(t)|^4 + b_5 |e(t)|^3 + c_5 |e(t)|^2 + d_5 |e(t)| + f_5 \quad (5.5)$$

where  $a_5, b_5, c_5, d_5, f_5$  are the fourth order characteristics' coefficients.

The coefficients used in the above functions were selected such that, for the proportional gain ( $K_p$ ), a fast dynamic response, less overshoot and small settling time is desired. While for the integral gain ( $K_i$ ), it is required to reduce the overshoot and to eliminate the steady state error.

The advantage of gain scheduling is that the controller gains can be changed as quickly as the auxiliary measurements respond to parameter changes. Frequent and rapid changes of the controller gains, however, may lead to instability [4]; therefore, there is a limit as to how often and how fast the controller gains can be changed.

One of the disadvantages of gain scheduling is that the adjustment mechanism of the controller gains is precomputed off-line and, therefore, provides no feedback to compensate for incorrect schedules. Unpredictable changes in the plant dynamics may lead to deterioration of performance or even to complete failure. Another possible drawback of gain scheduling is the high design and implementation costs that increase with the number of operating points.

### 5.3 Implementation of the adaptive PI gain scheduler

The proposed adaptive PI gain scheduler is implemented. The system considered is a grid connected doubly-fed induction generator with the rotor circuit connected to the grid through back-to-back PWM voltage source converters as shown in Fig.5.3. The wind turbine considered has a power rating of 40kW. The turbine output power changes as a function of the wind speed as shown in Fig. 5.4. The wind speed is measured in order to set the set values for both the maximum output power and the corresponding generator speed in order to track the maximum power curve as shown in Fig. 5.5. These set values are then used to calculate the error signal which is the set value minus its corresponding measured actual value. The absolute value of the error signal is used to calculate the scheduled proportional and integral gains depending on the chosen characteristics (linear, exponential,...etc). This takes place in the “Adaptive PI gain scheduler.” The output of this block is the scheduled proportional and integral gains  $K_p$  and  $K_i$  respectively which are the inputs for the PI controller part of the vector controller. The error signal is also used, after scheduling the PI gains, as an input to the vector controller to generate the control signals  $v_{dr}$  and  $v_{qr}$ . The induction machine parameters used in the simulation are listed in Table 5.1.

**Table 5.1: DFIG parameters used in the simulation**

Rated power	40 kW	$R_s$	0.0083 pu
Rated voltage	460 V	$R_r$	0.0181 pu
Rated frequency	60 Hz	$L_{sl}$	0.0316 pu
$L_{mu}$	1.7845 pu	$L_{rl}$	0.0316 pu

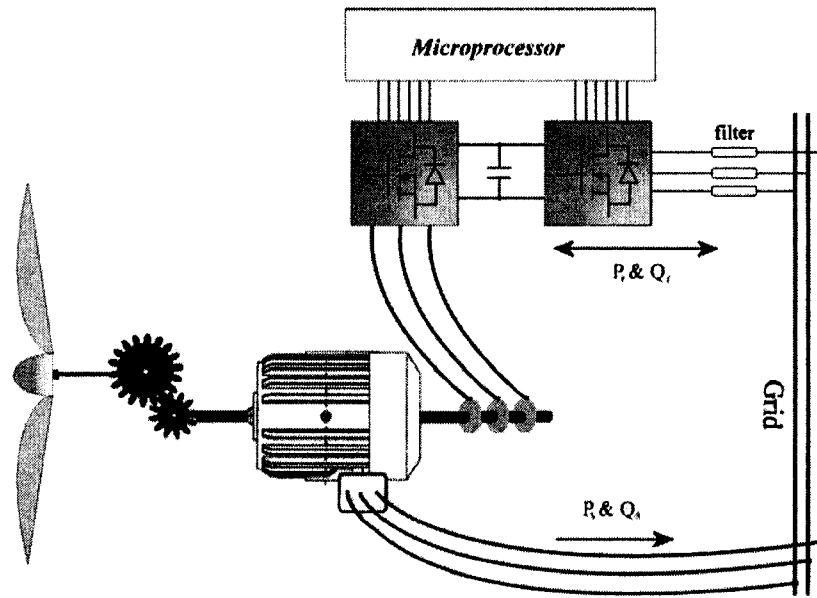


Fig. 5.3: Wind-driven DFIG system configuration.

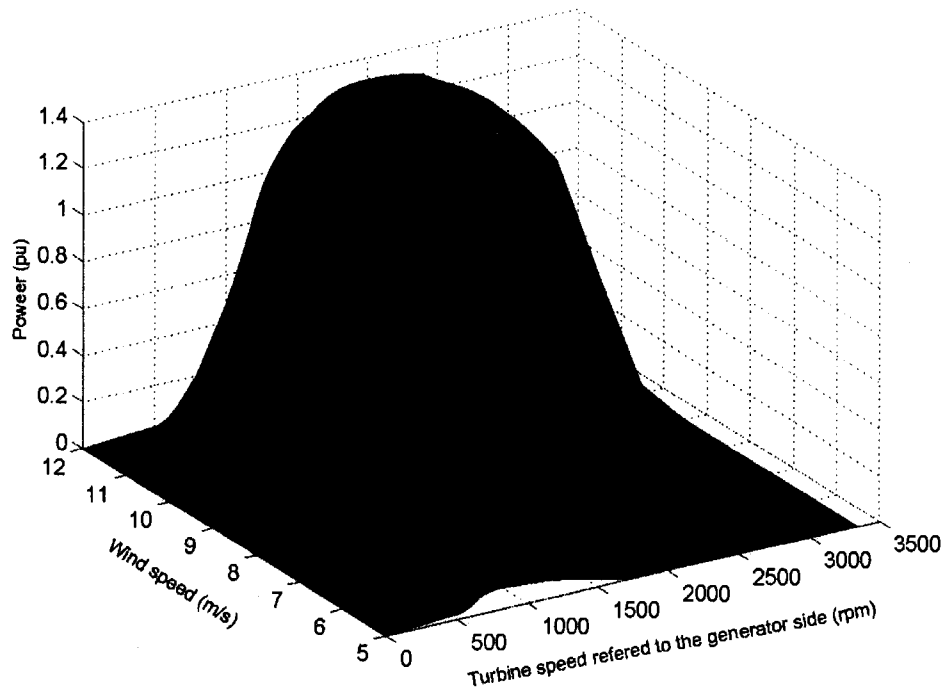


Fig. 5.4: Wind turbine power for different wind speeds showing maximum power point curve.

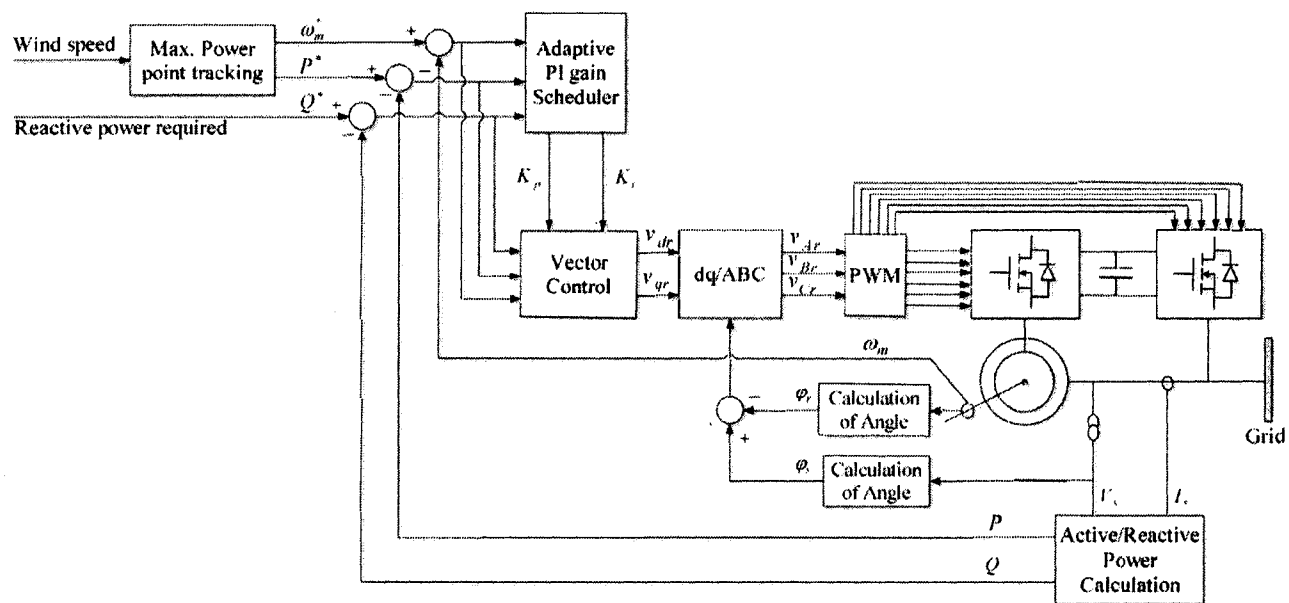


Fig. 5.5: Vector control configuration for slip energy recovery using the PI gain scheduler.

## 5.4 Simulation and results

Simulation has been performed on a saturated doubly-fed wind driven induction generator system incorporating the proposed PI gain scheduler for the vector control. The linear, piece wise linear, exponential, second- and fourth order characteristics for proportional and integral gains of the PI scheduler was selected as shown in Fig. 5.6. The coefficients for the equations (5.1)-(5.5) which describe the chosen characteristics are as follows:

1. Linear Characteristics (eq.(5.1)):

$$K_p : a_1 = 44, b_1 = 20.$$

$$K_i : a_1 = -45, b_1 = 50.$$

2. Exponential Characteristics (eq.(5.2)):

$$K_p : b_2 = 1.1632, c_2 = 2.9957.$$

$$K_i : b_2 = -2.3026, c_2 = 3.912.$$

3. Piece wise linear Characteristics (eq.(5.3)):

$$K_p : a_3 = 20, b_3 = 42.5, c_3 = 64, \gamma_1 = 0.1, \gamma_2 = 0.5.$$

$$K_i : a_3 = 50, b_3 = 27.5, c_3 = 5, \gamma_1 = 0.1, \gamma_2 = 0.5.$$

4. Second order Characteristics (eq.(5.4)):

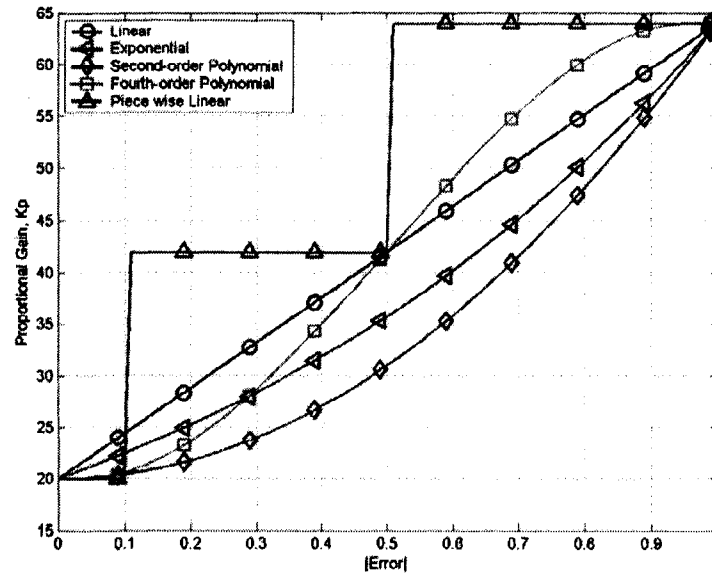
$$K_p : a_4 = 44, b_4 = 0, c_4 = 20.$$

$$K_i : a_4 = -45, b_4 = 0, c_4 = 50.$$

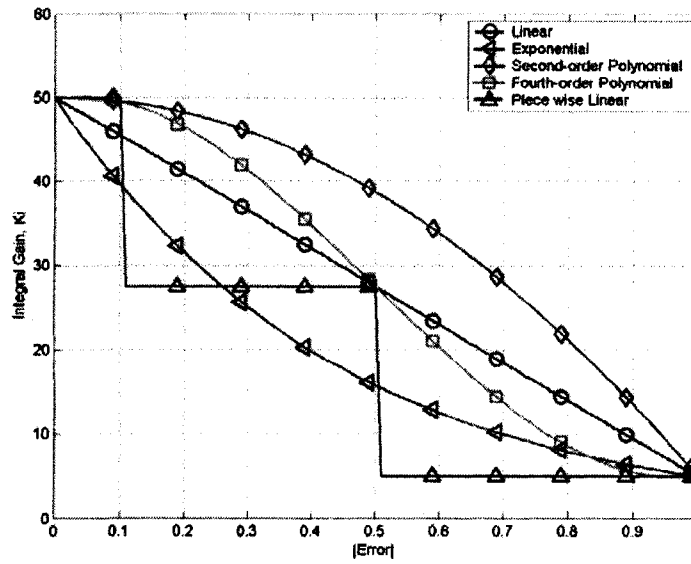
5. Fourth order Characteristics (eq.(5.5)):

$$K_p : a_5 = -7.281 \times 10^{-13}, b_5 = -109.156, c_5 = 163.732, d_5 = -10.80, f_5 = 20.$$

$$K_i : a_5 = 5.962 \times 10^{-13}, b_5 = 114.434, c_5 = -171.643, d_5 = 12.514, f_5 = 50.$$



(a)



(b)

**Fig. 5.6: PI gain scheduler characteristics.**

**(a) Proportional gain ( $K_p$ ). (b) Integral gain ( $K_i$ ).**

The performance of the vector controller with the proposed PI gain scheduler is compared to the vector controller employing constant proportional and integral gains. The fixed proportional gains are 64, 45, 5 and the fixed integral gains are 50, 22.5, 5. These values were chosen to be at the least, mid, and the most value of the error space. The results are show in Fig. 5.7. In this figure, the wind speed is 9m/s which corresponds to a set speed of 1600 rpm, i.e. 0.889 pu, according to Fig. 5.4 for the maximum power

generation. It can be seen from Fig. 5.7 that by using a controller that schedules its gains, we achieve faster dynamic response, less overshoot, less settling time and less steady state error. It can be noticed that both the piece wise linear and the exponential characteristics give the best performance.

The performance of the vector controller is investigated by measuring the rotor d- and q-axis currents, stator active and reactive power as well as the rotor active and reactive power flow as shown in Figs. 5.8 to 5.10.

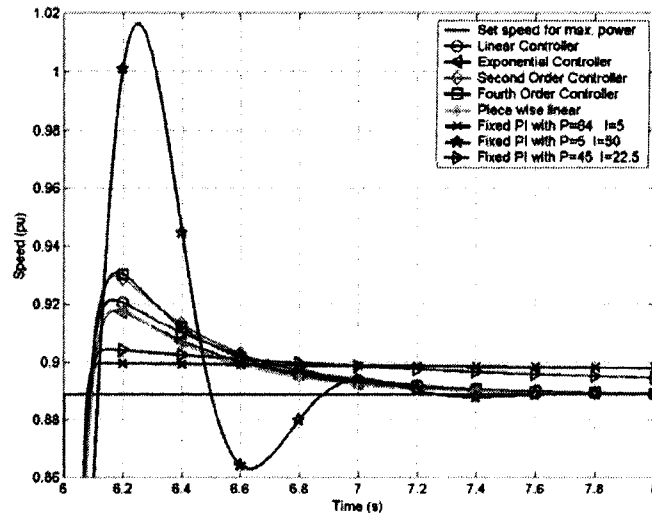


**Fig. 5.7: System speed response using the proposed adaptive controller compared to fixed PI controllers.**

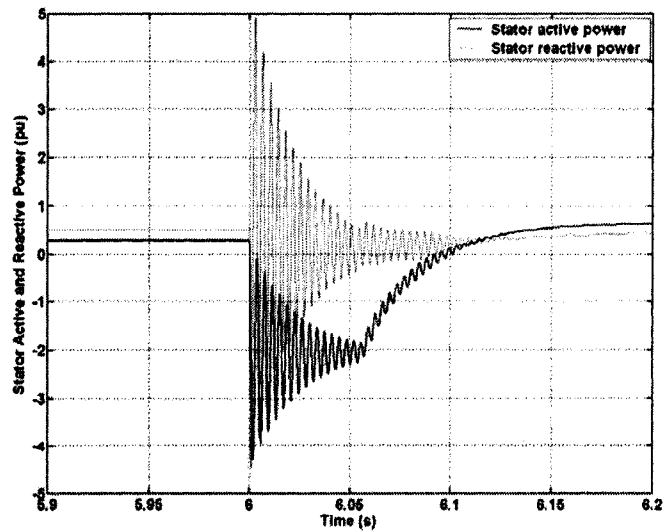


**Fig. 5.8: Stator active and reactive power generated.**

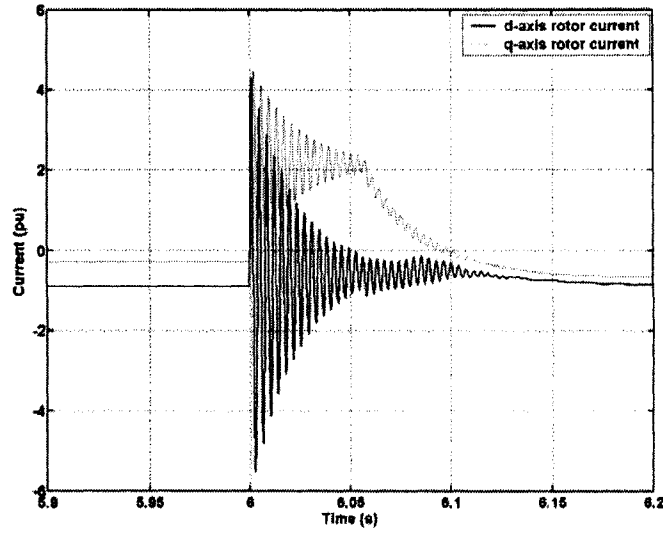


Fig. 5.9:  $d$ - and  $q$ - axis rotor current components.

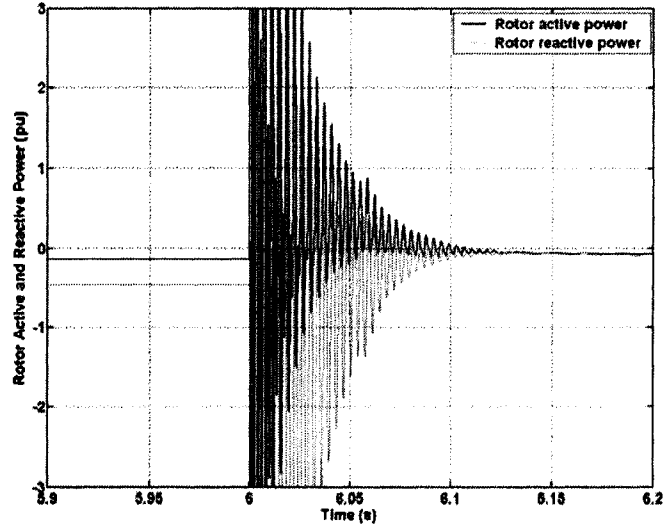


Fig. 5.10: Rotor active and reactive power flow.

Figure 5.8 shows the stator active and reactive power generated for  $Q_{set} = -0.5$  pu and  $P_{set} = -0.365$  pu which correspond to the maximum power at wind speed of 7m/s. At  $t=6$ sec., the wind speed increases to 9m/s, so the rotor speed increases to 1600 rpm and  $P_{set} = -0.61$  pu to maximize the output power. It can be seen from this figure that by using a controller that schedules its gains, a faster dynamic response with less overshoot, less settling time and less steady state error can be achieved.

Figure 5.9 shows the rotor  $d$ - and  $q$ -axis current components  $i_{dr}$  and  $i_{qr}$  respectively for the same scenario discussed above. It can be seen that to increase the amount of active power generated, an increase in the  $q$ -axis component of the rotor current  $i_{qr}$  is required,



on the other hand, there is no change in the d- axis component of the rotor current  $i_{dr}$  because there is no change in the set value of the reactive power generation. Figure 5.10 shows the active and reactive power flow to the rotor for the same operating conditions, i.e. fixed reactive power generation at 0.5 pu and the increase in the active power generated to track the maximum wind energy.

## 5.5 References

- [1] K. J. Astrom, "Adaptive control around 1960," *IEEE Control Systems Magazine*, vol. 16, no. 3 pp. 44–49, 1996.
- [2] R. Cárdenas and R. Peña, "Sensorless vector control of induction machines for variable-speed wind energy applications," *IEEE Trans. On Energy Conversion*, vol. 19, pp.196–205, 2004.
- [3] G. Poddar, A. Joseph, and A. K. Unnikrishnan, "Sensorless variable-speed controller for existing fixed-speed wind power generator with unity-power-factor operation," *IEEE Trans. On Industrial Electronics*, vol. 50, pp.1007–1015, 2003.
- [4] K. S. Tsakalis and P.A. Ioannou, *Linear Time Varying Systems: Control and Adaptation*, Prentice Hall, Englewood Cliffs, New Jersey, 1993.

## 6 Fuzzy Logic Controller

### 6.1 Introduction

Fuzzy logic controllers have been successfully applied to a variety of problems including image processing [1,2], power system faults diagnostic [3] and identification [4], motor control [5-7], faults diagnostic [8], variable speed wind power generators [8-14] and many others. Because of its multidisciplinary nature, fuzzy inference systems (FIS) are associated with a number of names, such as fuzzy-rule-based systems, fuzzy expert systems, fuzzy modeling, fuzzy associative memory, fuzzy logic controllers, and simply (and ambiguously) fuzzy systems.

Mamdani's fuzzy inference method is the most commonly seen fuzzy methodology. Mamdani's method was among the first control systems built using fuzzy set theory. It was proposed in 1975 by Ebrahim Mamdani [15] as an attempt to control a steam engine and boiler combination by synthesizing a set of linguistic control rules obtained from experienced human operators. Mamdani's effort was based on Lotfi Zadeh's 1973 paper on fuzzy algorithms for complex systems and decision processes [16]. Although the inference process described in the next few sections differs somewhat from the methods described in the original paper, the basic idea is much the same.

### 6.2 Overview on fuzzy logic

The point of fuzzy logic is to map an input space to an output space, and the primary mechanism for doing this is a list of *if-then* statements called rules. All rules are evaluated in parallel, and the order of the rules is unimportant. The rules themselves are useful because they refer to variables and the adjectives that describe those variables. Before you can build a system that interprets rules, you must define all the terms you plan on using and the adjectives that describe them.

#### 6.2.1 Membership functions

A *membership function* (MF) is a curve that defines how each point in the input space is mapped to a membership value (or degree of membership) between 0 and 1.

The only condition a membership function must really satisfy is that it must vary between 0 and 1. The function itself can be an arbitrary curve whose shape we can define as a function that suits us from the point of view of simplicity, convenience, speed, and efficiency.

The simplest membership functions are formed using straight lines. Of these, the simplest is the *triangular* membership function as shown in Fig. 6.1. This function is nothing more than a collection of three points forming a triangle. The *trapezoidal* membership function, shown in Fig. 6.1, has a flat top and really is just a truncated triangle curve. These straight line membership functions have the advantage of simplicity.

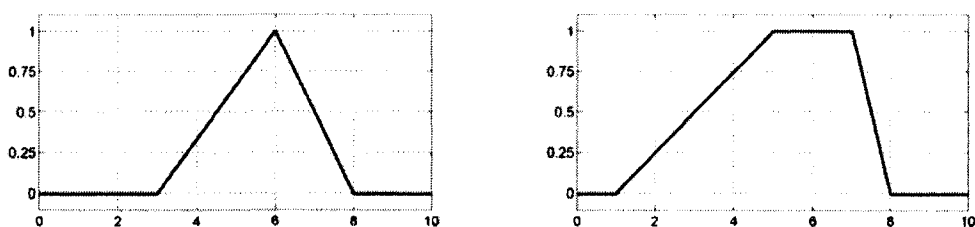


**Fig. 6.1: Triangular and trapezoidal membership functions.**

Two membership functions are built on the *Gaussian* distribution curve: a simple Gaussian curve and a two-sided composite of two different Gaussian curves as shown in Fig. 6.2.

The *generalized bell* membership function is specified by three parameters and shown in Fig. 6.2. The bell membership function has one more parameter than the Gaussian membership function, so it can approach a non-fuzzy set if the free parameter is tuned. Because of their smoothness and concise notation, Gaussian and bell membership functions are popular methods for specifying fuzzy sets. Both of these curves have the advantage of being smooth and nonzero at all points.

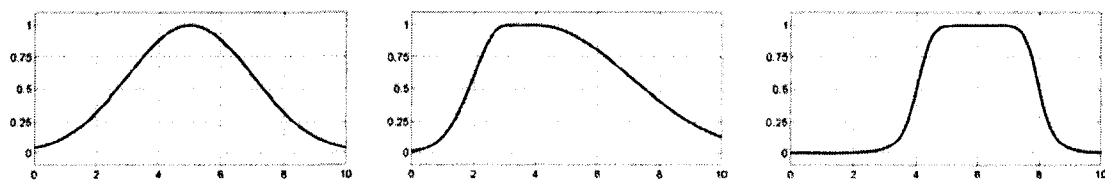


**Fig. 6.2: Gaussian, two-sided composite Gaussian and generalized bell membership functions.**

Although the Gaussian membership functions and bell membership functions achieve smoothness, they are unable to specify asymmetric membership functions, which

are important in certain applications. Next the *sigmoidal* membership function which is either open left or right. Asymmetric and closed (i.e. not open to the left or right) membership functions can be synthesized using two sigmoidal functions as shown in Fig.6.3.

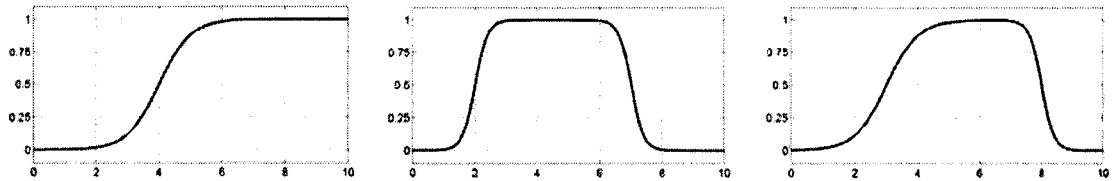


**Fig. 6.3: Sigmoidal based membership functions.**

Polynomial based curves account for several of the membership functions. Three related membership functions are the *Z*, *S*, and *Pi* curves, all named because of their shape and shown in Fig.6.4. The function *Z* is the symmetrical polynomial curve open to the left, *S* is the mirror-image function that opens to the right, and *Pi* is zero on both extremes with a rise in the middle as shown in Fig.6.4.

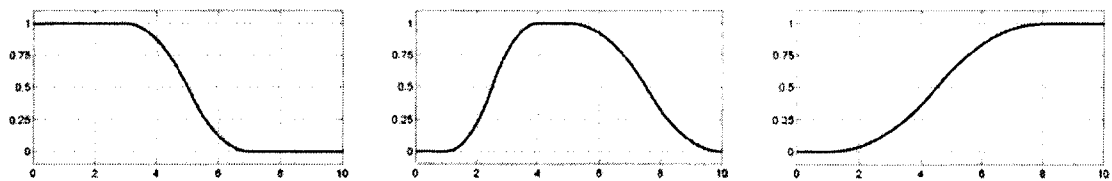


**Fig. 6.4: Z, S and Pi membership functions.**

The designer of the fuzzy inference system can also create his own membership functions. The selection is wide for those who want to explore the possibilities, but expansive membership functions are not necessary for good fuzzy inference systems.

## 6.2.2 Logical operations

The most important thing to realize about fuzzy logical reasoning is the fact that it is a superset of standard Boolean logic. In other words, if you keep the fuzzy values at their extremes of 1 (completely true), and 0 (completely false), standard logical operations will hold. As an example, consider the following standard truth tables.

Table 6.1: Truth tables for fuzzy logical operations.

A	B	$\min(A,B)$	A	B	$\max(A,B)$	A	$1 - A$
0	0	0	0	0	0	0	1
0	1	0	0	1	1	1	0
1	0	0	1	0	1		
1	1	1	1	1	1		

AND
OR
NOT

In fuzzy logic, the input values can be real numbers between 0 and 1. To solve this problem, the *min* operation resolves the statement  $A$  AND  $B$ , where  $A$  and  $B$  are limited to the range  $(0,1)$ , by using the function  $\min(A,B)$ . Using the same reasoning, you can replace the OR operation with the *max* function, so that  $A$  OR  $B$  becomes equivalent to  $\max(A,B)$ . Finally, the operation NOT  $A$  becomes equivalent to the operation  $\bar{A}$ . Notice how the previous truth table is completely unchanged by this substitution.

The next figure uses a graph to show the same information. In this figure, the truth table is converted to a plot of two fuzzy sets applied together to create one fuzzy set. The figure displays how the operations work over a continuously varying range of truth values  $A$  and  $B$  according to the fuzzy operations you have defined.

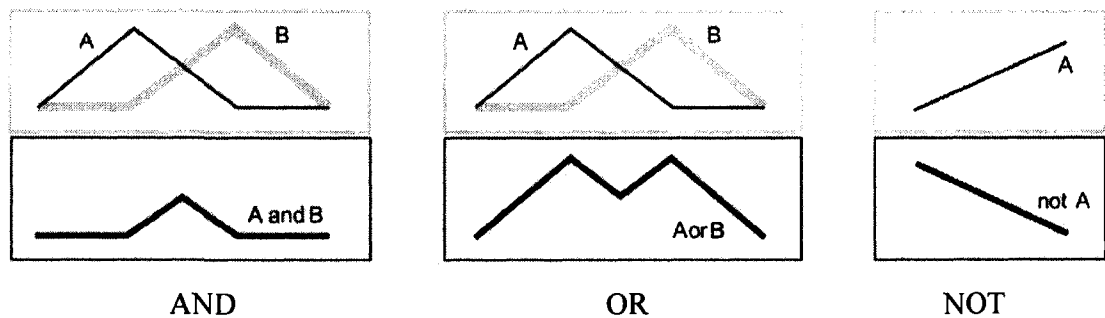


Fig. 6.5: Graphic interpretation of the fuzzy logic operations.

### 6.2.3 If-then rules

Fuzzy sets and fuzzy operators are the subjects and verbs of fuzzy logic. These if-then rule statements are used to formulate the conditional statements that comprise fuzzy logic.

A single fuzzy if-then rule assumes the form

**if  $x$  is  $A$  then  $y$  is  $B$**

where  $A$  and  $B$  are linguistic values defined by fuzzy sets on the ranges  $X$  and  $Y$ , respectively. The if-part of the rule “ $x$  is  $A$ ” is called the *antecedent* or premise, while the then-part of the rule “ $y$  is  $B$ ” is called the *consequent* or conclusion.

In general, the input to an if-then rule is the current value for the input variable and the output is an entire fuzzy set. This set will later be *defuzzified*, assigning one value to the output. The concept of defuzzification is described in the next section.

Interpreting an if-then rule involves distinct parts: first evaluating the antecedent (which involves *fuzzifying* the input and applying any necessary *fuzzy operators*) and second applying that result to the consequent (known as *implication*). It should also be noted that the antecedent of a rule can have multiple parts. In which case; all parts of the antecedent are calculated simultaneously and resolved to a single number using the logical operators described in the preceding section. The consequent of a rule can also have multiple parts. In which case; all consequents are affected equally by the result of the antecedent.

The consequent specifies a fuzzy set be assigned to the output. The *implication function* then modifies that fuzzy set to the degree specified by the antecedent. The most common ways to modify the output fuzzy set are truncation using the min function (where the fuzzy set is truncated) or scaling using the prod function (where the output fuzzy set is squashed).

### **6.3 Fuzzy inference system**

Fuzzy inference process comprises of five parts: fuzzification of the input variables, application of the fuzzy operator (AND or OR) in the antecedent, implication from the antecedent to the consequent, aggregation of the consequents across the rules, and defuzzification. These sometimes cryptic and odd names have very specific meaning that are defined in the following steps.

#### **6.3.1 Step 1: Fuzzify inputs**

The first step is to take the inputs and determine the degree to which they belong to each of the appropriate fuzzy sets via membership functions. The input is always a crisp

numerical value limited to the universe of discourse of the input variable and the output is a fuzzy degree of membership in the qualifying linguistic set (always the interval between 0 and 1). Fuzzification of the input amounts to either a table lookup or a function evaluation.

### **6.3.2 Apply fuzzy operator**

After the inputs are fuzzified, you know the degree to which each part of the antecedent is satisfied for each rule. If the antecedent of a given rule has more than one part, the fuzzy operator is applied to obtain one number that represents the result of the antecedent for that rule. This number is then applied to the output function. The input to the fuzzy operator is two or more membership values from fuzzified input variables. The output is a single truth value.

### **6.3.3 Apply implication method**

Before applying the implication method, you must determine the rule's weight. Every rule has a *weight* (a number between 0 and 1), which is applied to the number given by the antecedent. Generally, this weight is 1 and thus has no effect at all on the implication process. From time to time you may want to weight one rule relative to the others by changing its weight value to something other than 1. After proper weighting has been assigned to each rule, the implication method is implemented. A consequent is a fuzzy set represented by a membership function, which weights appropriately the linguistic characteristics that are attributed to it. The consequent is reshaped using a function associated with the antecedent (a single number). The input for the implication process is a single number given by the antecedent, and the output is a fuzzy set. Implication is implemented for each rule.

### **6.3.4 Aggregate all outputs**

Because decisions are based on the testing of all of the rules in a FIS, the rules must be combined in some manner in order to make a decision. Aggregation is the process by which the fuzzy sets that represent the outputs of each rule are combined into a single fuzzy set. Aggregation only occurs once for each output variable, just prior to the fifth and final step, defuzzification. The input of the aggregation process is the list of truncated

output functions returned by the implication process for each rule. The output of the aggregation process is one fuzzy set for each output variable. As long as the aggregation method is commutative (which it always should be), then the order in which the rules are executed is unimportant.

### **6.3.5 Defuzzify**

The input for the defuzzification process is a fuzzy set (the aggregate output fuzzy set) and the output is a single number. As much as fuzziness helps the rule evaluation during the intermediate steps, the final desired output for each variable is generally a single number. However, the aggregate of a fuzzy set encompasses a range of output values, and so must be defuzzified in order to resolve a single output value from the set. Perhaps the most popular defuzzification method is the centroid calculation, which returns the center of area under the curve. There are other defuzzification methods such as centroid, bisector, middle of maximum (the average of the maximum value of the output set), largest of maximum, and smallest of maximum [17].

## **6.4 *Implementation of fuzzy gain scheduler***

Fuzzy logic controllers are typically described by a relatively large number of parameters including the number of membership functions for each fuzzy variable, the shape and position of each membership function, the number of rules, the antecedents and consequents of each rule and the output defuzzification method [18]. This provides a large degree of freedom for designing high-performance controllers.

Traditionally, controllers have been designed and tested based upon a mathematical model of the system to be controlled. If the controller is non-adaptive, options for improving performance include retuning controller parameters, redesigning the controller or using a different type of controller. These methods can be difficult and time-consuming, especially if it is unrealistic to describe the troublesome qualities of the plant mathematically [19]. Several methods have been proposed to improve the performance of an existing control system by using fuzzy logic. Examples of these include fuzzy tuning of PID controller parameters [20], knowledge-based modification of references [21] and fuzzy resetting of control effort for PI-type fuzzy logic controllers [22].



The conventional PI controller is one of the most common approaches for speed control in industrial electrical drives in general, because of its simplicity, and the clear relationship existing between its parameters and the system response specifications. It is also the basis for many advanced control algorithms and strategies. The conventional PI controller fixed gains may perform well under some operating conditions but not all, because the involved processes are in general complex, time variant, with non-linearities and model uncertainties [18,20,21,23].

One of the most successful expert system techniques applied in a wide range of control applications has been fuzzy logic [24]. It can be combined with conventional PI controller, to build fuzzy self-tuning controllers, in order to achieve a more robust control [25]. The fuzzy adaptation can be built via updating fuzzy sets functions, fuzzy rules, or controller gains [26-28].

In this work, the later technique of using fuzzy inference system to update the PI controller gains is implemented. The two gains of the PI controller will be initialized using well-known conventional methods. Then, a fuzzy algorithm for tuning these two gains of the PI controller is proposed to keep good control performance, when parameter variations take place and/or when disturbances are present. This approach uses fuzzy rules to generate proportional and integral gains,  $K_p$ , and  $K_i$ . The design of these rules is based on a qualitative knowledge, deduced from extensive simulation tests of a conventional PI controller of the system for different values of  $K_p$  and  $K_i$ , with different operating conditions.

The proposed fuzzy PI gain scheduler has three inputs, each represents the error signal  $e(t)$  of the controlled variable. In this case the three controlled variables are the generator speed  $\omega$ , the generated active power  $P$  and reactive power  $Q$ . The set value of the active power is selected depending on the wind speed and according to the wind turbine characteristic curves to track the maximum power point in order to maximize the total power generation. Considering only one error signal, the proposed PI gain scheduler is as shown in Fig. 6.6.

The input signal has 9 membership functions while the outputs have 5 membership functions each. The fuzzy system has 9 rules and the defuzzification method employed is the center of area. The nine membership functions in the case of the speed controller are

designed as shown in Fig. 6.7 while in the case of the active and reactive power controllers are designed as shown in Fig. 6.8. Also, the five membership functions for the proportional gain  $K_p$  and the integral gain  $K_i$  in the case of the speed controller are designed as shown in Figs. 6.9 and 6.10 while they are designed as shown in Figs. 6.11 and 6.12 in the case of active and reactive power controllers. The nine fuzzy rules are the same for speed, active and reactive power controllers and are shown in Table 6.2.

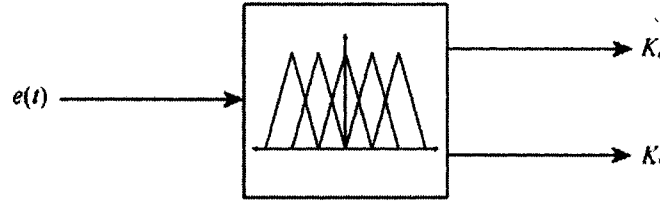


Fig. 6.6: Fuzzy PI gain scheduler.

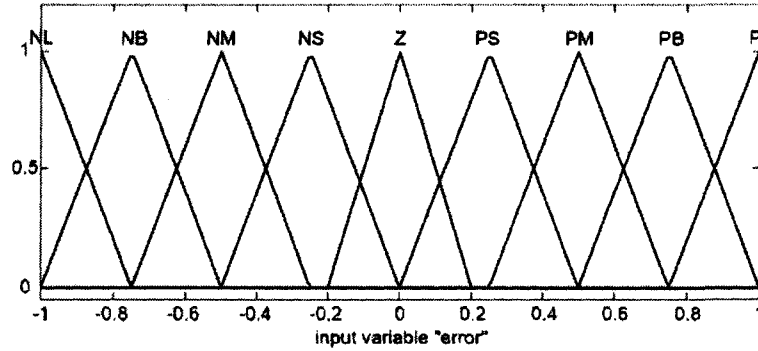


Fig. 6.7: Membership functions for the speed error input.

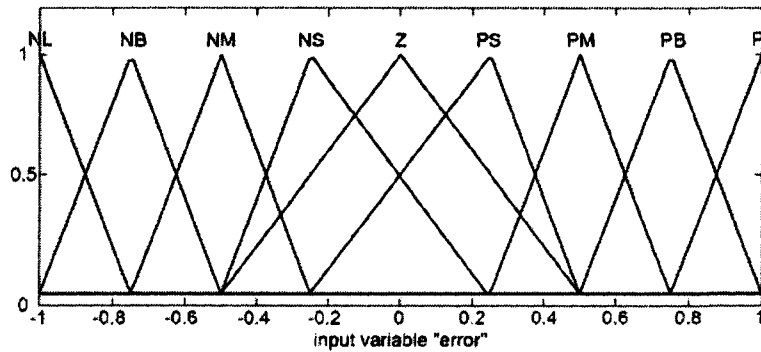
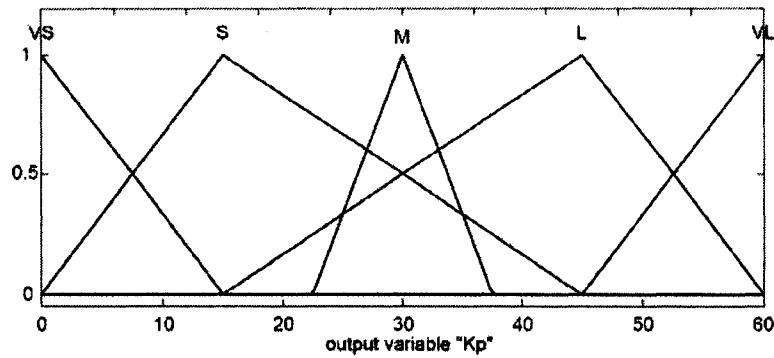


Fig. 6.8: Membership functions for the active and reactive power error inputs.

The first column of the rules table shows that the proportional gain  $K_p$  is more and more increased for large positive or negative speed error  $e$ . This will improve the speed rise time, but can lead to speed response with overshoot. From the second column of the

rules table, it can be seen that the integral gain  $K_i$  is more and more increased for lower positive or negative speed error  $e$ . The reasoning behind this is to avoid speed overshoots, and steady-state errors.



**Fig. 6.9: Membership functions for the proportional gain,  $K_p$ , of the speed controller.**

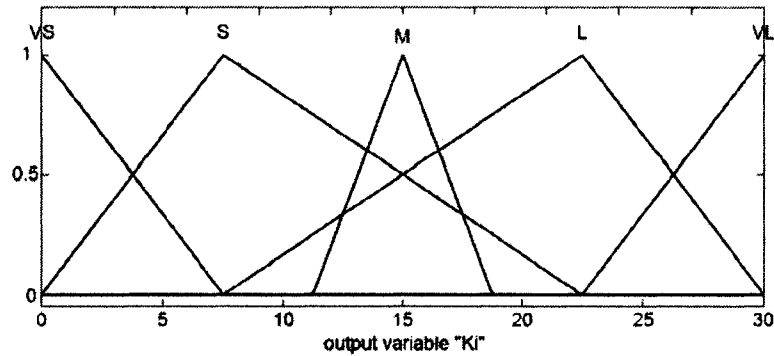


**Fig. 6.10: Membership functions for the integral gain,  $K_i$ , of the speed controller.**

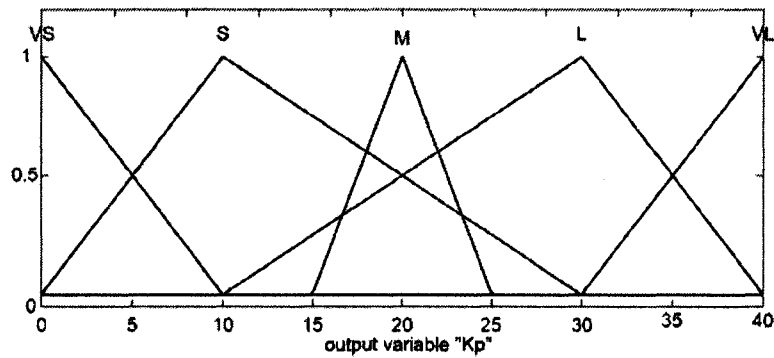


**Fig. 6.11: Membership functions for  $K_p$  of the active and reactive power controllers.**

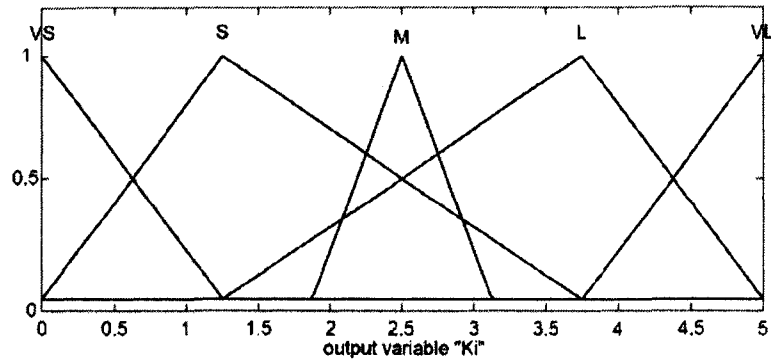


**Fig. 6.12: Membership functions for  $K_i$  of the active and reactive power controllers.**

The proposed fuzzy PI gain scheduler generates suitable changes of the PI controller gains, using center of area method for defuzzification of the two output linguistic variables after applying the 9 fuzzy rules. As a result, these two gains are updated as shown in Figs. 6.13 and 6.14. It is to be noted that  $K_i$ , and  $K_p$  are limited when the steady-state is reached and initialized when the speed command change occurs.

**Table 6.2: Fuzzy rules for the proposed PI gain scheduler.**

$e$	$K_p$	$K_i$
NL	VL	VS
NB	L	S
NM	M	M
NS	S	L
Z	VS	VL
PS	S	L
PM	M	M
PB	L	S
PL	VL	VS

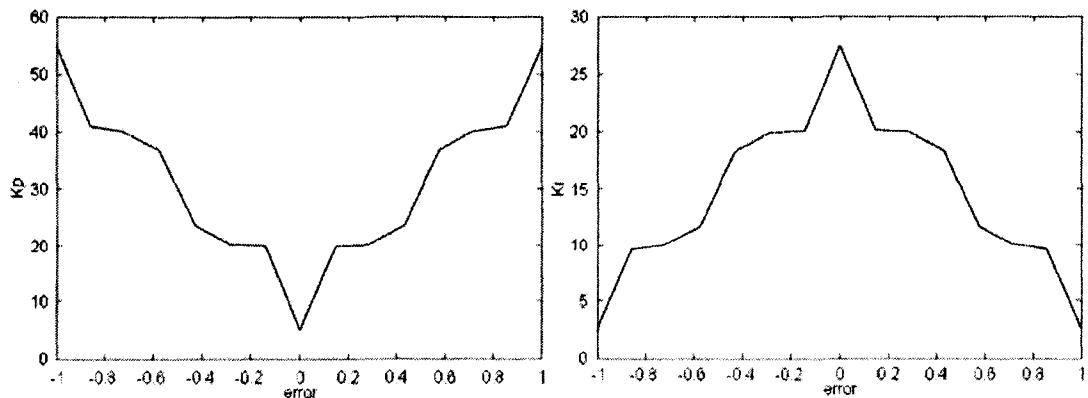


**Fig. 6.13: Proportional and Integral gains vs. error for the speed controller.**

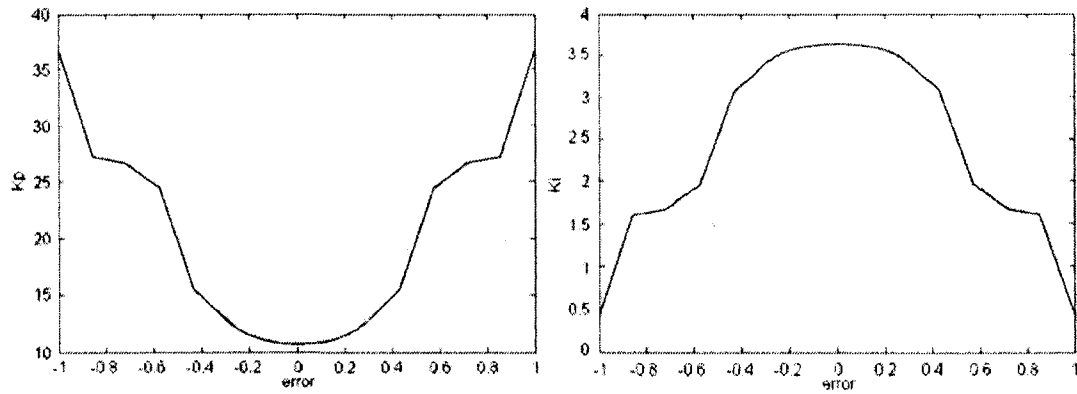


**Fig. 6.14: Proportional and integral gains vs. error for the active and reactive power controllers.**

### 6.4.1 System configuration

The system considered is a grid connected doubly-fed induction generator with the rotor circuit connected to the grid through back-to-back PWM voltage source converters in a configuration shown in Fig. 5.3. The wind turbine considered has a power rating of 40kW. The turbine output power changes as a function of the wind speed as shown in Fig. 5.4. The wind speed is measured in order to determine the set values for both the maximum output power and the corresponding generator speed in order to track the maximum power curve as shown in the maximum power point tracking component in Fig. 6.15. These set values are then used to calculate the error signals which are the set values minus its corresponding measured actual values. The values of the error signals are used as inputs to the fuzzy inference which, depending on the membership functions and the fuzzy rules, determines both the proportional and integral gains for the PI controller part. This takes place in the fuzzy PI gain scheduler component as shown in Fig. 6.15. The output of this block is the scheduled proportional and integral gains  $K_p$  and  $K_i$  for each of the speed, active and reactive power controllers. These gains are the inputs for the PI controller part of the vector controller.

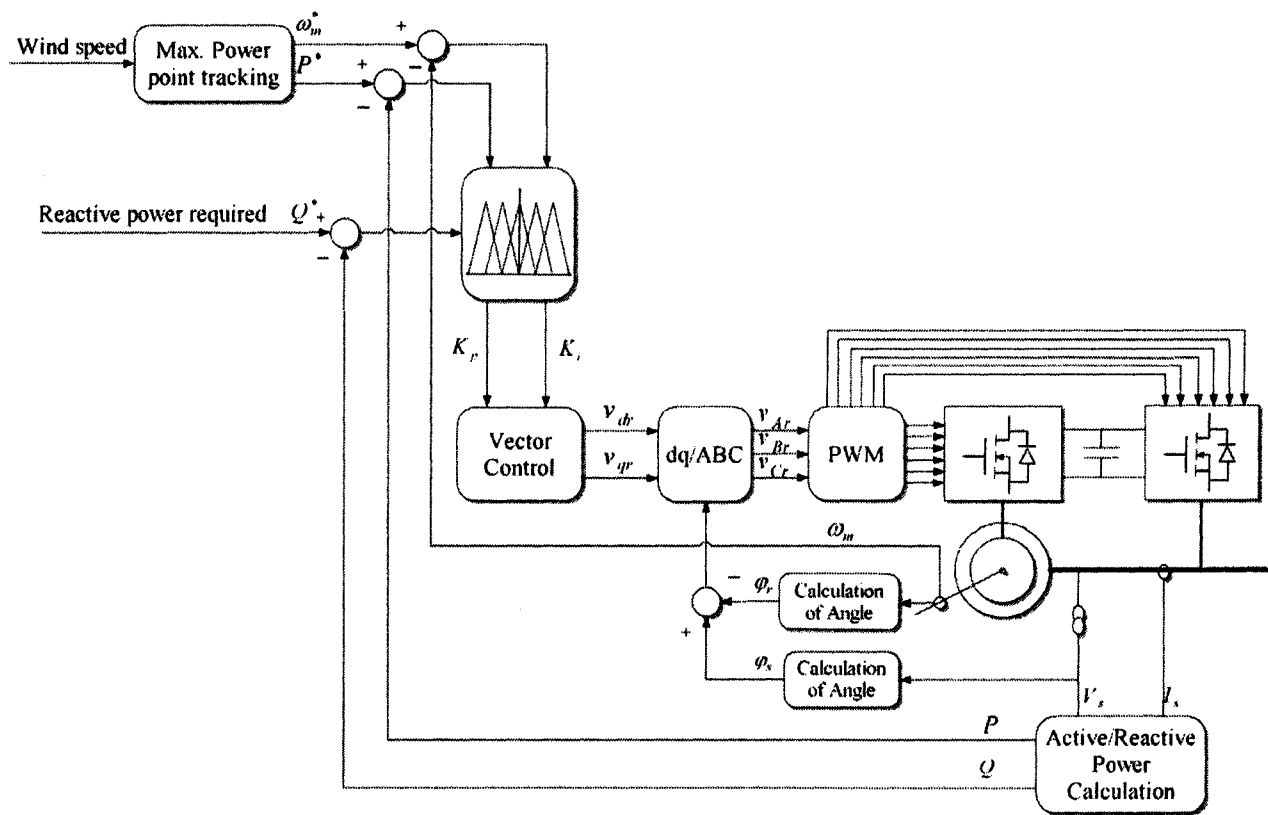


Fig. 6.15: Vector control configuration using the proposed Fuzzy PI gain scheduler.

## 6.5 Simulation and results

Simulation has been performed on a saturated doubly-fed wind driven induction generator system incorporating the proposed fuzzy PI gain scheduler for the vector controller. The induction machine parameters used in the simulation are listed in Table 5.1. The performance of the vector controller with the proposed fuzzy PI gain scheduler is compared to a vector controller employing conventional PI controller with three different configurations of constant proportional and integral gains for speed control and active and reactive power control. The fixed proportional and integral gains of the three different conventional PI controllers considered for comparison are shown in Table 6.3. These values were chosen to be at the least, mid, and the most value of the gain ranges set for the fuzzy PI gains. In Fig. 6.16, the wind speed is 6 m/s which corresponds to a set speed of 994 rpm, i.e. 0.552 pu, according to Fig. 5.4 for the maximum power generation. At  $t = 2s$  the wind speed changed to 8 m/s, so the generator set speed is changed to 1460 rpm to track the maximum power point curve. It can be seen from Fig. 6.16 that by using the proposed fuzzy PI gain scheduler, faster dynamic response, less overshoot, less settling time and less steady-state error are achieved. The performance of the vector controller is further investigated by calculating the stator active and reactive power, rotor d- and q-axis currents, as well as the rotor active and reactive power flow as shown in Figs. 6.17-6.22.

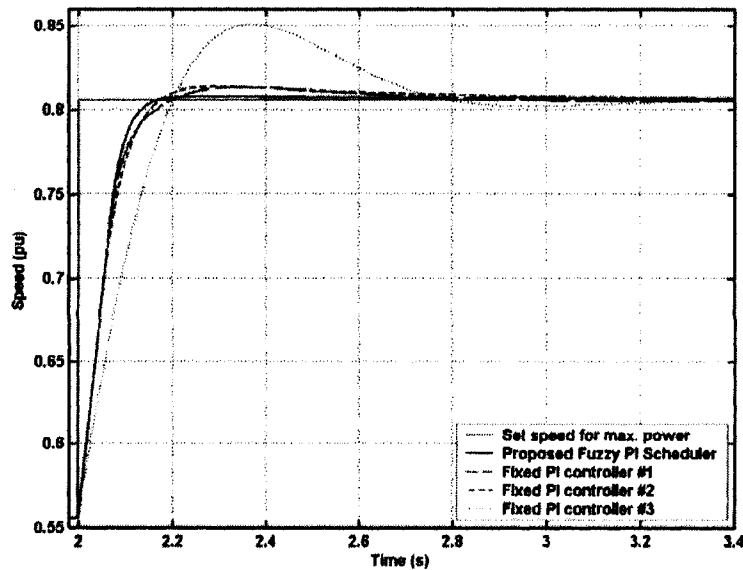


Fig. 6.16: Speed response for sub-synchronous operation.

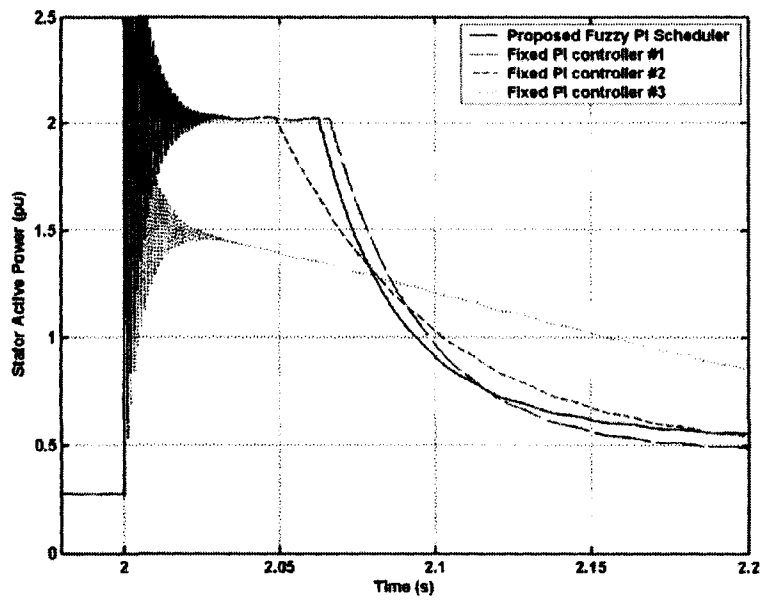


Fig. 6.17: Stator active power for sub-synchronous operation.

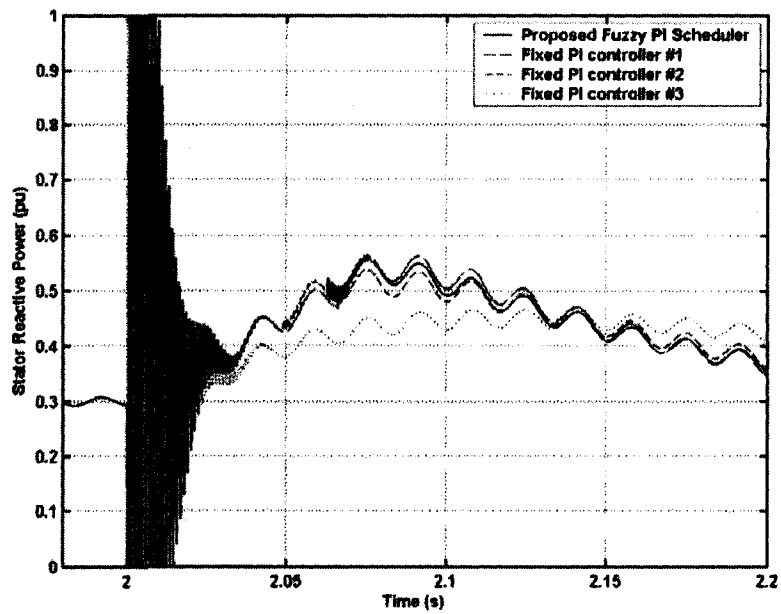


Fig. 6.18: Stator reactive power for sub-synchronous operation.



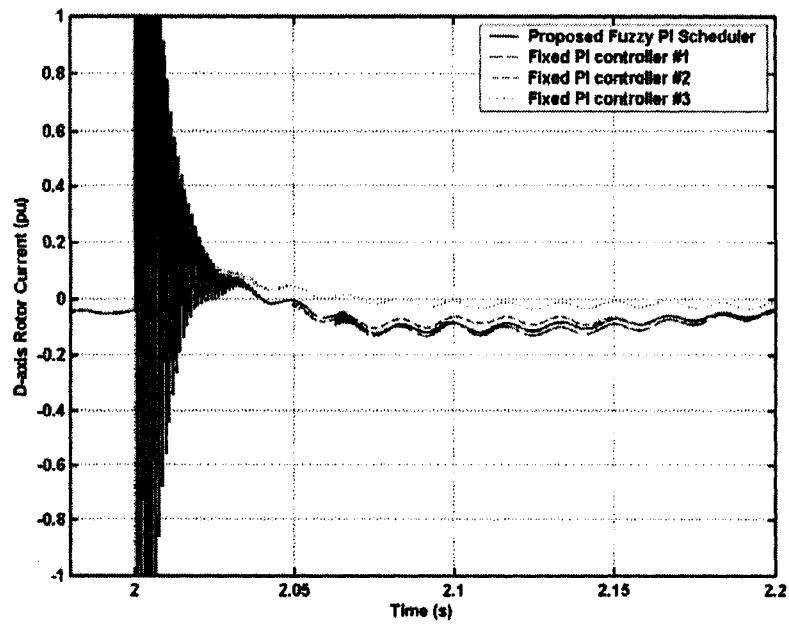


Fig. 6.19: D-axis rotor current for sub-synchronous operation.

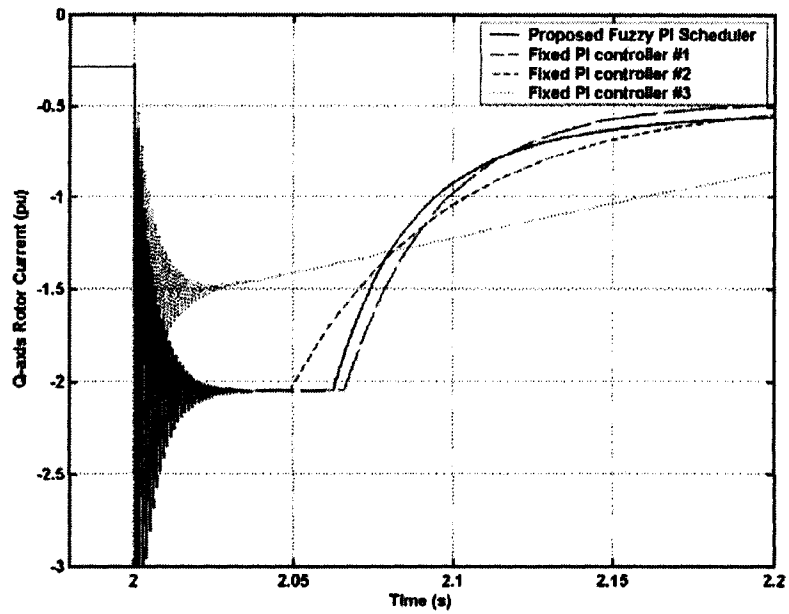


Fig. 6.20: Q-axis rotor current for sub-synchronous operation.

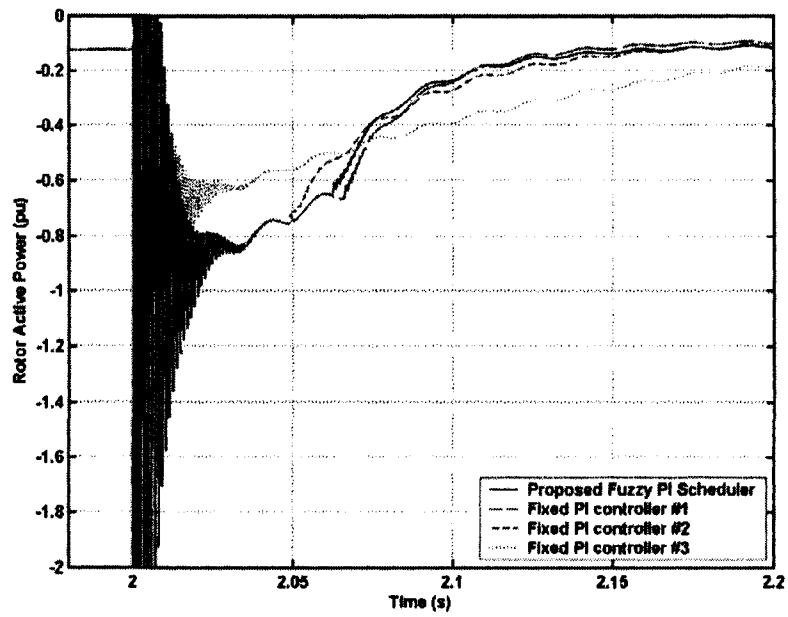


Fig. 6.21: Rotor active power for sub-synchronous operation.

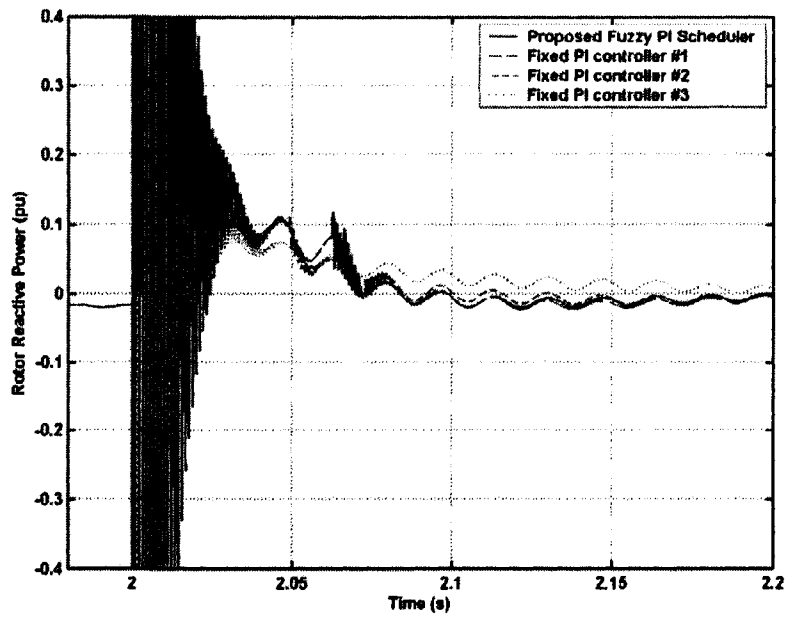


Fig. 6.22: Rotor reactive power for sub-synchronous operation.

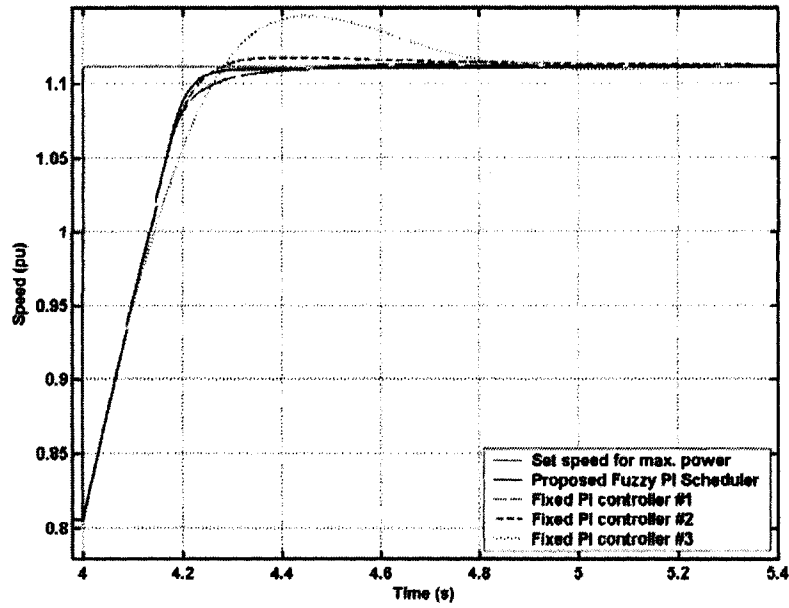


Fig. 6.23: Speed response for super-synchronous operation.

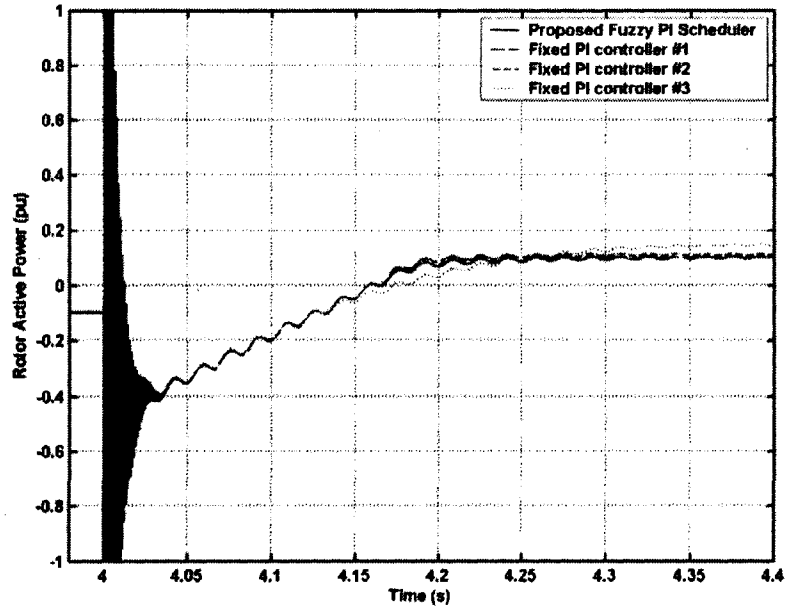


Fig. 6.24: Rotor active power for super-synchronous operation.

For the same scenario considered for the speed response, Figs. 6.17 and 6.18 show the stator active and reactive power generated for  $Q_{set} = 0.3$  pu and  $P_{set} = 0.365$  pu which correspond to the maximum power at wind speed of 6 m/s. At  $t = 2$  s., the wind speed increases to 8 m/s, so the rotor speed increases to 1460 rpm and  $P_{set} = 0.61$  pu to maximize the output power. Figs. 6.19 and 6.20 show the rotor d- and q-axis current components  $i_{dr}$  and  $i_{qr}$  respectively for the same scenario discussed above. It can be seen

that to increase the amount of active power generated, an increase in the q-axis component of the rotor current  $i_{qr}$  is required, on the other hand, there is no change in the d-axis component of the rotor current  $i_{dr}$  because there is no change in the set value of the reactive power generation. Figs. 6.21 and 6.22 show the active and reactive power flow to the rotor for the same operating conditions, i.e. fixed reactive power generation at 0.3 pu and the increase in the active power generated to track the maximum wind energy. It can be seen that the flow of both active and reactive power is toward the rotor as they are both negative. This is due to the fact that the generator is operating at a sub-synchronous speed.

**Table 6.3: Fixed controllers' gains.**

Controller #1				Controller #2				Controller #3			
Speed		Power		Speed		Power		Speed		Power	
$K_p$	$K_i$	$K_p$	$K_i$	$K_p$	$K_i$	$K_p$	$K_i$	$K_p$	$K_i$	$K_p$	$K_i$
50	5	35	0.5	25	15	25	2	10	25	15	3.5

Another case is considered, in which the wind speed is 8 m/s and the generator was working at set speed of 0.81 pu for maximum power generation. At  $t = 4$ s, the wind speed is increased to 12 m/s which requires a set speed of 2010 rpm in order to capture the maximum wind energy as shown in Fig. 6.23. This speed is obviously higher than the synchronous speed and the generator is working in the super-synchronous region. Fig. 6.24 shows the rotor active power flow which in this case is flowing out of the rotor, i.e. more power is generated.

## 6.6 References

- [1] D. Van De Ville, M. Nachtegaal, D. Van der Weken, E. E. Kerre, W. Philips, and I. Lemahieu, "Noise reduction by fuzzy image filtering," *IEEE Transactions on Fuzzy Systems*, vol. 11, pp.429-436, 2003.
- [2] A. W. C. Liew, S. H. Leung, and W. H. Lau, "Fuzzy image clustering incorporating spatial continuity," *IEE Proceedings on Vision, Image and Signal Processing*, vol. 147, pp.185-192, 2000.
- [3] H. Monsef, A. M. Ranjbar, and S. Jadid, "Fuzzy rule-based expert system for power system fault diagnosis," *IEE Proceedings on Generation, Transmission and Distribution*, vol. 144, pp.186-192, 1997.

- [4] A. Ferrero, S. Sangiovanni, and E. Zappitelli, "A fuzzy-set approach to fault-type identification in digital relaying," *IEEE Transactions on Power Delivery*, vol.10, pp.169-175, 1995.
- [5] P. Vas, A. F. Stronach, and M. Neuroth, "Full fuzzy control of a DSP-based high performance induction motor drive," *IEE Proceedings on Control Theory Appl.*, vol. 144, pp. 361-368, 1997.
- [6] B. N. Singh, B. Singh, and B. P. Singh, "Fuzzy control of integrated current-controlled converter-inverter-fed cage induction motor drive," *IEEE Transactions on Industry Applications*, vol. 35, pp.405-412, 1999.
- [7] P. Grabowski, M. Kazmierkowski, B. Bose, and F. Blaabjerg, "A simple direct-torque neuro-fuzzy control of PWM-inverter-fed induction motor drive," *IEEE Transactions on Industrial Electronics*, vol. 47, pp. 863-870, 2000.
- [8] F. Zidani, M. E. H. Benbouzid, D. Diallo, and M. S. Nait-Said, "Induction motor stator faults diagnosis by a current Concordia pattern-based fuzzy decision system," *IEEE Transactions on Energy Conversion*, vol.18, pp.469-475, 2003.
- [9] R. M. Hilloowala, and A. M. Sharaf, "A rule-based fuzzy logic controller for a PWM inverter in a stand alone wind energy conversion scheme," *IEEE Transactions on Industry Applications*, vol. 32, pp. 57-65, 1996.
- [10] H. M. Mashaly, A. M. Sharaf, A. A. El-Sattar, and M. M. Mansour, "Implementation of a fuzzy logic controller for wind energy induction generator DC link scheme," *Proceedings of the Third IEEE Conference on Fuzzy Systems 1994*, vol. 2, pp. 978-982, 1994.
- [11] M. G. Simoes, B. K. Bose, and R. J. Spiegel, "Fuzzy logic based intelligent control of a variable speed cage machine wind generation system," *IEEE Transactions on Power Electronics*, vol. 12, pp. 87-95, 1997.
- [12] M. G. Simoes, B. K. Bose, and R. J. Spiegel, "Design and performance evaluation of a fuzzy-logic-based variable-speed wind generation system," *IEEE Transactions on Industry Applications*, vol. 33 , pp. 956-965, 1997.
- [13] Z. Chen, S. A. Gomez, and M. McCormick, "A fuzzy logic controlled power electronic system for variable speed wind energy conversion systems," *Eighth*

- International Conference on Power Electronics and Variable Speed Drives*, pp. 114-119, 2000.
- [14] M. M. Prats, J. M. Carrasco, E. Galvan, J. A. Sanchez, and L. G. Franquelo, "A new fuzzy logic controller to improve the captured wind energy in a real 800 kW variable speed-variable pitch wind turbine," *IEEE 33rd Annual Power Electronics Specialists Conference*, vol.1, pp. 101- 105, 2002.
  - [15] E. H. Mamdani and S. Assilian, "An experiment in linguistic synthesis with a fuzzy logic controller," *International Journal of Man-Machine Studies*, vol. 7, no. 1, pp. 1-13, 1975.
  - [16] L. A. Zadeh, "Outline of a new approach to the analysis of complex systems and decision processes," *IEEE Transactions on Systems, Man, and Cybernetics*, vol. 3, no. 1, pp. 28-44, Jan. 1973.
  - [17] Matlab Fuzzy toolbox
  - [18] A. S. Mostafa, A. L. Mohamadein, and E. M. Rashad, "Analysis of series-connected wound-rotor self-excited induction generator," *IEE Proceedings on Electric Power Applications*, vol. 140, pp. 329-336, 1993.
  - [19] J. Teeter, M. Chow, and J. J. Brickley, "Use of a fuzzy gain tuner for improved control of a DC motor system with nonlinearities," *Proceedings of the IEEE International Conference on Industrial Technology*, pp. 258-262, 1994.
  - [20] S. He, S. Tan, F. Xu and P. Wang, "Fuzzy self-tuning of PID controllers," *Fuzzy Sets and Systems*, vol. 56, pp. 37-46, 1993.
  - [21] K. G. Shin and X. Cui. "Design of a knowledge-based controller for intelligent control systems." *IEEE Transactions on Systems, Man. and Cybernetics*, vol. 21, pp. 368-375, 1991.
  - [22] J. Lee, "On methods for improving performance of PI type fuzzy logic controllers," *IEEE Transactions on Fuzzy Systems*, vol. 1, pp. 298-301, 1993.
  - [23] B. Kosko, *Neural Networks and Fuzzy Systems*, Prentice-Hall, Englewood Cliffs, New Jersey, 1992.
  - [24] J. Victor, and A. Douarda, "Adaptive scaling factors algorithm for the fuzzy logic controller," *Simulation Practice and Theory*, pp. 121-136, Elsevier Science, 1995.

- [25] H. C. Tseng, and V. H. Hwang, "Servocontroller tuning with fuzzy logic," *IEEE Transactions on Control Systems Technology*, vol. 1, pp. 262-269, 1993.
- [26] S. Tzafestas, and N. P. Papanikolopoulos, "Incremental fuzzy expert PID control," *IEEE Trans. on Industrial Electronics*, vol. 37, pp.365-371, 1990.
- [27] Z. Y. Zhang, M. Tomizuka, and S. Isaka, "Fuzzy gain scheduling of PID controllers," *IEEE Trans. on Systems, Man, and Cybernetics*, vol. 23, pp. 1392-1398, 1993.
- [28] L. Romeral, J. Llmuet, E. Aldabas, and A. Arias, "A simple fuzzy adaptive speed controller," *Proc. of IEEE Annual Meeting Industry Applications Conf.*, vol. 2, pp. 1249-1256, 2000.

## **7 Neuro-fuzzy Control System**

### **7.1 Introduction**

The design and choice of the membership parameters (number, shape and location) require an extensive knowledge and experience of the control system designer. It also requires the existence of a detailed mathematical model of the system which is not always available. In such cases, a set of input/output data can be obtained. In the neuro-fuzzy system, a learning method similar to that of neural networks is used to train and adjust the parameters of the membership functions. Neuro-adaptive learning techniques provide a method for the fuzzy modeling procedure to learn information about a data set. Then, the parameters of membership functions that best allow the associated fuzzy inference system to track the given input/output data are computed.

Currently, several neuro-fuzzy networks exist in the literature. Most notable are Adaptive Network-based Fuzzy Inference System (ANFIS) developed by Jang [1]. Most neuro-fuzzy systems are developed based on the concept of neural methods on fuzzy systems. The idea is to learn the shape of membership functions for the fuzzy system efficiently by taking the advantage of adaptive property of the neural methods. Takagi, Sugeno and Kang [2,3] are known as the first to utilize this approach. Later, Jang [1] elaborated upon this idea and developed a systematic approach for the adaptation with illustrations of several successful applications.

There are two types of fuzzy systems namely Mamdani and Sugeno. The one that is commonly used is the Mamdani type which uses linguistic expressions to describe the membership functions. The Sugeno type has some advantages over the Mamdani type such as its computational efficiency, suitable for the application of optimization and adaptive techniques and has guaranteed continuity of the output surface.

#### **7.1.1 Mamdani fuzzy model**

The Mamdani fuzzy inference system [4] was proposed as the first attempt to control a steam engine and boiler combination by a set of linguistic control rules obtained from experienced human operators. Figure 7.1 is an illustration of how a two-rule



Mamdani fuzzy inference system derives the overall output  $z$  when subjected to two crisp inputs as  $x$  and  $y$ .

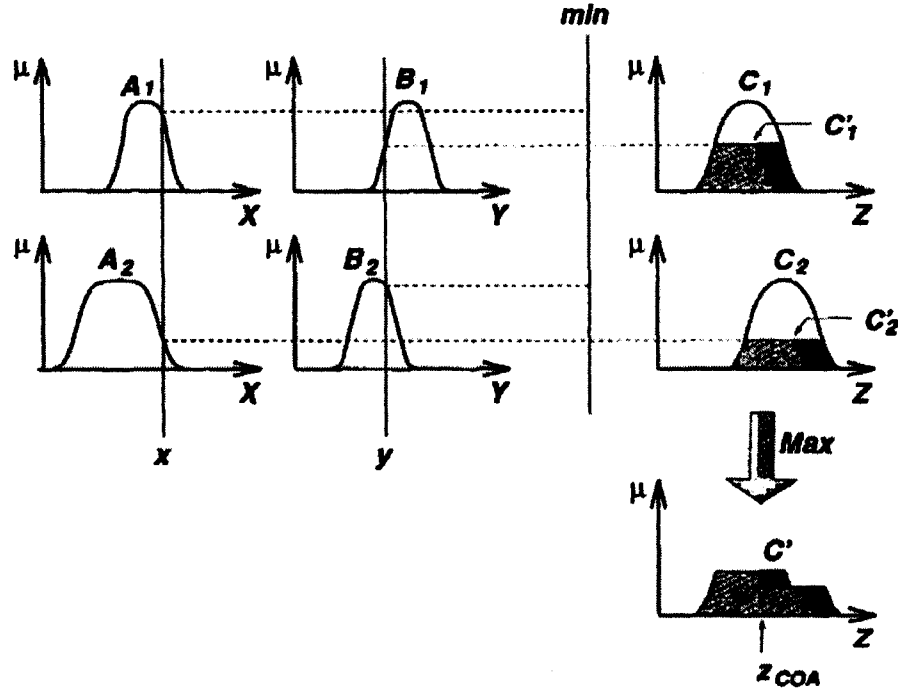


Fig. 7.1: The Mamdani fuzzy inference system using min and max for T-norm and T-conorm operators respectively.

### 7.1.2 Sugeno fuzzy model

The Sugeno fuzzy model was proposed by Takagi, Sugeno, and Kang [5, 6] in an effort to develop a systematic approach to generating fuzzy rules from a given input-output data set. A typical fuzzy rule in a Sugeno fuzzy model has the form

**if  $x$  is  $A$  and  $y$  is  $B$  then  $z = f(x, y)$ ,**

where  $A$  and  $B$  are fuzzy sets in the antecedent, while  $z = f(x, y)$  is a crisp function in the consequent. Usually  $f(x, y)$  is a polynomial in the input variables  $x$  and  $y$ , but it can be any function as long as it can appropriately describe the output of the model within the fuzzy region specified by the antecedent of the rule. When  $f(x, y)$  is a first-order polynomial, the resulting fuzzy inference system is called a first-order Sugeno fuzzy model, which was originally proposed in [5, 6].

When  $f$  is a constant, we then have a zero-order Sugeno fuzzy model, which can be viewed either as a special case of the Mamdani fuzzy inference system, in which each

rule's consequent is specified by a fuzzy singleton (or a pre-defuzzified consequent). Moreover, a zero-order Sugeno fuzzy model is functionally equivalent to a radial basis function network under certain minor constraints [7].

The output of a zero-order Sugeno model is a smooth function of its input variables as long as the neighboring MFs in the antecedent have enough overlap. In other words, the overlap of MFs in the consequent of a Mamdani model does not have a decisive effect on the smoothness; it is the overlap of the antecedent MFs that determines the smoothness of the resulting input-output behavior.

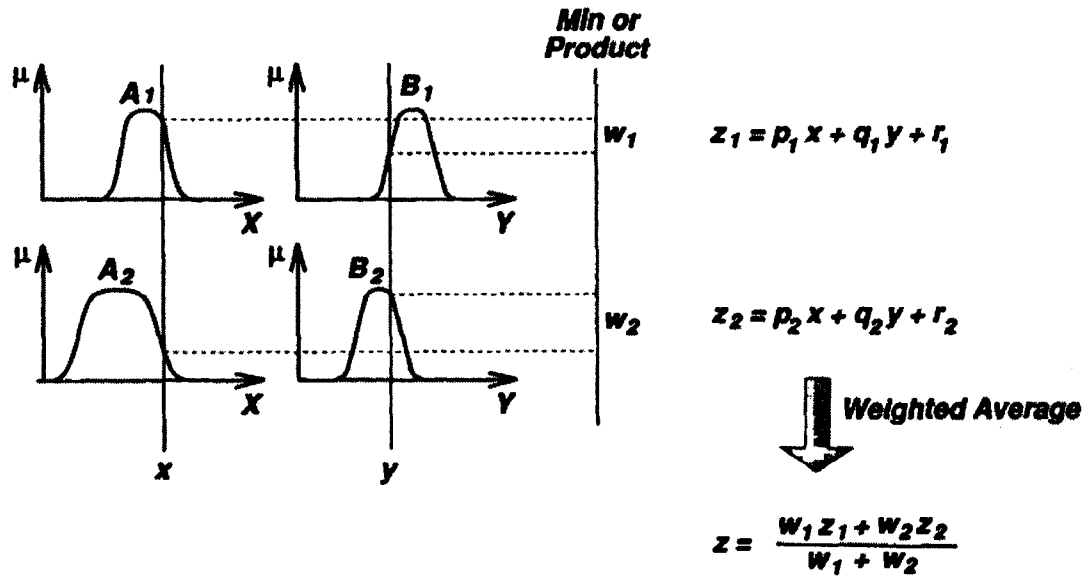


Fig. 7.2: The Sugeno fuzzy model.

Figure 7.2 shows the fuzzy reasoning procedure for a first-order Sugeno fuzzy model. Since each rule has a crisp output, the overall output is obtained via weighted average, thus avoiding the time-consuming process of defuzzification required in a Mamdani model. In practice, the weighted average operator is sometimes replaced with the weighted sum operator (that is,  $z = \omega_1 z_1 + \omega_2 z_2$  in Fig.7.2) to reduce computation further, especially in the training of a fuzzy inference system. However, this simplification could lead to the loss of MF linguistic meanings unless the sum of firing strengths (that is,  $\sum_i \omega_i$ ) is close to unity. Since the only fuzzy part of a Sugeno model is in its antecedent, it is easy to demonstrate the distinction between a set of fuzzy rules and non-fuzzy ones.

## 7.2 ANFIS Architecture

For simplicity, we assume that the fuzzy inference system under consideration has two inputs  $x$  and  $y$  and one output  $z$ . For a first-order Sugeno fuzzy model [5, 6, 8], a common rule set with two fuzzy if-then rules is the following:

Rule 1: If  $x$  is  $A_1$  and  $y$  is  $B_1$ , then  $f_1 = p_1x + q_1y + r_1$ ,

Rule 2: If  $x$  is  $A_2$  and  $y$  is  $B_2$ , then  $f_2 = p_2x + q_2y + r_2$ .

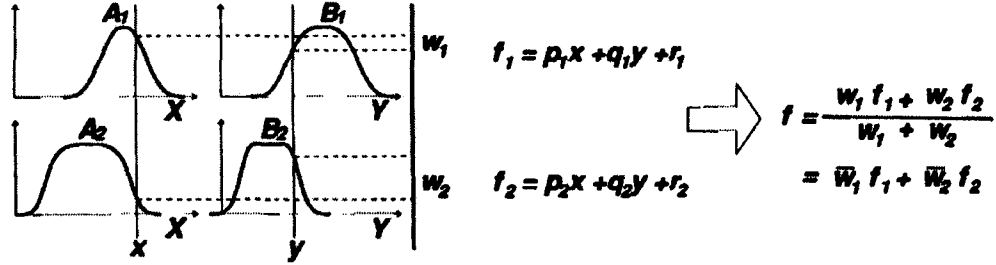


Fig. 7.3: A two input first-order Sugeno fuzzy model with two rules.

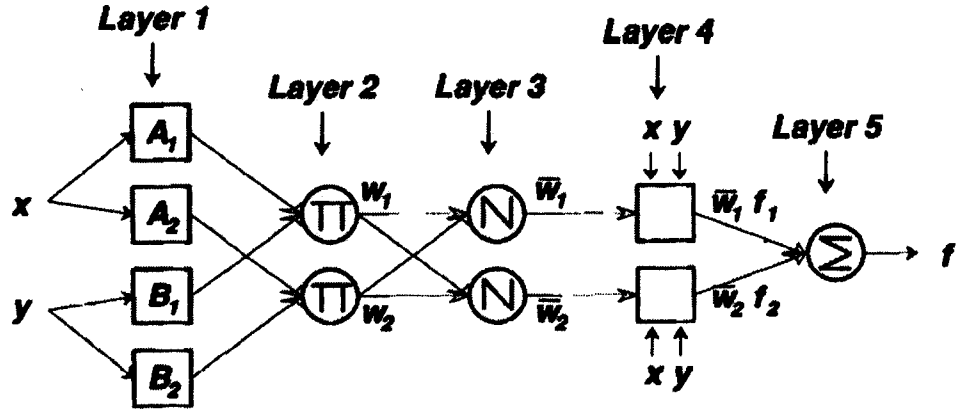


Fig. 7.4: Equivalent ANFIS architecture.

Figure 7.3 illustrates the reasoning mechanism for this Sugeno model; the corresponding equivalent ANFIS architecture is as shown in Fig.7.4, where nodes of the same layer have similar functions, as described next. (Here we denote the output of the  $i^{\text{th}}$  node in layer  $l$  as  $O_{l,i}$ .)

**Layer 1** Every node  $i$  in this layer is an adaptive node with a node function

$$O_{1,i} = \mu_{A_i}(x), \quad \text{for } i=1, 2, \text{ or}$$

$$O_{1,i} = \mu_{B_{i-2}}(y), \quad \text{for } i=3, 4, \quad (7.1)$$

where  $x$  (or  $y$ ) is the input to node  $i$  and  $A_i$  (or  $B_{i-2}$ ) is a linguistic label (such as "small" or "large") associated with this node. In other words,  $O_{1,i}$  is the membership grade of a fuzzy set  $A$  ( $= A_1, A_2, B_1$  or  $B_2$ ) and it specifies the degree to which the given input  $x$  (or  $y$ ) satisfies the quantifier  $A$ . Here the membership function for  $A$  can be any appropriate parameterized membership function introduced earlier, such as the generalized bell function:

$$\mu_A(x) = \frac{1}{1 + \left| \frac{x - c_i}{a_i} \right|^{2b}} \quad (7.2)$$

where  $\{a_i, b_i, c_i\}$  is the parameter set. As the values of these parameters change, the bell-shaped function varies accordingly, thus exhibiting various forms of membership functions for fuzzy set  $A$ . Parameters in this layer are referred to as premise parameters.

**Layer 2** Every node in this layer is a fixed node labeled  $\Pi$ , whose output is the product of all the incoming signals:

$$O_{2,i} = \omega_i = \mu_{A_i}(x) \mu_{B_i}(y), i=1, 2. \quad (7.3)$$

Each node output represents the firing strength of a rule. In general, any operator that performs fuzzy AND can be used as the node function in this layer.

**Layer 3** Every node in this layer is a fixed node labeled  $N$ . The  $i^{\text{th}}$  node calculates the ratio of the  $i^{\text{th}}$  rule's firing strength to the sum of all rules' firing strengths:

$$O_{3,i} = \varpi_i = \frac{\omega_i}{\omega_1 + \omega_2}, i=1, 2. \quad (7.4)$$

For convenience, outputs of this layer are called normalized firing strengths.

**Layer 4** Every node  $i$  in this layer is an adaptive node with a node function

$$O_{4,i} = \varpi_i f_i = \varpi_i (p_i x + q_i y + r_i) \quad (7.5)$$

where  $\overline{\omega_i}$  is a normalized firing strength from layer 3 and  $\{p_i, q_i, r_i\}$  is the parameter set of this node. Parameters in this layer are referred to as consequent parameters.

**Layer 5** The single node in this layer is a fixed node labeled  $\Sigma$ , which computes the overall output as the summation of all incoming signals:

$$\text{Overall output} = O_{5,1} = \sum_i \varpi_i f_i = \frac{\sum_i \omega_i f_i}{\sum_i \omega_i} \quad (7.6)$$

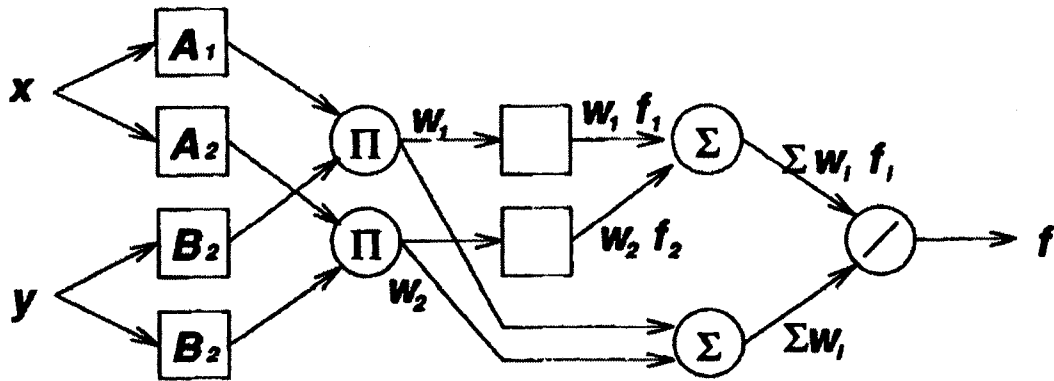


Fig. 7.5: ANFIS architecture for the Sugeno fuzzy model, where weight normalization is performed at the very last layer.

Thus we have constructed an adaptive network that is functionally equivalent to a Sugeno fuzzy model. Note that the structure of this adaptive network is not unique; we can combine layers 3 and 4 to obtain an equivalent network with only four layers. By the same token, we can perform the weight normalization at the last layer; Fig.7.5 illustrates an ANFIS of this type. In the extreme case, we can even shrink the whole network into a single adaptive node with the same parameter set. Obviously, the assignment of node functions and the network configuration are arbitrary, as long as each node and each layer perform meaningful and modular functionalities.

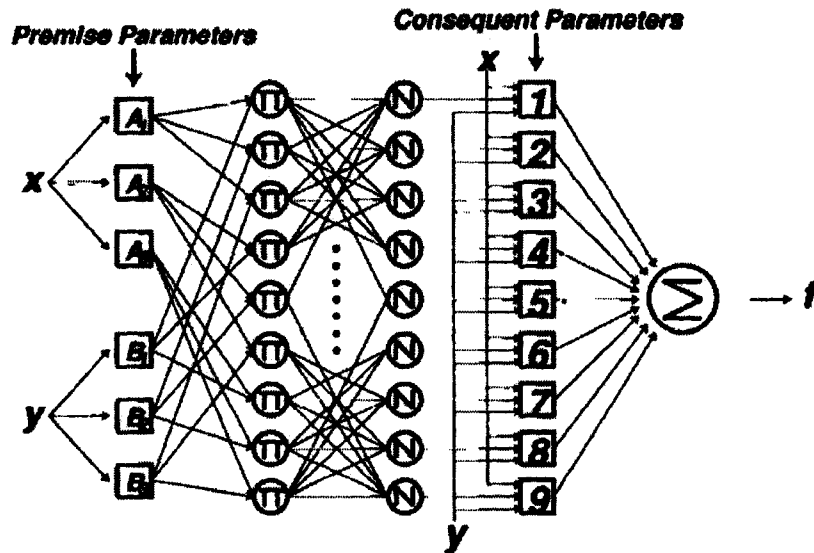


Fig: 7.6: ANFIS architecture for a two-input Sugeno fuzzy model with nine rules.

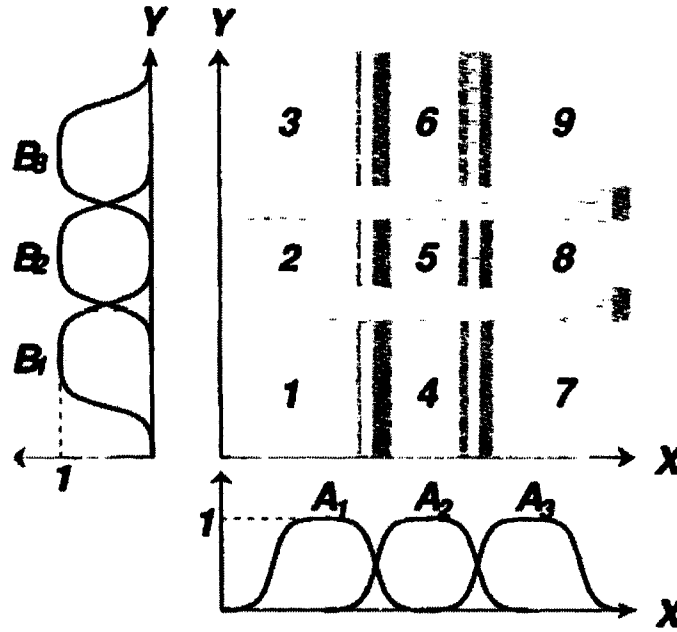


Fig. 7.7: The input space that are partitioned into nine fuzzy regions.

Throughout this chapter, we shall concentrate on the ANFIS architectures for the first-order Sugeno fuzzy model because of its transparency and efficiency. Figure 7.6 is an ANFIS architecture that is equivalent to a two-input first-order Sugeno fuzzy model with nine rules, where each input is assumed to have three associated MFs. Figure 7.7 illustrates how the two-dimensional input space is partitioned into nine overlapping fuzzy regions, each of which is governed by a fuzzy if-then rule. In other words, the premise part of a rule defines a fuzzy region, while the consequent part specifies the output within the region.

### 7.3 Hybrid learning algorithm

From the ANFIS architecture shown in Fig.7.4, we observe that when the values of the premise parameters are fixed, the overall output can be expressed as a linear combination of the consequent parameters. In symbols, the output  $f$  in Fig.7.4 can be rewritten as

$$\begin{aligned}
 f &= \frac{\omega_1}{\omega_1 + \omega_2} f_1 + \frac{\omega_2}{\omega_1 + \omega_2} f_2 \\
 &= \varpi_1(p_1x + q_1y + r_1) + \varpi_2(p_2x + q_2y + r_2) \\
 &= (\varpi_1x)p_1 + (\varpi_1y)q_1 + (\varpi_1)r_1 + (\varpi_2x)p_2 + (\varpi_2y)q_2 + (\varpi_2)r_2
 \end{aligned} \tag{7.7}$$

which is linear in the consequent parameters  $p_1, q_1, r_1, p_2, q_2, \text{ and } r_2$ . From this observation, we have

$S$  = set of total parameters,

$S_1$  = set of premise (nonlinear) parameters,

$S_2$  = set of consequent (linear) parameters

Therefore, the hybrid learning algorithm developed in [9] can be applied directly. More specifically, in the forward pass of the hybrid learning algorithm, node outputs go forward until layer 4 and the consequent parameters are identified by the least-squares method. In the backward pass, the error signals propagate backward and the premise parameters are updated by gradient descent. Table 7.1 summarizes the activities in each pass.

**Table 7.1: Two passes in the hybrid learning procedure for ANFIS.**

	Forward pass	Backward pass
Premise parameters	Fixed	Gradient descent
Consequent parameters	Least-squares estimator	Fixed
Signals	Node outputs	Error signals

As mentioned in [9], the consequent parameters thus identified are optimal under the condition that the premise parameters are fixed. Accordingly, the hybrid approach converges much faster since it reduces the search space dimensions of the original pure back-propagation method. Thus we should always look for the possibility of decomposing the parameter set in the first place.

Because the update formulas for the premise and consequent parameters are decoupled in the hybrid learning rule (see Table 7.1), further speedup of learning is possible by using variants of the gradient method or other optimization techniques on the premise parameters, such as conjugate gradient descent, second-order back-propagation [10], quick propagation [11], and many others.

#### **7.4 Implementation of neuro-fuzzy gain scheduler**

To apply the vector control to the DFIG system, six neuro-fuzzy gain tuners are trained. Two for each of active power, reactive power and speed controllers. One unit is

responsible for tuning the proportional gain and the other for tuning the integral gain. The developed neuro-fuzzy system is a first-order Sugeno type which has a single input with ten Gaussian distribution membership functions. It has ten if-then rules. A simple structure of the developed neuro-fuzzy system is shown in Fig. 7.8 where the input is the error signal of the controlled variables of speed, active and reactive power ( $\Delta\omega$ ,  $\Delta P$ ,  $\Delta Q$ ). The training is performed using the hybrid back-propagation algorithm. The training is done using a set of input/output data collected from extensive simulations of the vector controller system under different operating conditions using constant PI gains for the active, reactive and speed controllers. The number of training epochs is set to 45 with an error tolerance  $10^{-6}$ . The number of epoch was chosen to be the highest number after which there is no significant reduction in the training error. Figure 7.9 shows the error while training at each epoch for the neuro-fuzzy gain tuner of the speed controller. After the training process, the input membership functions for the neuro-fuzzy proportional gain tuner of both active power and speed are as shown in Fig. 7.10. The output membership functions were chosen to be linear; the parameters of the ten output membership functions for the speed controller and active and reactive power controller are listed in Tables 7.2 and 7.3 respectively. Figure 7.11 shows the neuro-fuzzy gain scheduler in its place with the vector controller and the DFIG.

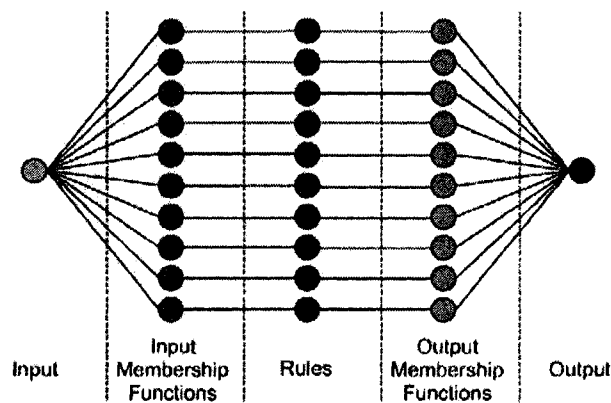


**Fig. 7.8: Simple structure of a single unit of the neuro-fuzzy gain scheduler.**



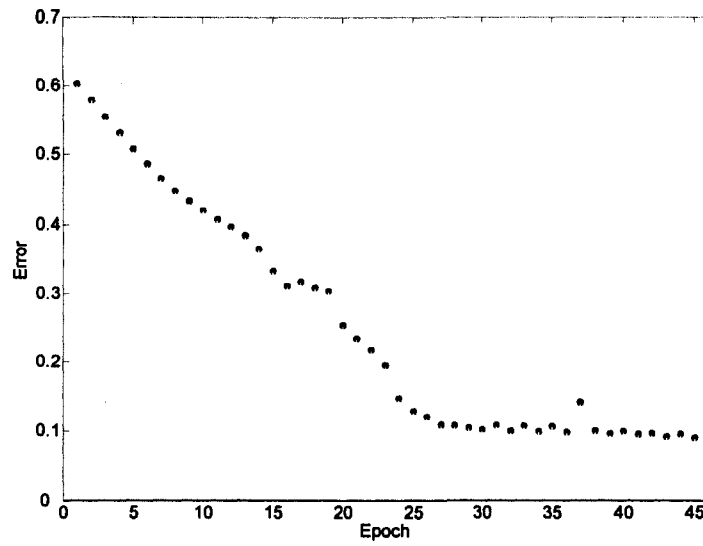
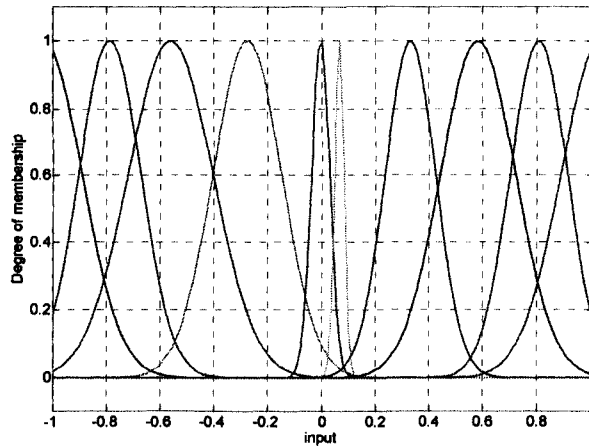
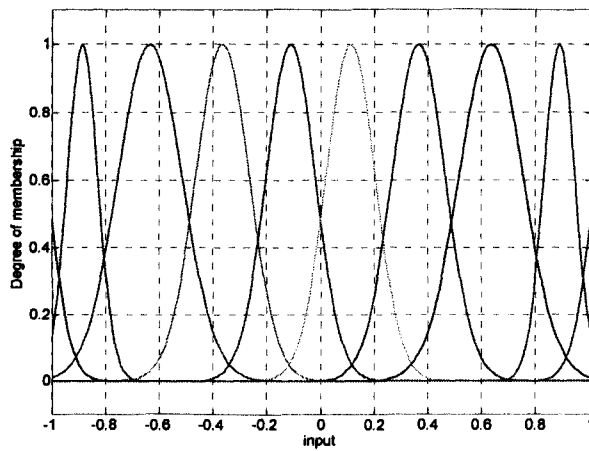


**Fig. 7.9: The training error for the speed neuro-fuzzy gain tuner.**



**(a)**



**(b)**

**Fig. 7.10: Input membership functions for the proportional gain tuners.**

**(a) Active power controller. (b) Speed controller.**

**Table 7.2: Parameters of the Linear Output Membership Functions of the Speed Controller.**

	Proportional Gain		Integral Gain	
	$P_{11}$	$P_{12}$	$P_{21}$	$P_{22}$
MF 1	-387	-339.1	175.9	179.9
MF 2	-203.3	-117.4	52.38	46.06
MF 3	-171.7	-53.78	38.23	32.38
MF 4	-26.53	18.04	-1.405	19.37
MF 5	-197.6	3.579	26.85	23.29
MF 6	-63.12	26.77	-63.06	27.92
MF 7	-0.2717	21.15	-7.523	19.54
MF 8	95.26	-14.91	-72.93	50.47
MF 9	146.9	-65.4	-79.23	70.89
MF 10	373	-323	-190.5	196.1

**Table 7.3: Parameters of the Linear Output Membership Functions of the Active and Reactive Power Controllers.**

	Proportional Gain		Integral Gain	
	$P_{11}$	$P_{12}$	$P_{21}$	$P_{22}$
MF 1	-95.32	-56.11	140.6	142.8
MF 2	-15.95	13.24	16.96	26.35
MF 3	-4.948	22.9	5.534	17.16
MF 4	-2.39	11.85	6.732	29.42
MF 5	-2.023	11.63	3.208	28.5
MF 6	2.023	11.63	-3.208	28.5
MF 7	2.39	11.85	-6.732	29.42
MF 8	4.948	22.9	-5.534	17.16
MF 9	15.95	13.24	-16.96	26.35
MF 10	95.32	-56.11	-140.6	142.8

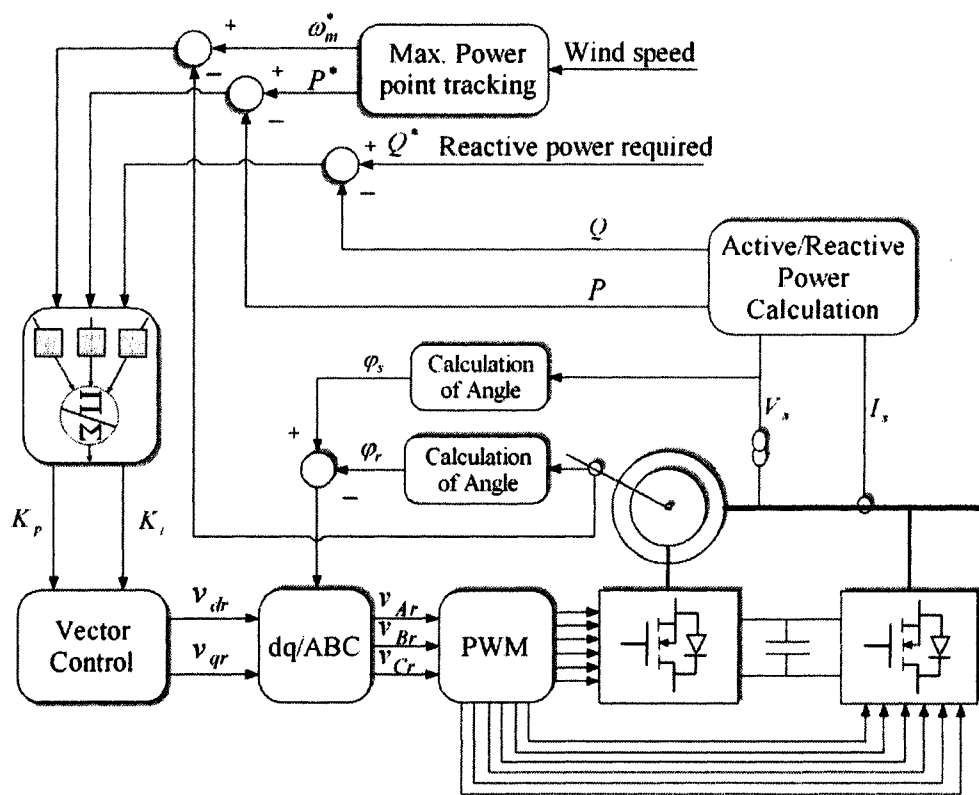


Fig. 7.11: Neuro-fuzzy gain scheduler for vector control of wind driven DFIG.

## 7.5 Simulation and results

The system considered in this chapter is a grid connected wind driven DFIG with the rotor circuit connected to the grid through back-to-back PWM voltage source converters in a configuration shown in Fig. 5.3. The wind turbine considered has a power rating of 40kW. Main and leakage flux saturation was incorporated as discussed in section 3.4 and the DFIG parameters are listed in Table 5.1. The turbine output power changes as a function of the wind speed as well as the generator speed as shown in Fig. 5.4. The wind speed is measured in order to determine the set values for both the maximum output power and the corresponding generator speed in order to track the maximum power curve as shown in the maximum power point tracking component in Fig. 5.4. Although measuring the wind speed may have some drawbacks, it is the most accurate and easiest way to change the generator speed to maximize the power generation. Major wind turbine manufacturers such as Vestas and Nordex use ultrasonic wind sensors in their V90-3.0 MW model [12] and N90/2500 kW model [13], respectively.

While the task of the rotor side converter is to apply the vector control strategy outlined previously, the grid side converter is controlled to maintain a constant voltage level across the coupling capacitor. A transformer is usually used in the rotor circuit due to the different voltage levels between the stator and the rotor. Also, a filter is utilized to minimize the harmonics injected to the grid due to the switching of the power electronic devices.

The performance of the system employing the proposed neuro-fuzzy gain tuner is examined under different operating conditions and compared to that of constant proportional and integral gains. One of these conditions is presented for illustration. In Fig. 7.12, the wind speed is 6 m/s. For the maximum power generation, this corresponds to a set speed of 994 rpm, i.e. 0.552 pu, according to Fig. 5.4. At  $t = 2$ s the wind speed changed to 8 m/s, so the generator set speed is changed to 1460 rpm to track the maximum power point curve. Fig. 7.12 shows that, by using the proposed neuro-fuzzy PI gain scheduler, faster dynamic response, less overshoot, less settling time and less steady-state error are achieved. The performance of the vector-controller is further investigated by calculating the stator active and reactive powers and the rotor d- and q-axis currents.

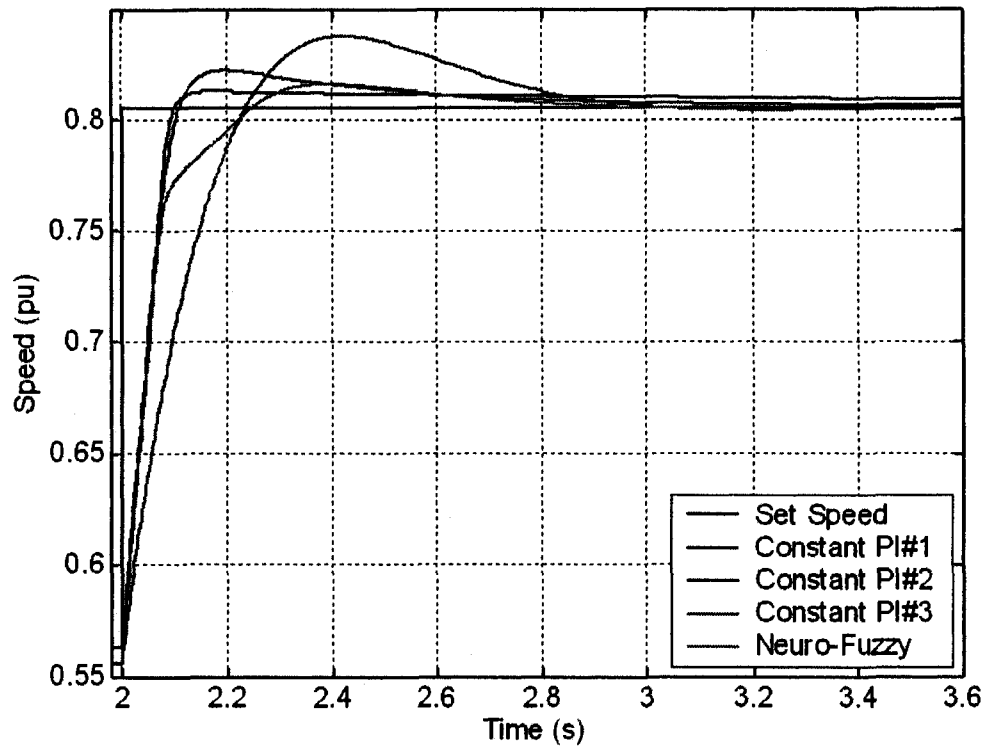
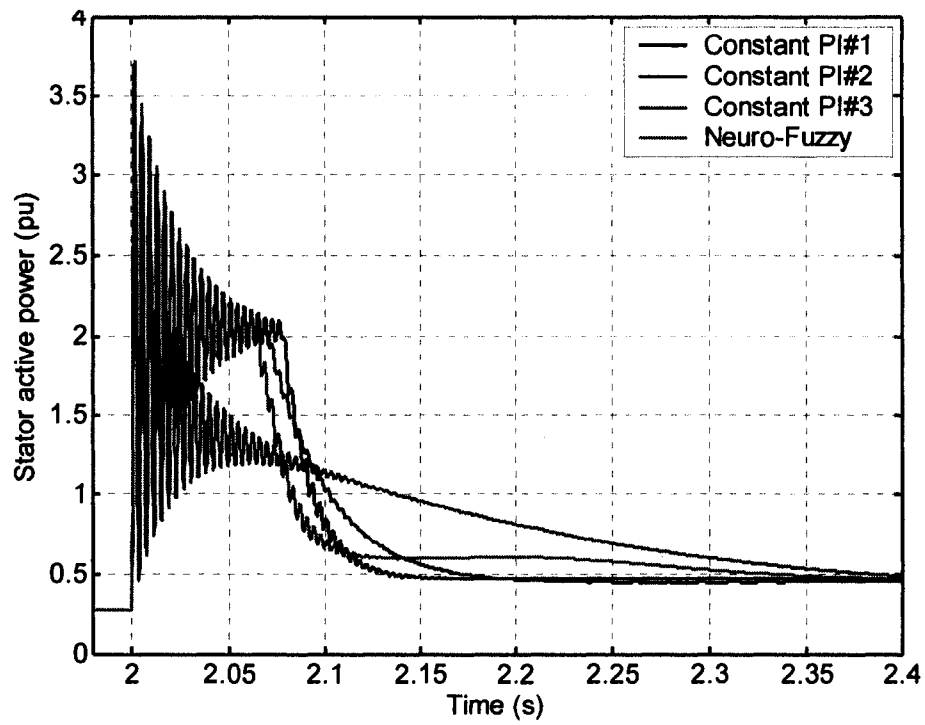
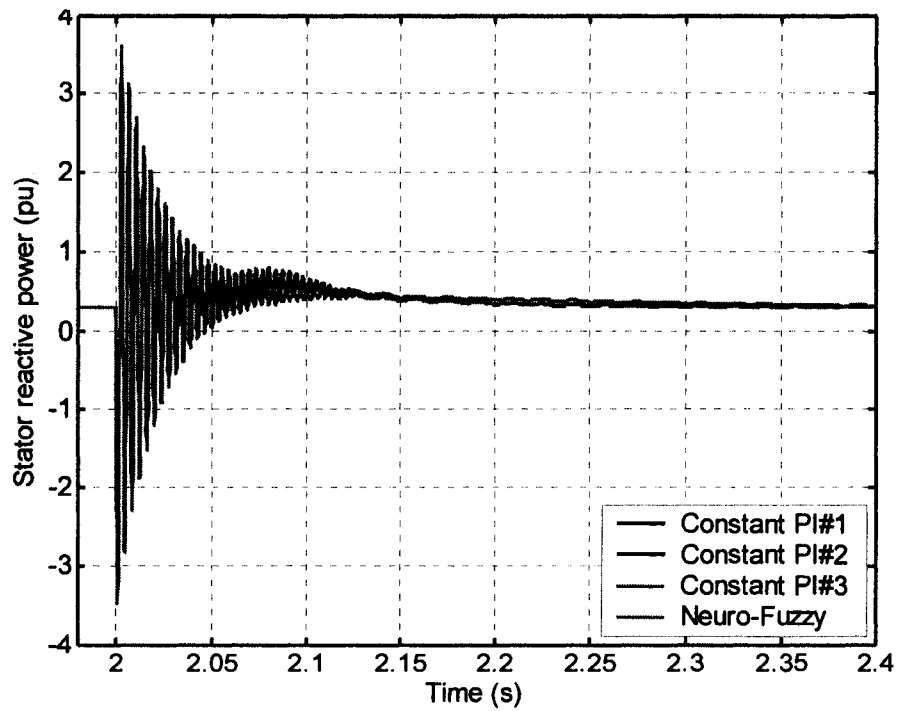


Fig. 7.12: System speed response.

For the same scenario considered for the speed response, Fig. 7.13 shows the stator active and reactive power generated for  $Q_{set} = 0.3$  pu and  $P_{set} = 0.365$  pu, which correspond to the maximum power at a wind speed of 6 m/s. At  $t = 2$ s, the wind speed increases to 8 m/s, so the rotor speed increases to 1460 rpm and  $P_{set} = 0.61$  pu, to maximize the output power. Figure 7.14 shows the rotor d- and q-axis current components,  $i_{dr}$  and  $i_{qr}$  respectively, for the same scenario discussed above. It can be seen that to increase the amount of active power generated, an increase in the q-axis component of the rotor current  $i_{qr}$  is required. Nevertheless, there is no change in the d-axis component of the rotor current  $i_{dr}$  because there is no change in the set value of the reactive power generation.

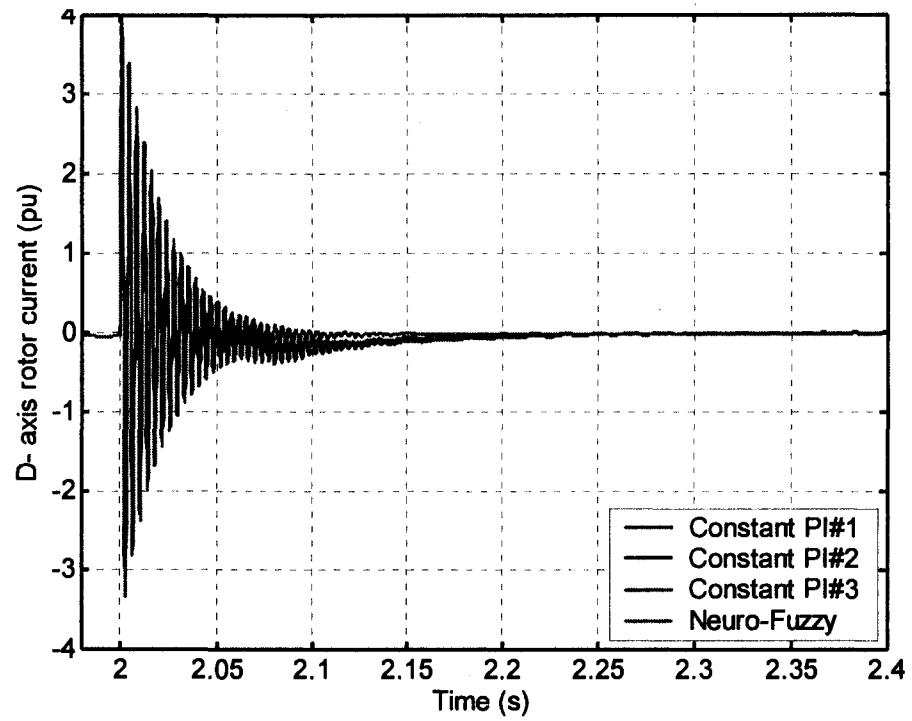


(a)

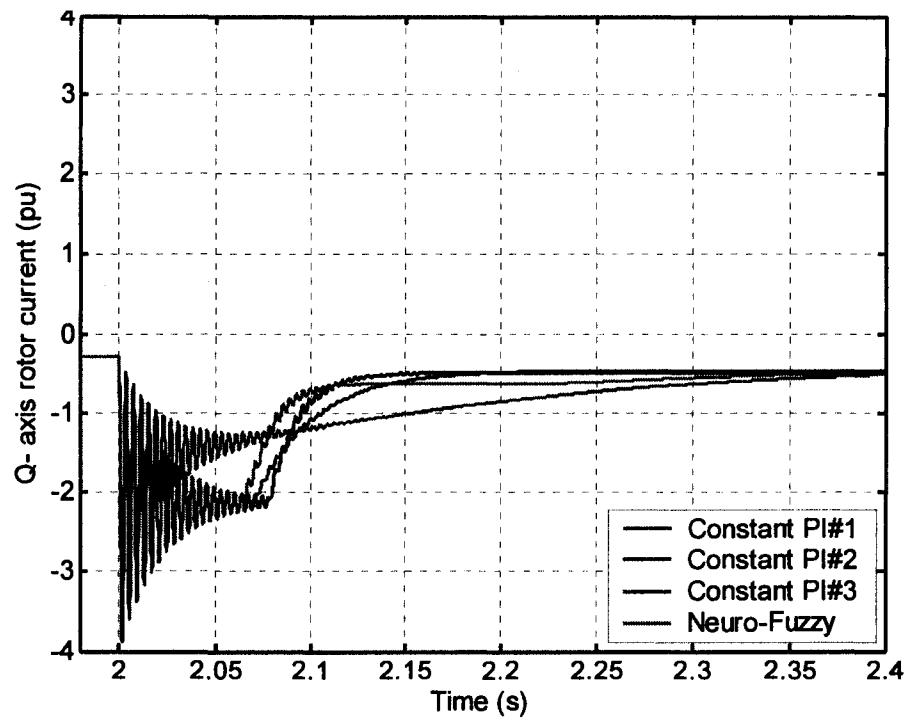


(b)

Fig. 7.13: Stator power. (a) Active power. (b) Reactive power.



(a)



(b)

Fig. 7.14: Rotor currents. (a) D- axis rotor current. (b) Q- axis rotor current.

## **7.6 Simulation and results for another system**

In this section, another set of parameters are used. These parameters are of the actual experimental setup built in the next chapter. The results presented here are for comparison with the actual experimental measurements presented in the next chapter section 8.5. For the complete set of machine parameters and the tests performed to obtain them, please refer to section 8.2.

Two scenarios are considered with set points match with the ones chosen in section 8.5. The first scenario investigates the sub-synchronous operation with the generator speed increases from 1200 rpm to 1400 rpm. The second scenario investigates the super-synchronous operation with the generator speed increases from 1600 rpm to 1900 rpm. For both scenarios, a neuro-fuzzy gain scheduler is employed as shown previously. The speed response for sub-synchronous operation is shown in Fig.7.15. Figure 7.16 shows the stator current for the sub-synchronous operation while Figs 7.17 to 7.19 show the rotor line voltage, rotor phase voltage and rotor current respectively. For the super-synchronous operation, Fig. 7.20 shows the speed response, Fig. 7.21 shows the stator current while Figs. 7.22 to 7.24 show the rotor line voltage, rotor phase voltage and rotor current respectively. It can be seen that these results are in excellent agreement with the results obtained later, in section 8.5, from the experimental investigation performed on the same machine using the same controller.



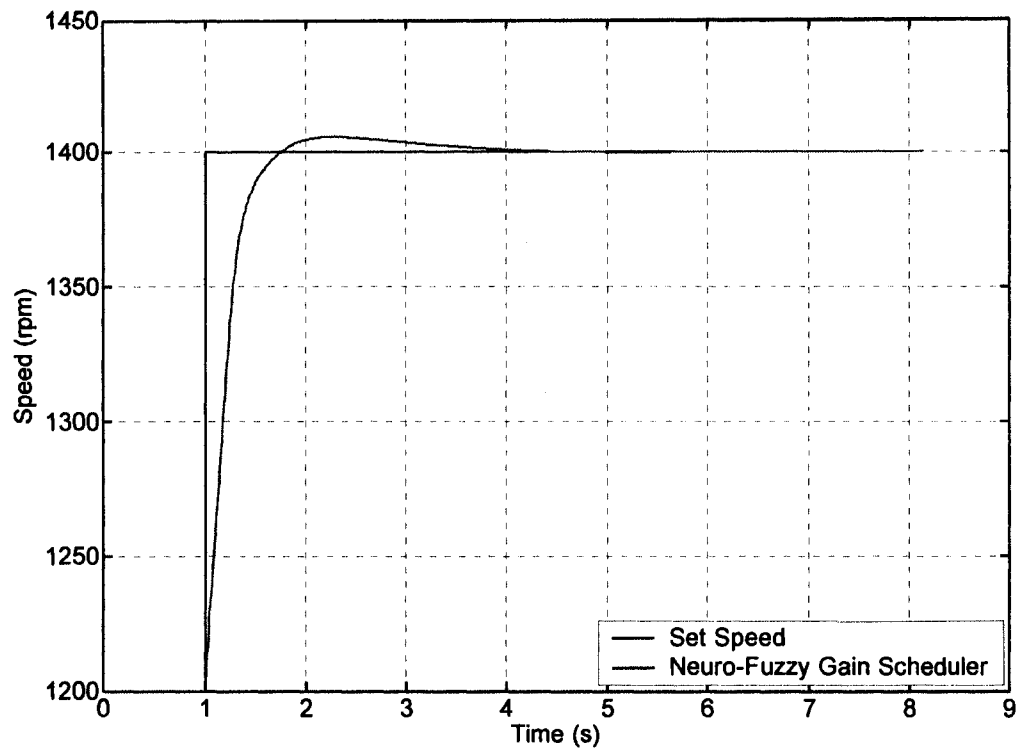


**Fig. 7.15: Speed response for sub-synchronous operation.**

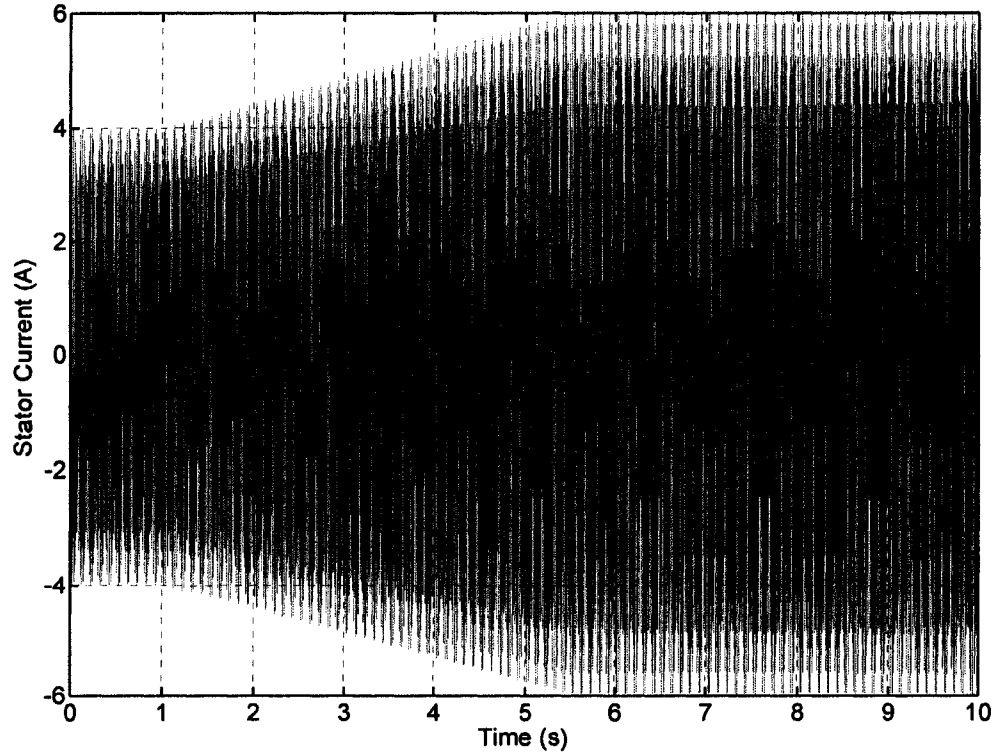


**Fig. 7.16: Stator current for sub-synchronous operation.**

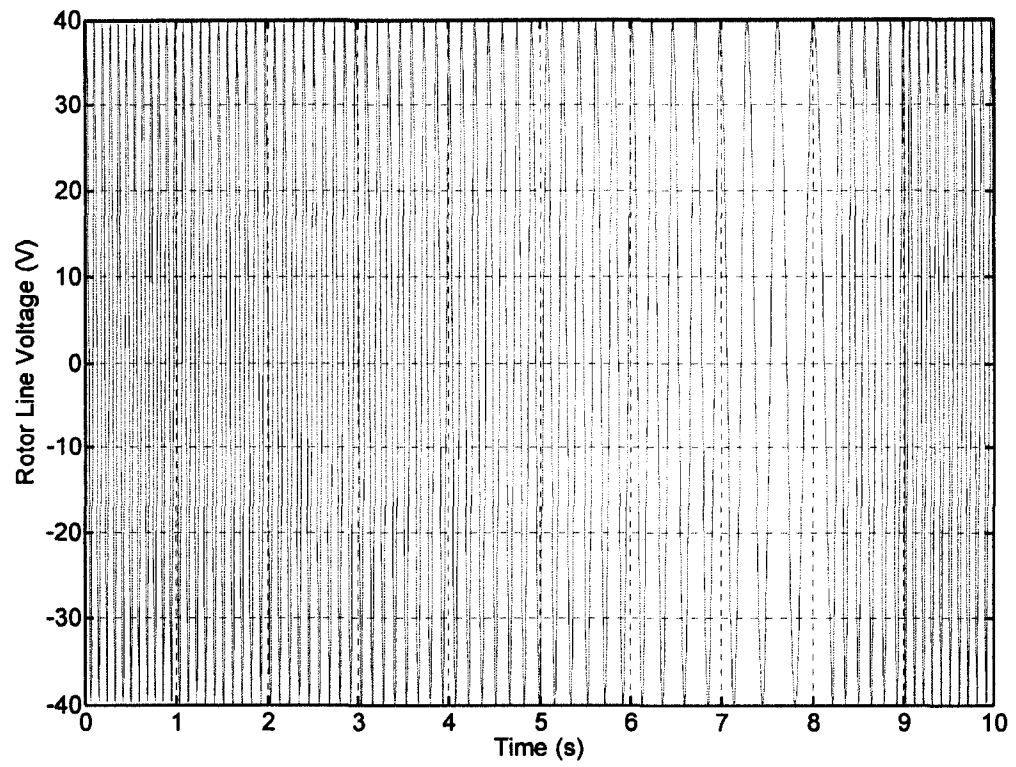


**Fig. 7.17: Rotor line voltage for sub-synchronous operation.**

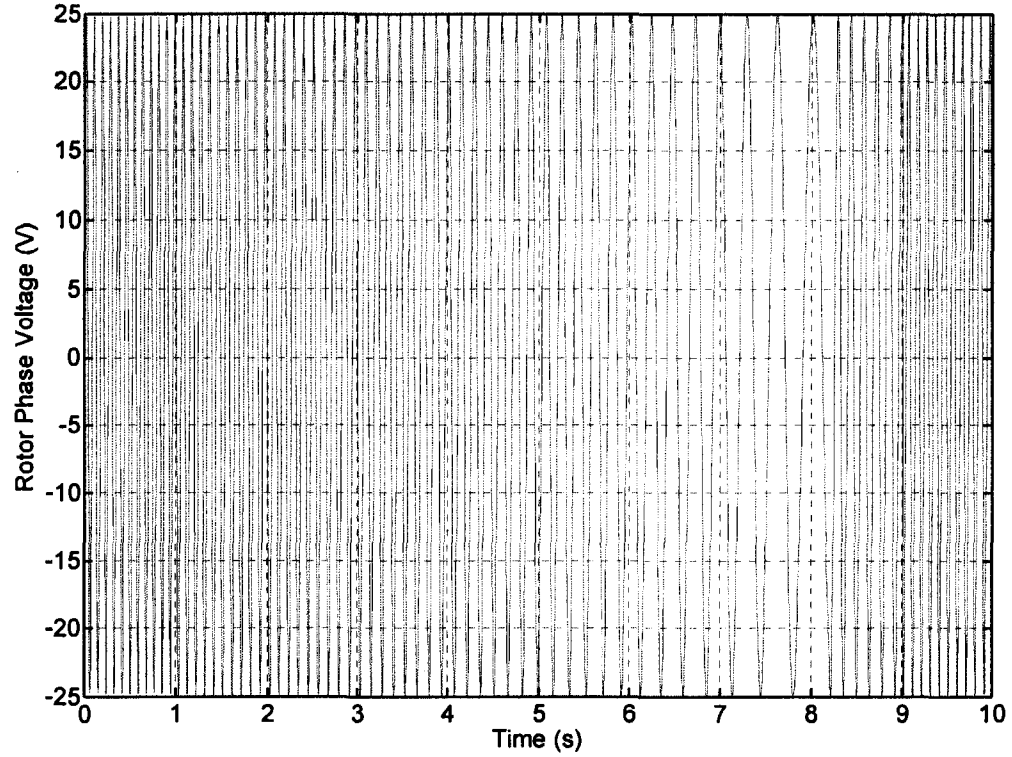


**Fig. 7.18: Rotor phase voltage for sub-synchronous operation.**

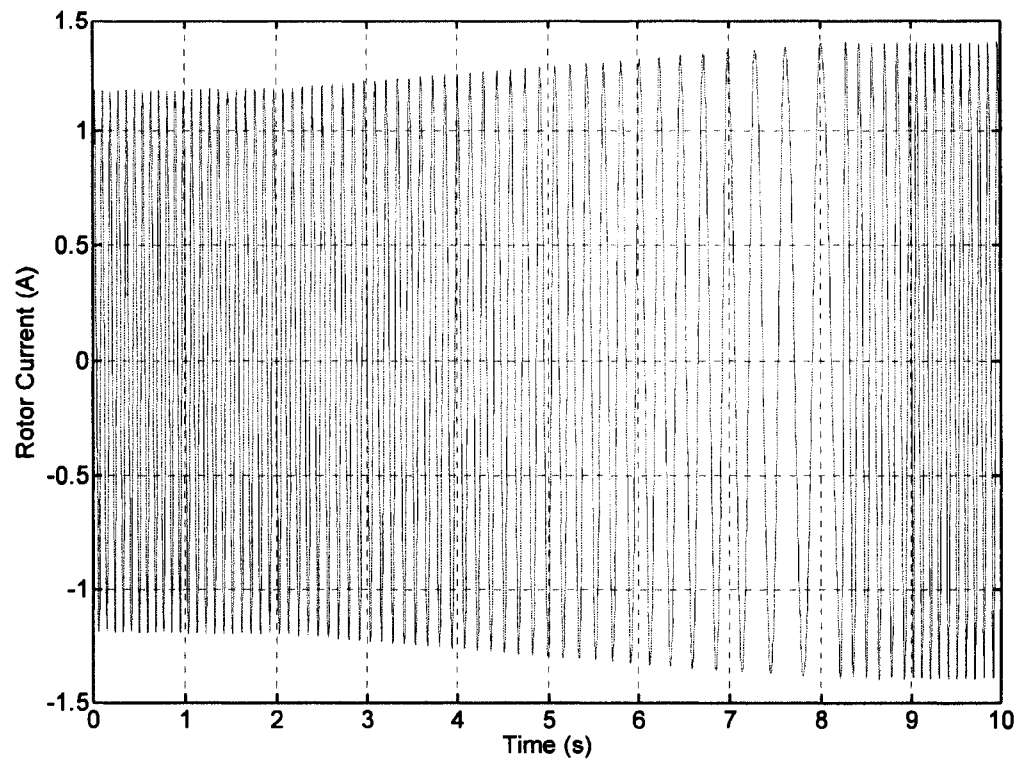


**Fig. 7.19: Rotor current for sub-synchronous operation.**

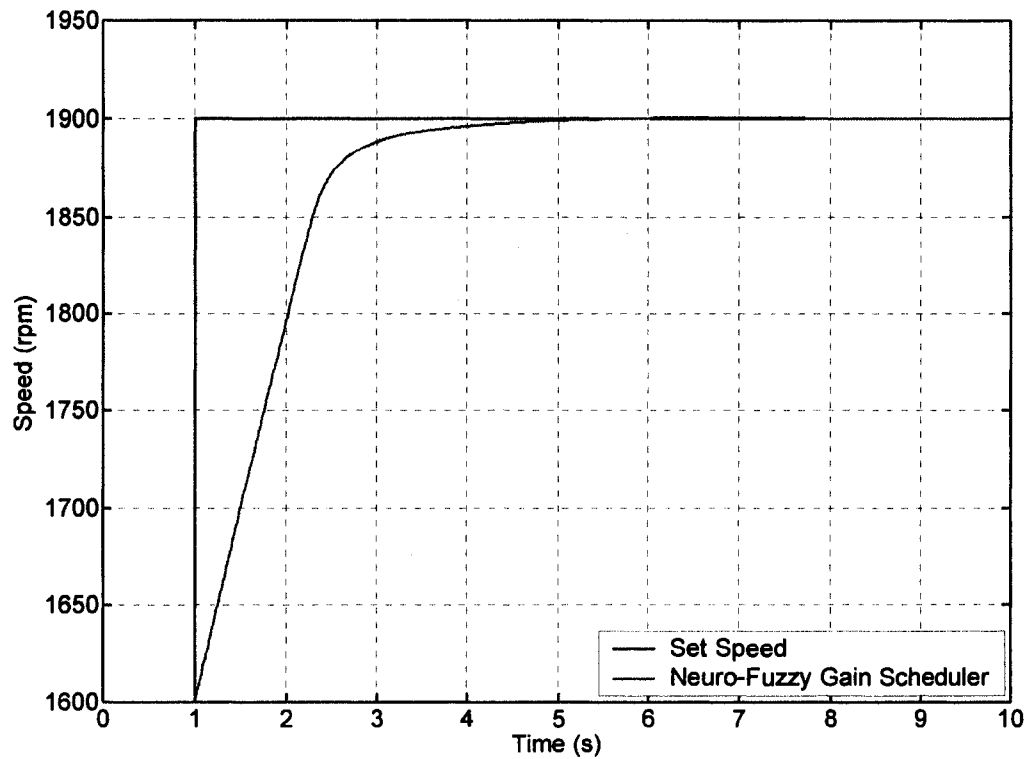


**Fig. 7.20: Speed response for super-synchronous operation.**

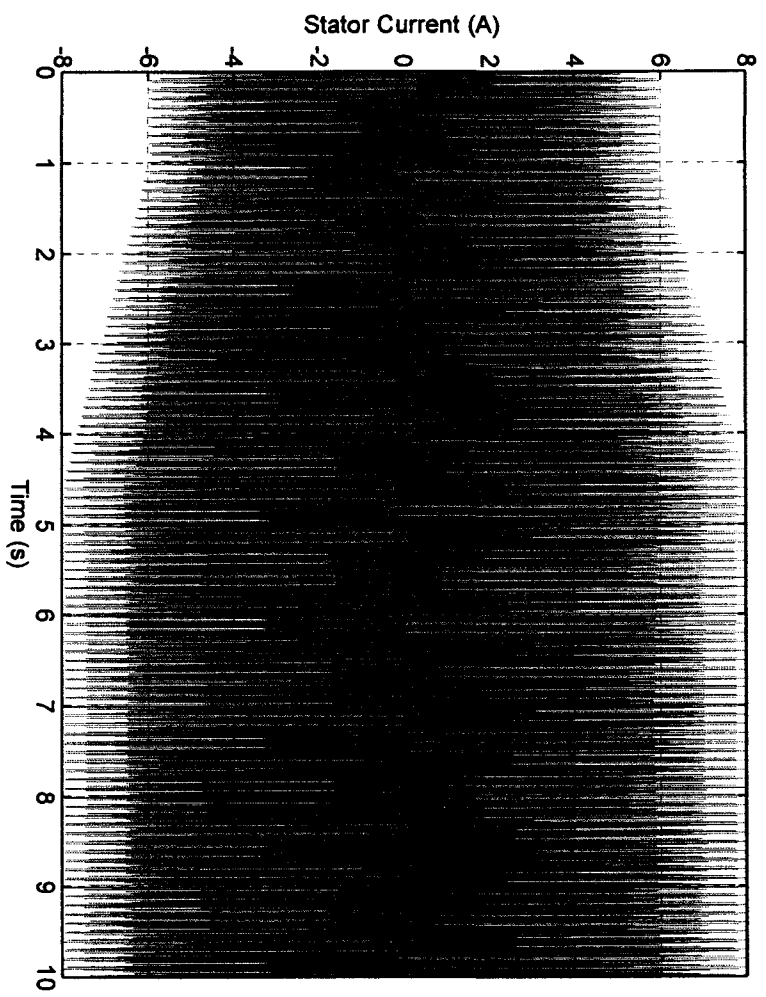


Fig. 7.21 : Stator current for super-synchronous operation.

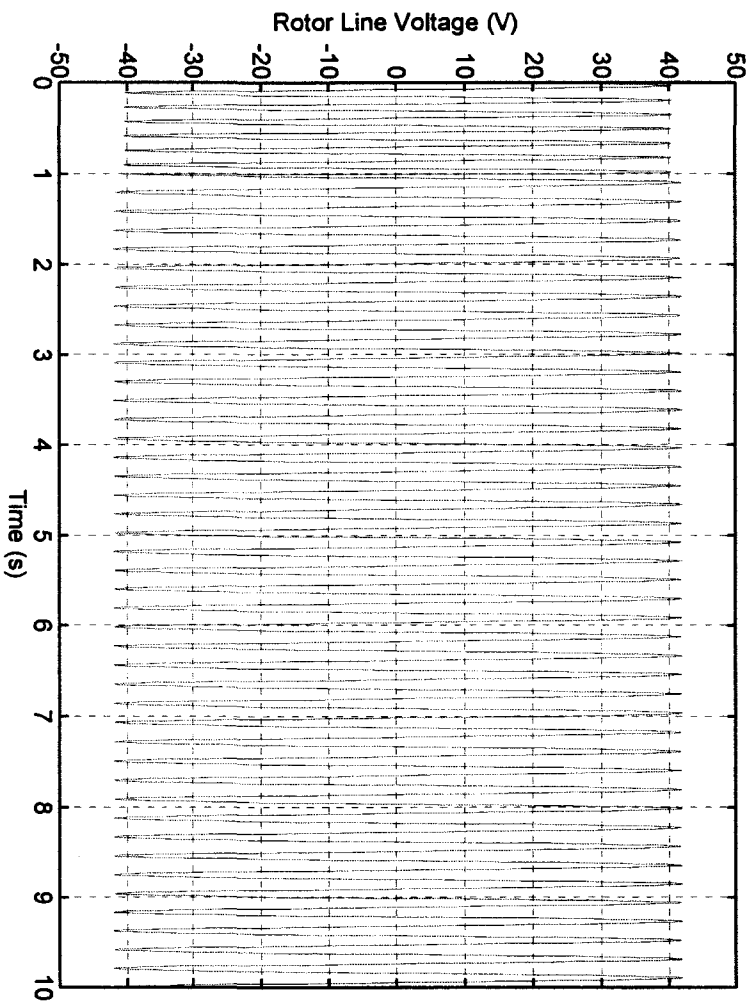
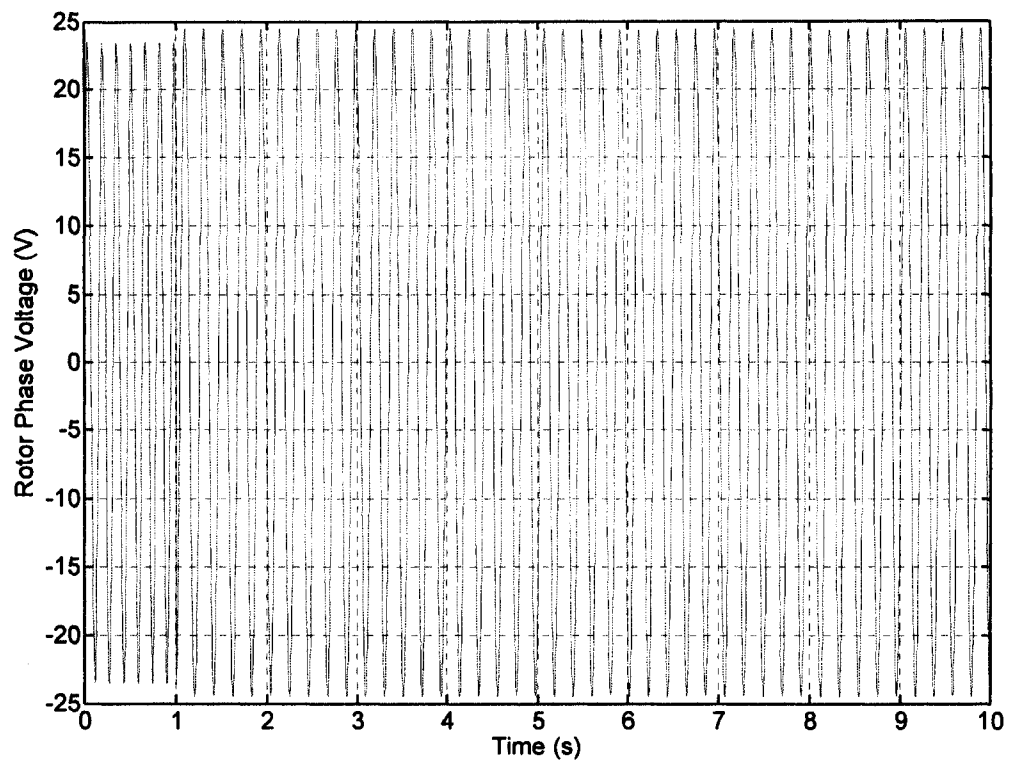
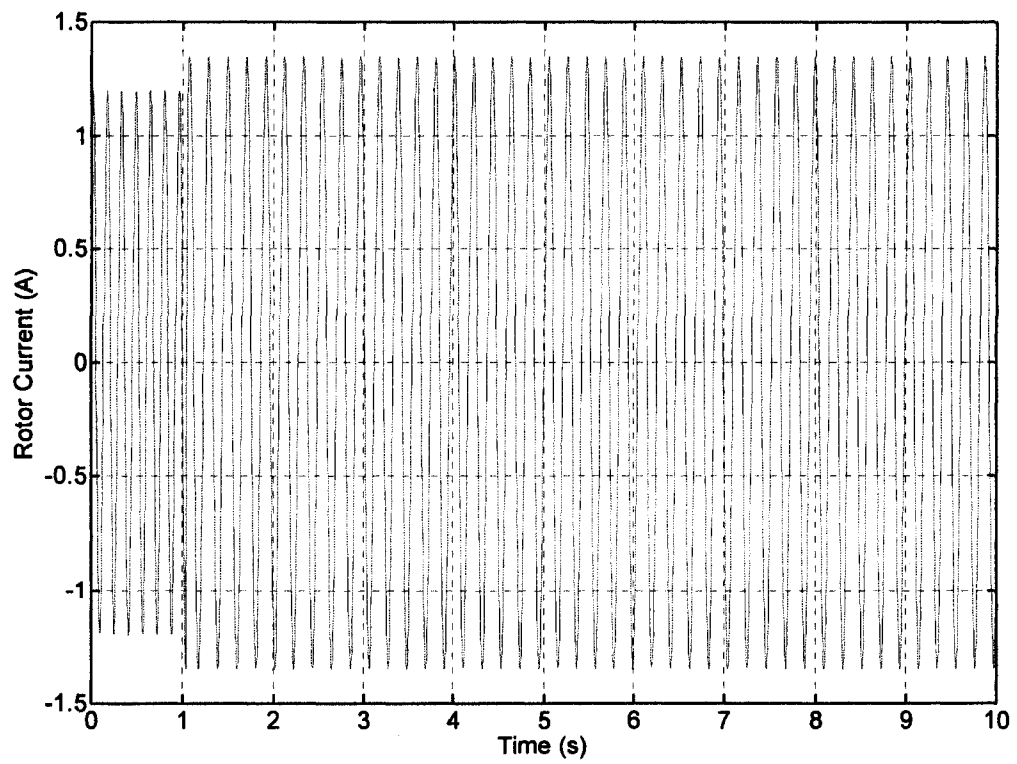


Fig. 7.22: Rotor line voltage for super-synchronous operation.



**Fig. 7.23: Rotor phase voltage for super-synchronous operation.**



**Fig. 7.24: Rotor current for super-synchronous operation.**

## 7.7 References

- [1] J. S. Jang, "ANFIS: Adaptive-network-based fuzzy inference system," *IEEE Transactions on Systems, Man, and Cybernetics*, vol. 23, no. 3, pp. 665-684, 1993.
- [2] T. Takagi and M. Sugeno, "Fuzzy identification of systems and its applications to modeling and control," *IEEE Transactions on Systems, Man, and Cybernetics*, vol. 15, pp. 116-132, 1985.
- [3] M. Sugeno and G. T. Kang, "Structure identification of fuzzy model," *Journal of Fuzzy Sets and Systems*, vol. 28, pp. 15-33, 1988.
- [4] E. H. Mamdani and S. Assilian, "An experiment in linguistic synthesis with a fuzzy logic controller," *International Journal of Man-Machine Studies*, vol. 7, no. 1, pp. 1-13, 1975.
- [5] M. Sugeno and G. T. Kang. Structure identification of fuzzy model. *Fuzzy Sets and Systems*, vol. 28, pp. 15-33, 1988.
- [6] T. Takagi and M. Sugeno, "Fuzzy identification of systems and its applications to modeling and control," *IEEE Transactions on Systems, Man, and Cybernetics*, vol. 15, pp. 116-132, 1985.
- [7] J. S. Jang and C. T. Sun, "Functional equivalence between radical basis function networks and fuzzy inference systems," *IEEE Transactions on Neural Networks*, vol. 4, no. 1, pp. 156-159, January 1993.
- [8] T. Takagi and M. Sugeno, "Derivation of fuzzy control rules from human operator's control actions," *Proceedings of the IFAC Symposium on Fuzzy Information, Knowledge Representation and Decision Analysis*, pp. 55-60, July 1983.
- [9] J. R. Jang, C. Sun and E. Mizutani, *Neuro-Fuzzy and soft computing*, Prantice-Hall, Upper Saddle River, NJ, 1997.
- [10] D. B. Parker, "Optimal algorithms for adaptive networks, second order back propagation, second order direct propagation, and second order Hebbian learning," *Proceedings of IEEE International Conference on Neural Networks*, pp. 593-600, 1987.

- [11] S. E. Fahlman, "Faster-learning variations on back-propagation: an empirical study," *Proceedings of the 1988 Connectionist Models Summer School*, pages 38-51, Carnegie Mellon University, 1988.
- [12] Vestas Wind Systems A/S: V90-3.0 MW wind turbine brochure. [Online]. Available:[http://www.vestas.com/vestas/global/en/Products/Wind\\_turbines/V90\\_3\\_0.htm](http://www.vestas.com/vestas/global/en/Products/Wind_turbines/V90_3_0.htm).
- [13] Nordex AG: N90/2500 kW wind turbine brochure. [Online]. Available: <http://www.nordex-online.com/en/products-services/wind-turbines/n90-25-mw.html>.

## **8 Experimental Setup and System Implementation**

### **8.1 Introduction**

In this chapter, experimental setup of the system under research is built and different controllers are implemented in order to investigate the system performance. In the beginning, a series of test are carried out to determine the equivalent circuit parameters of the doubly-fed induction machine. Then the power electronics interface (the back-to-back converter) is built. Next, the microcontroller is programmed. Finally, the system is tested by running the DFIG using a DC motor as a prime mover to represent the wind turbine.

### **8.2 Determination of machine parameters**

To determine the machine parameters, a series of tests are performed. Each test resolves a certain set of parameters. These tests are explained in the IEEE standard of test procedure for polyphase induction motors and generators [1]. These tests are:

1. DC test: to determine stator and rotor DC resistance.
2. No-Load test: to determine stator and rotor reactance.
3. Locked rotor test: to determine machine magnetizing reactance.

These tests produce the unsaturated machine parameters. While in order to obtain a more realistic representation of the machine, saturation in the magnetic circuit should be included in the machine model as discussed in chapter 3. To determine the saturation characteristics of the machine parameters, two unconventional tests are carried out which are:

4. No-load generator test at synchronous speed: to determine the main flux saturation characteristic.

5. The  $V_f/I_a$  curve with the machine unloaded and unexcited and the o.c.c.c.: this test is performed twice, on the stator and the rotor, to determine both stator and rotor leakage reactance saturation characteristic curves.

These tests are explained in details in section 3.5.



The DFIG used in this experiment is shown in Fig. 8.1 and rated as follows:

- Rated power: 2000 W
- Rated voltage: 208 V
- Rated stator current: 9 A
- Rated rotor current: 4.5 A

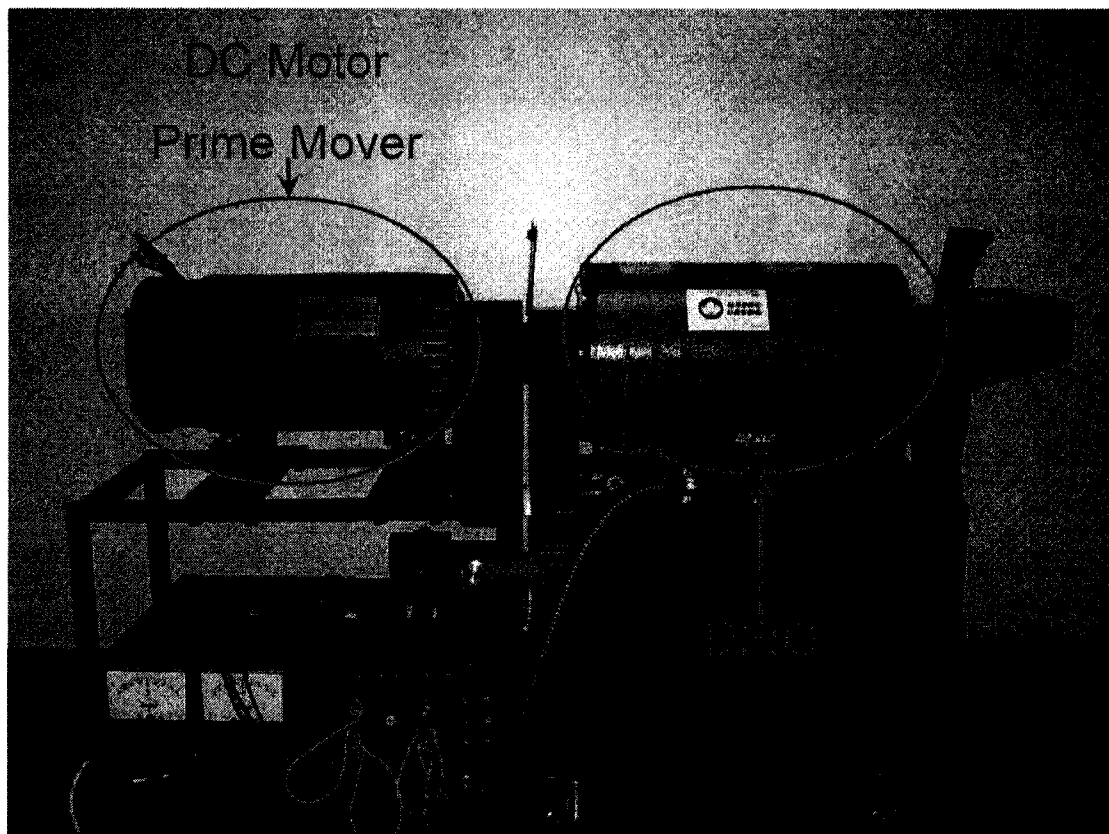


Fig. 8.1: DFIG coupled to the DC motor in the experimental setup.

### 8.2.1 DC test results

- Stator resistance:  $0.564 \, \Omega$
- Rotor resistance:  $0.450 \, \Omega$
- Cable resistance:  $0.036 \, \Omega$

### 8.2.2 No load test results

- $V_{nl}$ : 123.667 V
- $I_{nl}$ : 6.266 A
- $P_{nl}$ : 400 W

- $Q_{nl}$ : 2500 VAR

from which we get

- $Z_{eq}$ : 19.73  $\Omega$
- $P_{scl}$ : 66.44 W
- $P_{rot}$ : 333.553 W
- $X_m$ : 18.945  $\Omega$
- $L_m$ : 50.25 mH

### 8.2.3 Locked rotor test results

- $V_{lr}$ : 60 V
- $I_{lr}$ : 17.43 A
- $P_{lr}$ : 1100 W
- $Q_{lr}$ : 2500 VAR

from which we get

- $Z_{lr}$ : 1.987  $\Omega$
- $X_{ls}$ : 0.789  $\Omega$
- $X_{lr}$ : 0.789  $\Omega$
- $L_{ls}$ : 2.09 mH
- $L_{lr}$ : 2.09 mH

### 8.2.4 Main flux saturation characteristic

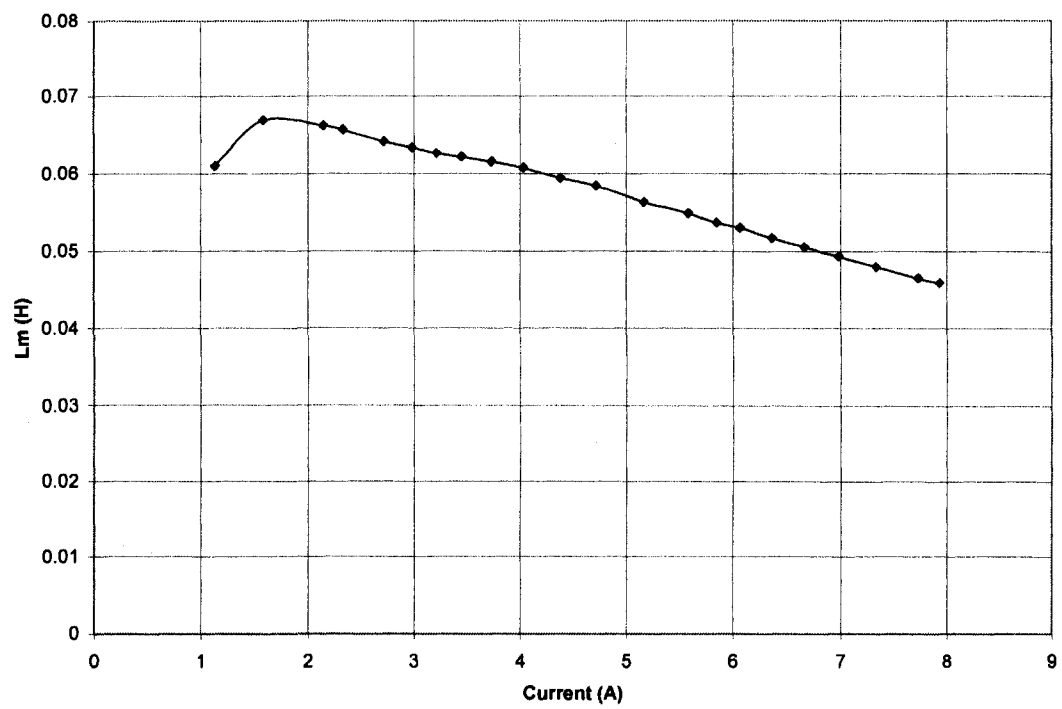


Fig. 8.2: Main flux saturation characteristic.

### 8.2.5 Stator and rotor leakage flux saturation characteristic

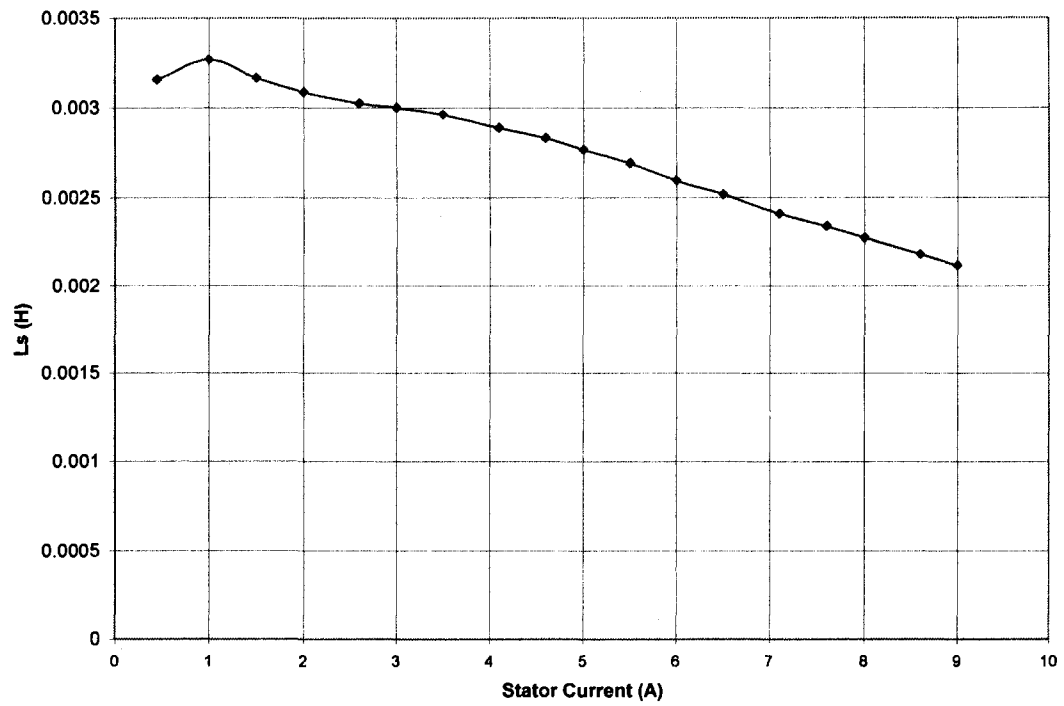


Fig. 8.3: Stator leakage flux saturation characteristic.

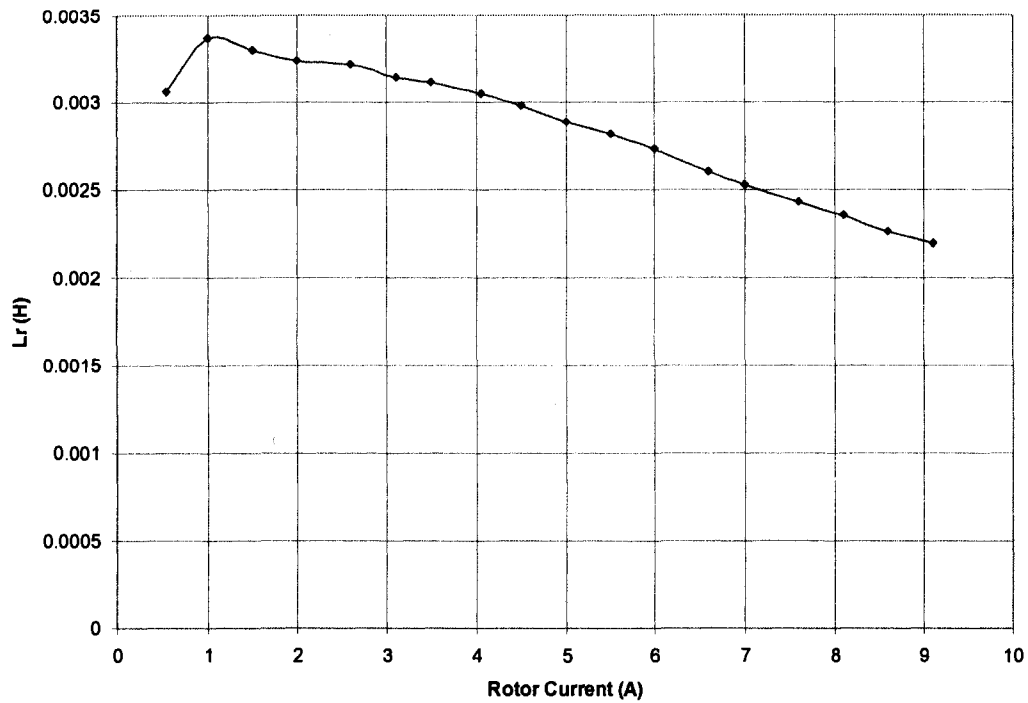


Fig. 8.4: Rotor leakage flux saturation characteristic.

### 8.3 Power electronics system components

The first stage in the process of building the power electronic interface is choosing the components. This depends on the required task and the system parameters. In the setup considered here, it is required to control the power flow in the rotor circuit of a DFIG rated 3500W, which is typically 0.25pu, ie. almost 1000W. The voltage is 208V max. and current is 3A max. The power electronic devices are mainly switches which operate (open/close) according to prescribed sequence (managed by a microprocessor or microcontroller) by sending the commands in form of firing signals. So, there are three interconnected systems, the microcontroller, the power electronic switches and the power system. Each system operates at a different voltage level so electrical isolation is mandatory. The interconnection between each system can be seen in Fig. 8.5.

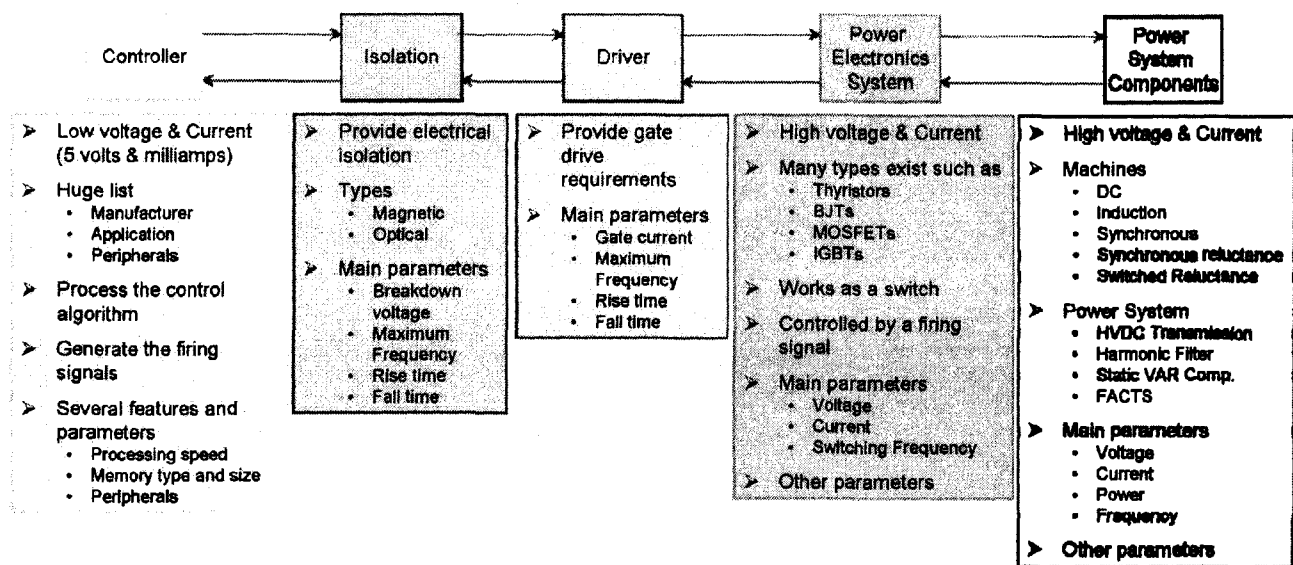


Fig. 8.5: Power electronics system showing the interaction between various subsystems.

### 8.3.1 The microprocessor or microcontroller

#### 8.3.1.1 Introduction

The remarkable increase in the speed and power of digital computers and special purpose hardware over recent years has ensured the continued growth of interest in data acquisition and microprocessors for monitoring and control of electrical machines. A signal is any variable that contains information from a transducer or from a controller that can be manipulated for a given application.

Each measurement system in the experimental set up involves sensors, signal conditioning, transmission, sampling, manipulation and interpretation of the resultant data. The output of the measurement process is presented to be displayed or processed for the control of physical parameters. The over all interconnection of a data acquisition and signal processing system is shown in Fig. 8.6.

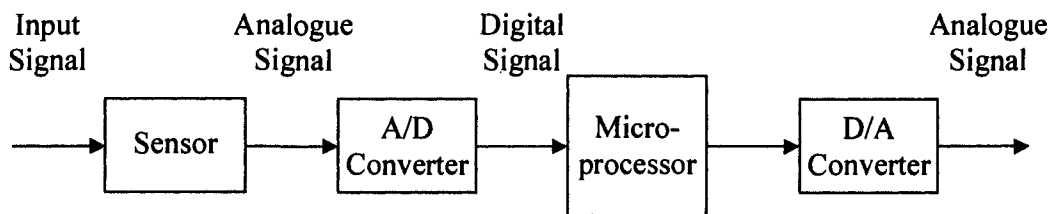


Fig. 8.6: Microcontroller based control system.

#### 8.3.1.2 Requirements

The main function of the microprocessor is to generate the firing signals to control the operation of the converters based on the control algorithm and the input states of system.

So, practically speaking, control of a 3-phase power converter (rectifier or inverter) requires pulse-width modulated control of the six switches of a 3-phase bridge connected as shown in Fig. 8.7. The six switches form 3 pairs of “half-bridges”, which can be used to connect the leg of a winding to the positive or the negative high-voltage DC bus. As shown in the figure, two switches on the same “half-bridge” must never be on simultaneously, otherwise the positive and negative buses will be shorted together. This condition would result in a destructive event known as “shoot-through”. If one switch is

on, then the other must be off; thus, they are driven as complementary pairs. It should also be noted that the switching devices used in the half-bridge (IGBTs or MOSFETs) often require more time to turn off than to turn on. For this reason, a minimum dead time must be inserted between the off and on time of complimentary channels. Based on this, the first requirement of the microprocessor is to generate 6 signals, 3 original and their complements. These signals are to be pulse-width modulated with the ability to insert a controllable dead-time.

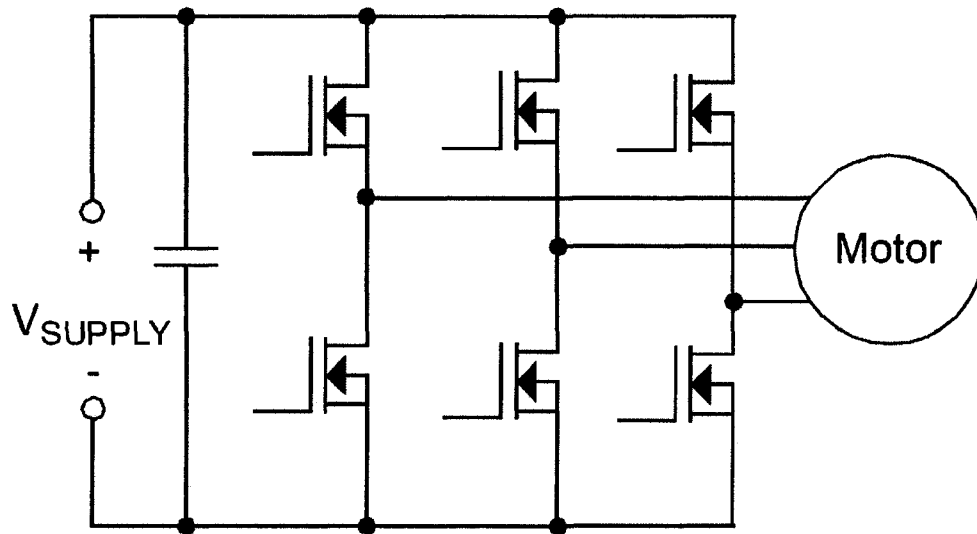


**Fig. 8.7: Power electronics converter.**

For the microprocessor to interact with the system, it should be able to measure the input variables. These input variables in this case are the voltage, current and speed of the machine with the ability to add more variables such as the set speed. These variables are usually inputted through an analogue to digital converter. Some microprocessors or microcontrollers designed for speed control applications are equipped with special port for interfacing to a quadrature encoder. This encoder generates two streams of pulses shifted  $90^\circ$  from each other with a specific number of pulses per revolution as shown in Fig. 8.8. The quadrature encoder interface (QEI) on the microprocessor has the ability to calculate the speed of the machine.



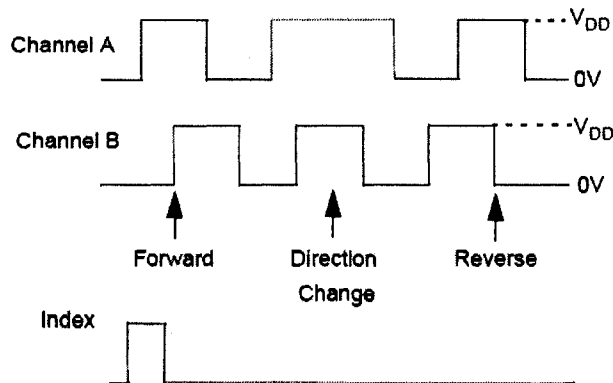


Fig. 8.8: Quadrature encoder output signal.

### 8.3.1.3 PIC<sup>®</sup>18F4431

Based on the above discussion, the Microchip<sup>®</sup> PIC<sup>®</sup> 18F4431 microcontroller was chosen. The 18F4431 has high computational performance at an economical price, with the addition of high endurance enhanced Flash program memory and a high-speed 10-bit A/D Converter. On top of these features, the PIC18F4431 introduces design enhancements that make this microcontroller a logical choice for many high performance, power control and motor control applications. These special peripherals include:

- 14-Bit Resolution Power Control PWM module (PCPWM) with Programmable Dead-time Insertion
- Motion Feedback Module (MFM), including a 3-Channel Input Capture (IC) module and Quadrature Encoder Interface (QEI)
- High-Speed 10-Bit A/D Converter (HSADC)

The PCPWM can generate up to eight complementary PWM outputs with dead-band time insertion. Overdrive current is detected by off-chip analog comparators or the digital Fault inputs (FLTA, FLTB).

The MFM Quadrature Encoder Interface provides precise rotor position feedback and/or velocity measurement. The MFM 3x input capture or external interrupts can be used to detect the rotor state for electrically commutated motor applications using Hall sensor feedback, such as BLDC motor drives.

The PIC18F4431 also feature Flash program memory and an internal RC oscillator with built-in LP modes.

The PIC18F4431 has 16384 bytes of program memory which can occupy 8192 single word instructions. For data memory, it has 768 bytes of SRAM and 256 bytes of EEPROM. It also has 36 digital I/O channels and 9 10-Bit A/D channels. It has 8 14-Bit PWM channels. For timers, it has 1 8-Bit timer and 3 16-Bit timers. It also has 32 interrupt sources. The major components of the PIC18F4431 are shown in Fig. 8.9.

The 18F4431 has the following distinctive features:

- **14-Bit Power Control PWM Module:**
  - Up to 4 Channels with Complementary Outputs
  - Edge or Center-Aligned Operation
  - Flexible Dead-Band Generator
  - Hardware Fault Protection Inputs
  - Simultaneous Update of Duty Cycle and Period:
    - Flexible Special Event Trigger output
- **Motion Feedback Module:**
  - Three Independent Input Capture Channels:
    - Flexible operating modes for period and pulse-width measurement
    - Special Hall sensor interface module
    - Special Event Trigger output to other modules
  - Quadrature Encoder Interface:
    - 2-phase inputs and one index input from encoder
    - High and low position tracking with direction status and change of direction interrupt
    - Velocity measurement
- **High-Speed, 200 ksps 10-Bit A/D Converter:**
  - Up to 9 Channels
  - Simultaneous, Two-Channel Sampling
  - Sequential Sampling: 1, 2 or 4 Selected Channels
  - Auto-Conversion Capability
  - 4-Word FIFO with Selectable Interrupt Frequency

- Selectable External Conversion Triggers
- Programmable Acquisition Time
- **Flexible Oscillator Structure:**
  - Four Crystal modes up to 40 MHz
  - Two External Clock modes up to 40 MHz
  - Internal Oscillator Block:
    - 8 user-selectable frequencies: 31 kHz to 8 MHz
    - OSCTUNE can compensate for frequency drift
  - Secondary Oscillator using Timer1 @ 32 kHz
  - Fail-Safe Clock Monitor:
    - Allows for safe shutdown of device if clock fails
- **Power-Managed Modes:**
  - Run: CPU on, Peripherals on
  - Idle: CPU off, Peripherals on
  - Sleep: CPU off, Peripherals off
  - Idle mode Currents Down to 5.8  $\mu$ A, Typical
  - Sleep Current Down to 0.1  $\mu$ A, Typical
  - Timer1 Oscillator, 1.8  $\mu$ A, Typical, 32 kHz, 2V
  - Watchdog Timer (WDT), 2.1  $\mu$ A, typical
  - Oscillator Two-Speed Start-up
- **Peripheral Highlights:**
  - High-Current Sink/Source 25 mA/25 mA
  - Three External Interrupts
  - Two Capture/Compare/PWM (CCP) modules:
    - Capture is 16-bit, max. resolution 6.25 ns (TCY/16)
    - Compare is 16-bit, max. resolution 100 ns (TCY)
    - PWM output: PWM resolution is 1 to 10 bits
  - Enhanced USART module:
    - Supports RS-485, RS-232 and LIN 1.2
    - Auto-wake-up on Start bit
    - Auto-Baud Detect

- RS-232 Operation using Internal Oscillator Block (no external crystal required)
- **Special Microcontroller Features:**
  - 100,000 Erase/Write Cycle Enhanced Flash Program Memory, Typical
  - 1,000,000 Erase/Write Cycle Data EEPROM Memory, Typical
  - Flash/Data EEPROM Retention: 100 Years
  - Self-Programmable under Software Control
  - Priority Levels for Interrupts
  - 8 x 8 Single-Cycle Hardware Multiplier
  - Extended Watchdog Timer (WDT):
    - Programmable period from 41 ms to 131s
  - Single-Supply In-Circuit Serial Programming. (ICSP.) via Two Pins
  - In-Circuit Debug (ICD) via Two Pins:
    - Drives PWM outputs safely when debugging

These features along with the ease of programming in either assembly language, only 75 instructions in the instruction set, or precompiled high level programming language such as basic or C makes the PIC® 18F4431 a very attractive solution for power converters' control.

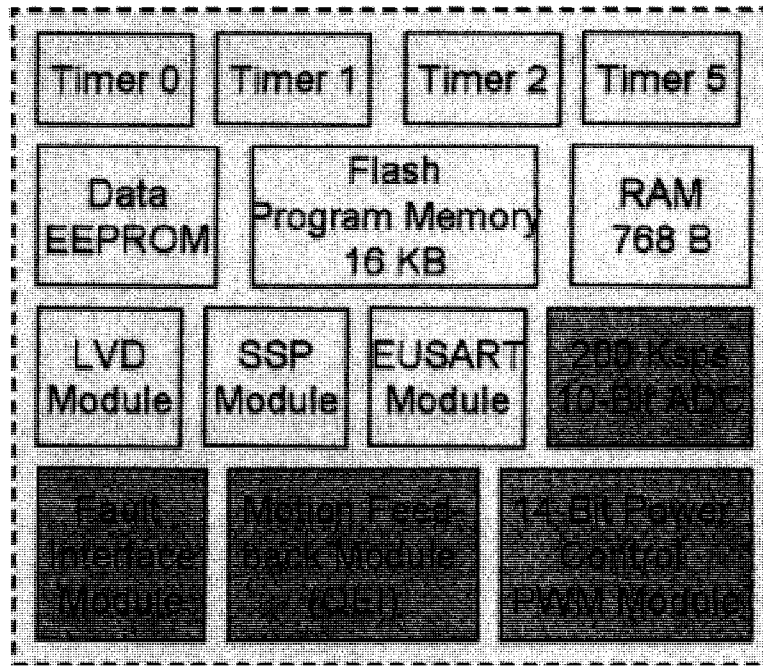


Fig. 8.9: PIC®18F4431 modules.

#### 8.3.1.3.1 Power Control PWM Module

In PWM mode, this module provides 1, 2 or 4 modulated outputs for controlling half-bridge and full-bridge drivers. Other features include auto-shutdown on fault detection and auto-restart to reactivate outputs once the condition has cleared.

The Power Control PWM module simplifies the task of generating multiple, synchronized Pulse-Width Modulated (PWM) outputs for use in the control of motor controllers and power conversion applications. In particular, the following power and motion control applications are supported by the PWM module:

- Three-Phase and Single-Phase AC Induction Motors
- Switched Reluctance Motors
- Brushless DC (BLDC) Motors
- Uninterruptible Power Supplies (UPS)
- Multiple DC Brush Motors

The PWM module has the following features:

- Up to eight PWM I/O pins with four duty cycle generators. Pins can be paired to get a complete half-bridge control.
- Up to 14-bit resolution, depending upon the PWM period.
- On-the-fly. PWM frequency changes.
- Edge and Center-Aligned Output modes.
- Single-Pulse Generation mode.
- Programmable dead-time control between paired PWMs.
- Interrupt support for asymmetrical updates in Center-Aligned mode.
- Output override for Electrically Commutated Motor (ECM) operation; for example, BLDC.
- Special Event Trigger comparator for scheduling other peripheral events.
- PWM outputs disable feature sets PWM outputs to their inactive state when in Debug mode.

#### ***8.3.1.3.2 High-Speed 10-Bit A/D Converter***

The high-speed Analog-to-Digital (A/D) Converter module allows conversion of an analog signal to a corresponding 10-bit digital number. This module incorporates programmable acquisition time, allowing for a channel to be selected and a conversion to be initiated without waiting for a sampling period and thus, reducing code overhead.

This high-speed 10-bit A/D module offers the following features:

- Up to 200K samples per second
- Two sample and hold inputs for dual-channel simultaneous sampling
- Selectable Simultaneous or Sequential Sampling modes
- 4-word data buffer for A/D results
- Selectable data acquisition timing
- Selectable A/D event trigger
- Operation in Sleep using internal oscillator

These features lend themselves to many applications including motor control, sensor interfacing, data acquisition and process control. In many cases, these features will reduce the software overhead associated with standard A/D modules.

#### **8.3.1.3.3 Motion Feedback Module (MFM)**

This module features a Quadrature Encoder Interface (QEI) and an Input Capture (IC) module. The QEI accepts two phase inputs (QEA, QEB) and one index input (INDX) from an incremental encoder.

The QEI supports high and low precision position tracking, direction status and change of direction interrupt and velocity measurement. The input capture features 3 channels of independent input capture with Timer5 as the time base, a Special Event Trigger to other modules and an adjustable noise filter on each IC input.

The Motion Feedback Module (MFM) is a special purpose peripheral designed for motion feedback applications. Together with the Power Control PWM (PCPWM) module, it provides a variety of control solutions for a wide range of electric motors.

The module actually consists of two hardware submodules:

- Input Capture (IC)
- Quadrature Encoder Interface (QEI)

Together with Timer5, these modules provide a number of options for motion and control applications. Many of the features for the IC and QEI submodules are fully programmable, creating a flexible peripheral structure that can accommodate a wide range of in-system uses.

### **8.3.2 The isolation**

The electrical isolation between circuits operating at different voltage levels is extremely essential. This isolation can be either magnetically or optically. The magnetic isolation is accomplished by using specially designed type of transformers called pulse transformers. These transformers are designed to work with non-sinusoidal waveforms at high frequencies. These transformers have the ability to reproduce the input signal at the secondary terminals despite the high frequency. The magnitude of the output signal depends on the magnitude of the input signal and the turns-ratio which is a drawback. If the design requires the increase of the output signal magnitude, then a new pulse transformer is required. Moreover, the pulse transformers are more expensive than the optical isolators. The pulse transformer has the advantage of being able to reproduce the

input signal which is essential to some applications such as the communication applications but not required for the application in hand.

On the other hand, optical isolators are inexpensive but works as a switch. Opto-couplers or opto-isolators have an input which is simply a light emitting diode (LED). When this LED is forward biased, it operates and produces light. On the output side, there is a special bipolar junction transistor (BJT) which enters the saturation region when it receives the light and current flows from the collector to the emitter (depending on the BJT type NPN or PNP). When the LED is reverse biased, the light is removed and the BJT enters the cutoff region.

So, the opto-couplers transfers the input signal, independent of its shape to the output in form of pulses which is very suitable for this application. The main characteristics of the opto-couplers are:

- Isolation voltage
- Input reverse voltage
- Collector-emitter voltage
- Cut-off frequency
- Rise time
- Fall time

Based on the above parameters, the opto-coupler chosen is LTV-827 from LITE-ON and has the schematic as shown in Fig 8.10. Table 8.1 lists the opto-coupler absolute maximum ratings while Table 8.2 lists its electrical and optical characteristics. These values are important in deciding the operating conditions of the opto-coupler.

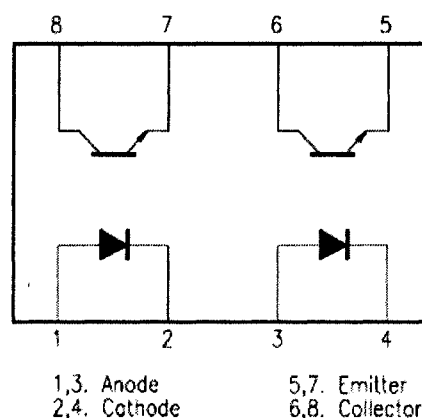


**Fig. 8.10: Opto-coupler pin and integral connection diagram.**



Table 8.1: Opto-coupler absolute maximum ratings.

**Absolute Maximum Ratings**

(Ta=25°C)

Parameter		Symbol	Rating	Unit
Input	Forward Current	IF	50	mA
	Reverse Voltage	VR	6	V
	Power Dissipation	P	70	mW
Output	Collector-Emitter Voltage	VCEO	35	V
	Emitter-Collector Voltage	VECO	6	V
	Collector Current	IC	50	mA
	Collector Power Dissipation	PC	150	mW
Total Power Dissipation		Ptot	200	mW
Operating Temperature		Topr	-30~+100	°C
Storage Temperature		Tstg	-55~+125	°C
*1.Isolation Voltage		Viso	5	KVrms
*2.Soldering Temperature		Tsol	260	°C

Table 8.2: Opto-coupler electrical and optical characteristics.

**Electrical/Optical Characteristics**

(Ta=25°C)

Parameter		Symbol	Min.	Typ.	Max.	Unit	Conditions
Input	Forward Voltage	VF	—	1.2	1.4	V	IF=20mA
	Reverse Current	IR	—	—	10	μA	VR=4V
	Terminal Capacitance	Ct	—	30	250	pF	V=0, f=1KHz
Output	Collector Dark Current	ICEO	—	—	100	nA	VCE=20V
	Collector-Emitter Breakdown Voltage	BVCEO	35	—	—	V	IC=0.1mA
	Emitter-Collector Breakdown Voltage	BVECO	6	—	—	V	IE=10 μA
	*Current Transfer Ratio	CTR	50	—	600	%	IF=5mA, VCE=5V Rθ=∞
Transfer Characteristics	Collector Current	IC	2.5	—	30	mA	IF=20mA, VCE=5V
	Collector-emitter Saturation Voltage	VCE(sat)	—	0.1	0.2	V	IF=20mA, IC=1mA
	Isolation Resistance	Riso	5 × 10 <sup>10</sup>	10 <sup>11</sup>	—	Ω	DC500V, 40~60% R.H.
	Floating Capacitance	Cf	—	0.6	1.0	pF	V=0, f=1MHz
	Cut-off Frequency	fc	—	80	—	KHz	VCE=5V, IC=2mA RL=100 Ω, -3dB
	Response Time (Rise)	tr	—	4	18	μs	VCE=2V, IC=2mA
	Response Time (Fall)	tf	—	3	18	μs	RL=100 Ω

**8.3.3 The power electronic components**

The bipolar transistor was the only “real” power transistor until the MOSFET came along in the 1970’s. The bipolar transistor requires a high base current to turn on, has relatively slow turn-off characteristics (known as current tail), and is liable for thermal runaway due to a negative temperature co-efficient. In addition, the lowest attainable on-state voltage or conduction loss is governed by the collector-emitter saturation voltage  $V_{CE(SAT)}$ .

The MOSFET, however, is a device that is voltage-, and not current-, controlled. MOSFETs have a positive temperature coefficient, stopping thermal runaway. The on-state-resistance has no theoretical limit, hence on-state losses can be far lower. The

MOSFET also has a body-drain diode, which is particularly useful in dealing with limited free wheeling currents.

All these advantages and the comparative elimination of the current tail soon meant that the MOSFET became the device of choice for power switch designs. Then in the 1980s the IGBT came along. The IGBT is a cross between the bipolar and MOSFET transistors.

The IGBT has the output switching and conduction characteristics of a bipolar transistor but is voltage-controlled like a MOSFET. In general, this means it has the advantages of high-current handling capability of a bipolar with the ease of control of a MOSFET. However, the IGBT still has the disadvantages of a comparatively large current tail and no body drain diode.

Early versions of the IGBT are also prone to latch up, but nowadays, this is completely eliminated. Another potential problem with some IGBT types is the negative temperature co-efficient, which could lead to thermal runaway and makes the paralleling of devices hard to effectively achieve. This problem is now being addressed in the latest generations of IGBTs that are based on “non-punch through” (NPT) technology. This technology has the same basic IGBT structure but is based on bulk-diffused silicon, rather than the epitaxial material that both IGBTs and MOSFETs have historically used.

The IGBT technology is certainly the device of choice for breakdown voltages above 1000V, while the MOSFET is certainly the device of choice for device breakdown voltages below 250V. Between 250 to 1000V, there are many technical papers available from manufacturers of these devices, some preferring MOSFETs, some IGBTs. However, choosing between IGBTs and MOSFETs is very application-specific and cost, size, speed and thermal requirements should all be considered.

IGBTs have a number of limitations including:

1. Lower switching speeds in comparison with MOSFETs, which is in part due to the tail current effect they exhibit during turn off (see Fig. 8.11).
2. Higher switching losses compared to MOSFETs, caused by the tail current effect (see Fig. 8.11).
3. Possibility of uncontrollable latch-up (stays-on) under overstress conditions (high  $dv/dt$  or  $di/dt$ )

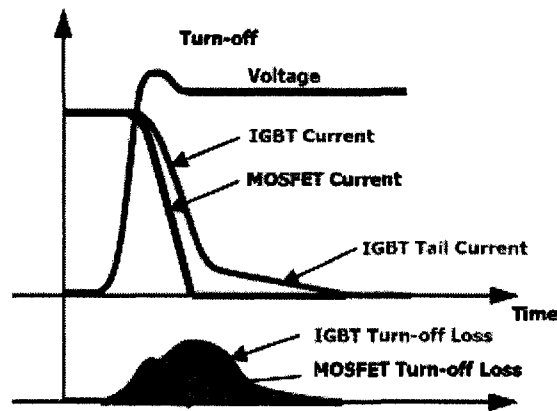


Fig. 8.11: MOSFET and IGBT turn-off behavior.

One of the challenges presently facing designers is the question of which device is better. Well, the answer is: **IT DEPENDS**. The choice of a MOSFET versus an IGBT in a given application depends greatly on the application needs and requirements. In developing a simple criteria to choose between MOSFETs and IGBTs in a given application, the switching frequency and the device's voltage withstand requirement can be used. Fig. 8.12 shows the application range of MOSFETs and IGBTs based on the above criteria. It is clear that MOSFETs are still the most dominant in low voltage (<300V) and low to medium power applications (<10kW) at any switching frequency. As the voltage requirements increase, IGBTs become more appealing. However, at higher switching frequencies, MOSFETs are still superior due to their faster switching speeds. Higher frequency operation of IGBTs is only feasible by employing soft switching power conversion techniques.

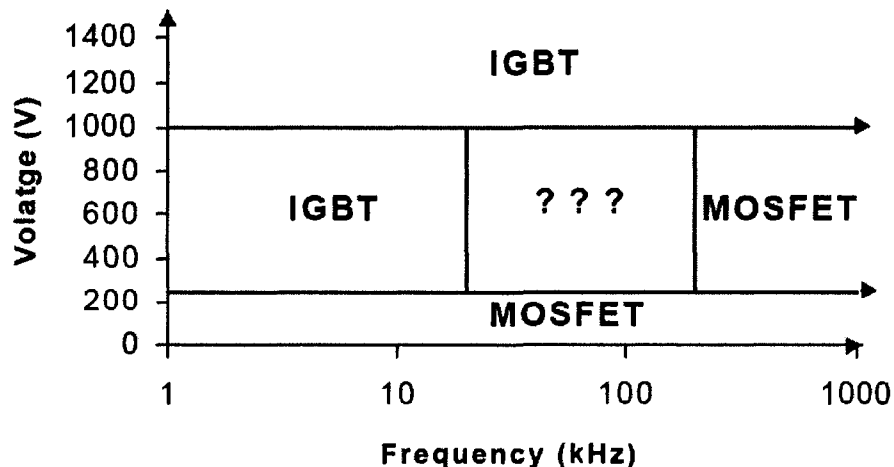


Fig. 8.12: MOSFET and IGBT operating range.

**IGBTs have been the preferred device under these conditions:**

- Low duty cycle
- Low frequency (<20kHz)
- Narrow or small line or load variations
- High-voltage applications (>1000V)
- Operation at high junction temperature is allowed (>100°C)
- >5kW output power

**Typical IGBT applications include:**

- Motor control: Frequency <20kHz, short circuit/in-rush limit protection
- Uninterruptible power supply (UPS): Constant load, typically low frequency
- Welding: High average current, low frequency (<50kHz), ZVS circuitry
- Low-power lighting: Low frequency (<100kHz)

**MOSFETs are preferred in:**

- High frequency applications (>200kHz)
- Wide line or load variations
- Long duty cycles
- Low-voltage applications (<250V)
- < 500W output power

**Typical MOSFET applications include:**


- Switch mode power supplies (SMPS): Hard switching above 200kHz
- Switch mode power supplies (SMPS): ZVS below 1000 watts
- Battery charging

Based on the above, knowing that the working voltage is 208V and current is 8A maximum with a switching frequency of 5kHz. The best choice is certainly the MOSFET. The chosen MOSFET is from International Rectifier (IRF) part number IFR-740. It is an N-Channel power MOSFET having the following parameters:

- Rated Voltage: 400V
- Rated Current: 10A
- Resistance: 0.55Ω

Detailed electrical characteristics are as shown in Table 8.3.

**Table 8.3: MOSFET electrical characteristics.**

	Parameter	Min.	Typ.	Max.	Unit	Test Conditions
$V_{(BR)DSS}$	Drain-to-Source Breakdown Voltage	400	—	—	V	$V_{GS}=0V$ , $I_D=250\mu A$
$\Delta V_{(BR)DSS}/\Delta T_J$	Breakdown Voltage Temp. Coefficient	—	0.49	—	V/°C	Reference to 25°C, $I_D=1mA$
$R_{DS(on)}$	Static Drain-to-Source On-Resistance	—	—	0.55	$\Omega$	$V_{GS}=10V$ , $I_D=6.0A$
$V_{GS(th)}$	Gate Threshold Voltage	2.0	—	4.0	V	$V_{DS}=V_{GS}$ , $I_D=250\mu A$
$g_{fs}$	Forward Transconductance	5.8	—	—		$V_{DS}=50V$ , $I_D=6.0A$
$I_{DSS}$	Drain-to-Source Leakage Current	—	—	25	$\mu A$	$V_{DS}=400V$ , $V_{GS}=0V$
		—	—	250		$V_{DS}=320V$ , $V_{GS}=0V$ , $T_J=125^\circ C$
$I_{GSS}$	Gate-to-Source Forward Leakage	—	—	100	nA	$V_{GS}=20V$
	Gate-to-Source Reverse Leakage	—	—	-100		$V_{GS}=-20V$
$Q_g$	Total Gate Charge	—	—	63	nC	$I_D=10A$ $V_{DS}=320V$ $V_{GS}=10V$
$Q_{gs}$	Gate-to-Source Charge	—	—	9.0		
$Q_{gd}$	Gate-to-Drain ("Miller") Charge	—	—	32		
$t_{d(on)}$	Turn-on Delay Time	—	14	—	ns	$V_{DD}=200V$ $I_D=10A$ $R_G=9.1\Omega$ $R_D=20\Omega$
$t_r$	Rise Time	—	27	—		
$t_{d(off)}$	Turn-off Delay Time	—	50	—		
$t_f$	Fall Time	—	24	—		
$L_D$	Internal Drain Inductance	—	4.5	—	nH	Between lead 6mm (0.25in.) from package and center of die contact 
$L_S$	Internal Source Inductance	—	7.5	—		
$C_{iss}$	Input Capacitance	—	1400	—	pF	$V_{GS}=0V$ $V_{DS}=25V$ $f=1.0MHz$
$C_{oss}$	Output Capacitance	—	330	—		
$C_{rss}$	Reverse Transfer Capacitance	—	120	—		

### 8.3.4 Gate drivers

To turn a power MOSFET on, the gate terminal must be set to a voltage at least 10 volts greater than the source terminal (about 4 volts for logic level MOSFETs). This is comfortably above the  $V_{GS(th)}$  parameter.

One feature of power MOSFETs is that they have a large stray capacitance between the gate and the other terminals,  $C_{iss}$ . The effect of this is that when the pulse to the gate terminal arrives, it must first charge this capacitance up before the gate voltage can reach the 10 volts required. The gate terminal then effectively does take current. Therefore the circuit that drives the gate terminal should be capable of supplying a reasonable current so the stray capacitance can be charged up as quickly as possible. The best way to do this is to use a dedicated MOSFET driver chip.

There are a lot of MOSFET driver chips available from several companies. Some require the MOSFET source terminal to be grounded (for the lower 2 MOSFETs in a full bridge or just a simple switching circuit). Some can drive a MOSFET with the source at a higher voltage. These have an on-chip charge pump, which means they can generate the 22 volts required to turn the upper MOSFET in a full bridge on. Some can supply as much as 6 Amps current as a very short pulse to charge up the stray gate capacitance.

Often a low value resistor is inserted between the MOSFET driver and the MOSFET gate terminal. This is to dampen down any ringing oscillations caused by the lead inductance and gate capacitance which can otherwise exceed the maximum voltage allowed on the gate terminal. It also slows down the rate at which the MOSFET turns on and off. This can be useful if the intrinsic diodes in the MOSFET do not turn on fast enough.

#### **8.3.4.1 Peak current drive requirement**

Matching the MOSFET driver to the MOSFET in the application will primarily be based on how fast the application requires the power MOSFET to be turned on and off (rise and fall time of the gate voltage). The optimum rise/fall time in any application is based on many requirements, such as EMI (conducted and radiated), switching losses, lead/circuit inductance, switching frequency, etc.

The speed at which a MOSFET can be turned on and off is related to how fast the gate capacitance of the MOSFET can be charged and discharged. The relationship between gate capacitance, turn-on/turn-off time and the MOSFET driver current rating can be written as:

$$dT = \frac{dV \times C}{I} \quad (8.1)$$

Where:

$dT$  = turn-on/turn-off time

$dV$  = gate voltage

$C$  = gate capacitance (from gate charge value)

$I$  = peak drive current (for the given voltage value)

Knowing that  $Q = C \times V$ , the above equation can be rewritten as:

$$dT = \frac{Q}{I} \quad (8.2)$$

Where:

Q = total gate charge

The relationship shown in the equations above assumes that a constant current source is being used for the current ( $I$ ). By using the peak drive current of the MOSFET driver, some error will be incurred.

MOSFET drivers are rated by the driver output peak current drive capability. This peak current drive capability is generally given for one of two conditions. Either the MOSFET driver output is shorted to ground or the MOSFET driver output is at a particular voltage value (usually 4V, as this is the gate threshold voltage at which the MOSFET begins to turn on). The peak current rating is also generally stated for the maximum bias voltage of the part. This means that if the MOSFET driver is being used with a lower bias voltage, the peak current drive capability of the MOSFET driver will be lower.

In the case of the IRF740, the total gate charge is  $63nC$  with a turn-on time of  $41ns$  which give a gate current of 1.53A. The selected gate driver is IRS2186 from International Rectifier. It is capable of providing 4A for the MOSFET gate. It has the following electrical characteristics as shown in Table 8.4.

**Table 8.4: MOSFET driver electrical characteristics.**

Symbol	Definition	Min.	Typ.	Max.	Units	Test Conditions
$V_{IH}$	Logic "1" input voltage	2.5	—	—	V	$V_{CC} = 10\text{ V to } 20\text{ V}$
$V_{IL}$	Logic "0" input voltage	—	—	0.8		
$V_{OH}$	High level output voltage, $V_{BIAS} - V_O$	—	—	1.4		$I_O = 0\text{ A}$
$V_{OL}$	Low level output voltage, $V_O$	—	—	0.15		$I_O = 20\text{ mA}$
$I_{LK}$	Offset supply leakage current	—	—	50	$\mu\text{A}$	$V_B = V_S = 600\text{ V}$
$I_{QBS}$	Quiescent $V_{BS}$ supply current	20	60	150		$V_{IN} = 0\text{ V or } 5\text{ V}$
$I_{QCC}$	Quiescent $V_{CC}$ supply current	50	120	240		
$I_{IN+}$	Logic "1" input bias current	—	25	60		$V_{IN} = 5\text{ V}$
$I_{IN-}$	Logic "0" input bias current	—	—	5.0		$V_{IN} = 0\text{ V}$
$V_{CCUV+}$ $V_{BSUV+}$	$V_{CC}$ and $V_{BS}$ supply undervoltage positive going threshold	8.0	8.9	9.8	V	
$V_{CCUV-}$ $V_{BSUV-}$	$V_{CC}$ and $V_{BS}$ supply undervoltage negative going threshold	7.4	8.2	9.0		
$V_{CCUMH}$ $V_{BSUMH}$	Hysteresis	0.3	0.7	—		
$I_{O+}$	Output high short circuit pulsed current	2.0	4.0	—	A	$V_O = 0\text{ V}$ , $PW \leq 10\text{ }\mu\text{s}$
$I_{O-}$	Output low short circuit pulsed current	2.0	4.0	—		$V_O = 15\text{ V}$ , $PW \leq 10\text{ }\mu\text{s}$

## 8.3.5 Feedback

### 8.3.5.1 Introduction

Sensors are a critical component in a motor control system. They are used to sense the current, position, speed and direction of the rotating motor. Recent advancements in sensor technology have improved the accuracy and reliability of sensors, while reducing the cost. Many sensors are now available that integrate the sensor and signal-conditioning circuitry into a single package.

In most motor control systems, several sensors are used to provide feedback information on the motor. These sensors are used in the control loop and to improve the reliability by detecting fault conditions that may damage the motor.

List of the sensors that can be used to feedback information to a microcontroller are listed below:

- Current sensors
  - Shunt resistor
  - Current-sensing transformer



- Hall effect current sensor
- Speed/position sensors
  - Quadrature encoder
  - Hall effect tachometer
- Back EMF/Sensorless control method

### 8.3.5.2 Current sensors

The three most popular current sensors in motor control applications are:

- Shunt resistors
- Hall effect sensors
- Current transformers

Shunt resistors are popular current sensors because they provide an accurate measurement at a low cost. Hall effect current sensors are widely used because they provide a non-intrusive measurement and are available in a small IC package that combines the sensor and signal-conditioning circuit. Current-sensing transformers are also a popular sensor technology, especially in high-current or AC line-monitoring applications. A summary of the advantages and disadvantages of each of the current sensors is provided in Table 8.5.

**Table 8.5: Current feedback schemes.**

Current Sensing Method	Shunt Resistor	Hall Effect	Current Sensing Transformer
Accuracy	Good	Good	Medium
Accuracy vs. Temperature	Good	Poor	Good
Cost	Low	High	Medium
Isolation	No	Yes	Yes
High Current-Measuring Capability	Poor	Good	Good
DC Offset Problem	Yes	No	No
Saturation/Hysteresis Problem	No	Yes	Yes
Power Consumption	High	Low	Low
Intrusive Measurement	Yes	No	No
AC/DC Measurements	Both	Both	Only AC

Fig. 8.13 shows an example of an AC motor powered by a three-phase inverter bridge circuit. This example shows that the composite current of all three Insulated Gate Bipolar Transistor (IGBT) circuit legs can be measured with a single shunt resistor, or that the current in each individual leg can be determined with three shunt resistors. Fig.

8.13 shows a system that uses shunt resistors. However, Hall effect and current sensing transformers can also be used to provide the current measurement.

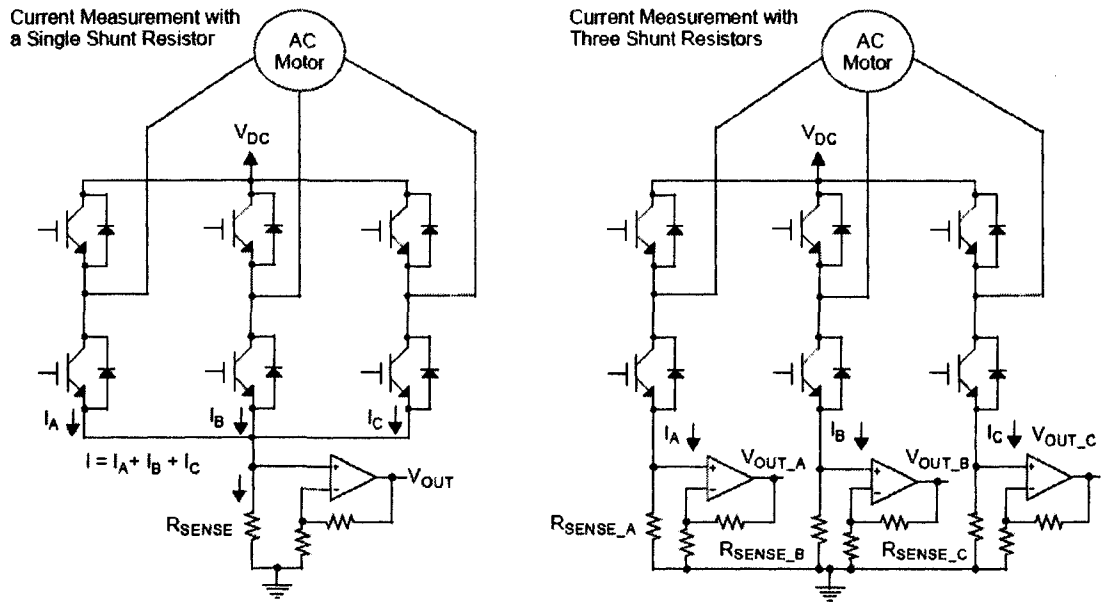


Fig. 8.13: Shunt resistors as current feedback sensors.

### 8.3.5.3 Shunt Resistors

Shunt resistors are a popular current-sensing sensor because of their low cost and good accuracy. The voltage drop across a known low value resistor is monitored in order to determine the current flowing through the load. If the resistor is small in magnitude, the voltage drop will be small and the measurement will not have a major effect on the motor circuit. The power dissipation of the resistance makes current shunts impractical for measurements of more than approximately 20 amperes.

The selection criteria of a shunt current resistor requires the evaluation of several trade-offs, including:

- Increasing  $R_{\text{SENSE}}$  increases the  $V_{\text{SENSE}}$  voltage, which makes the voltage offset ( $V_{\text{OS}}$ ) and input bias current offset ( $I_{\text{OS}}$ ) amplifier errors less significant.
- A large  $R_{\text{SENSE}}$  value causes a voltage loss and a reduction in the power efficiency due to the  $I^2 \times R$  loss of the resistor.

- A large  $R_{\text{SENSE}}$  value will cause a voltage offset to the load in a low-side measurement that may impact the EMI characteristics and noise sensitivity of the system.
- Special-purpose, low inductance resistors are required if the current has a high frequency content.
- The power rating of  $R_{\text{SENSE}}$  must be evaluated because the  $I^2 \times R$  power dissipation can produce self heating and a change in the nominal resistance of the shunt.

Special-purpose, shunt current measurement resistors are available from a number of vendors. If standard resistors are used, it is recommended that metal-film resistors be used rather than wire-wound resistors that have a relatively large inductance.

#### **8.3.5.4 Quadrature Encoder**

A quadrature encoder can be used to provide the speed, direction and shaft position of a rotating motor. A simplified block diagram of an optical quadrature encoder is shown in Fig 8.14. The typical quadrature encoder is packaged inside the motor assembly and provides three logic-level signals that can be directly connected to the microcontroller.

Motor speed is determined by the frequency of the Channel A and B signals. Note that the counts-per-revolution (CPR) depends on the location of the encoder and whether motor-gearing is used. The phase relationship between Channel A and B can be used to determine if the motor is turning in either a forward or reverse direction. The Index signal provides the position of the motor and, typically, a single pulse is generated for every 360 degrees of shaft rotation.

The quadrature encoder's speed and direction information can be determined either with discrete logic, a quadrature encoder logic IC or a PICmicro® microcontroller. A quadrature encoder with 36 positions is used with a truth table as shown in Table 8.6.

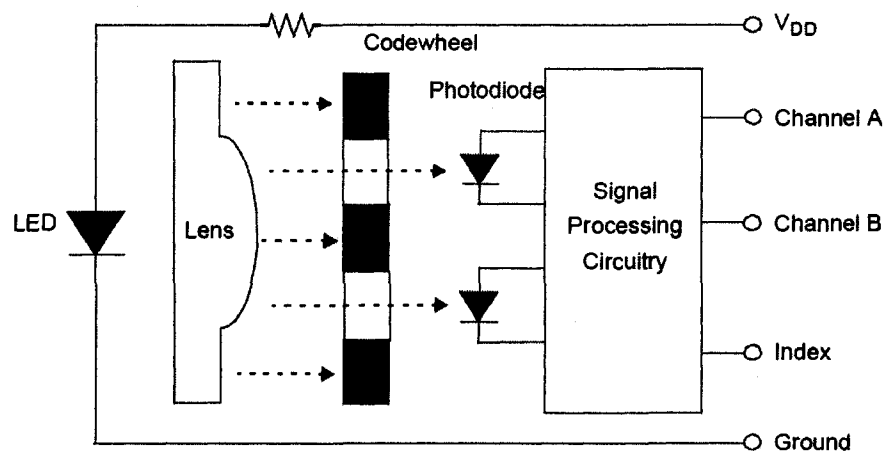
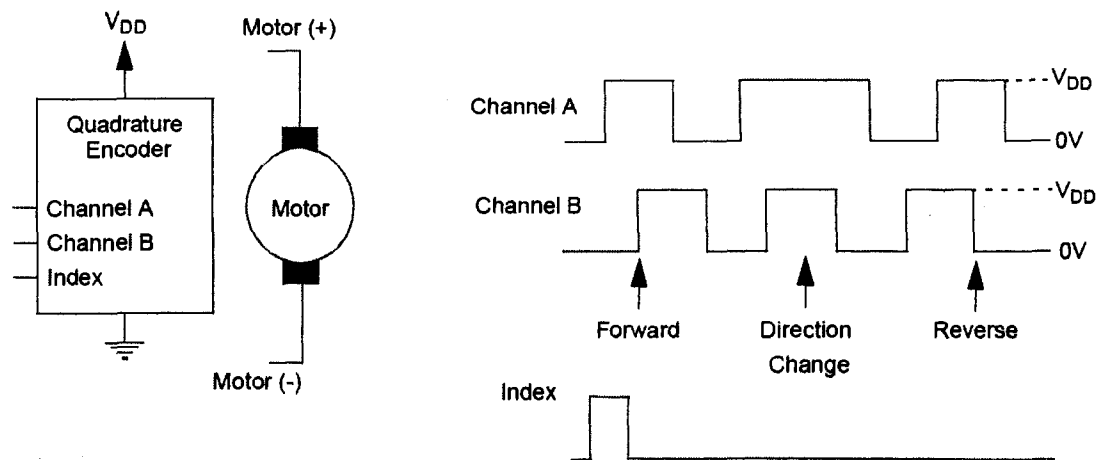


Fig. 8.14: Simplified block diagram of quadrature encoder.

Table 8.6: Quadrature encoder truth table.

Clockwise Rotation		
Quadrature 2-Bit Code 1/4 Cycle per Detent		
Switch Position	Output	
	"A"	"B"
1		
2	•	
3	•	•
4		•
5		
6	•	
7	•	•
8		•
9		
10	•	
11	•	•
12		•
13		
14	•	
15	•	•
16		•
17		
18	•	
19	•	•
20		•
21		
22	•	
23	•	•
24		•
25		
26	•	
27	•	•
28		•
29		
30	•	
31	•	•
32		•
33		
34	•	
35	•	•
36		•

## 8.4 Putting it all together

After selecting the components, the next stage is to build the circuit and fabricate the printed circuit board (PCB). Several programs are in the market that can perform this task including OrCAD®, Protel and Altium Designer. I used Altium Designer for its powerful capabilities in designing the routes and massive components' library.

After drawing the circuit in the schematic section and choosing the footprint of each component, these components are exported to the PCB layout section where the user can place them or the program can suggest the placement depending on a certain criteria. Then, the program can auto-route the PCB or the user can manually place the routes. The circuit schematic as designed in Altium Designer is shown in Fig 8.15. and the final two-layer PCB is shown in Fig. 8.16.



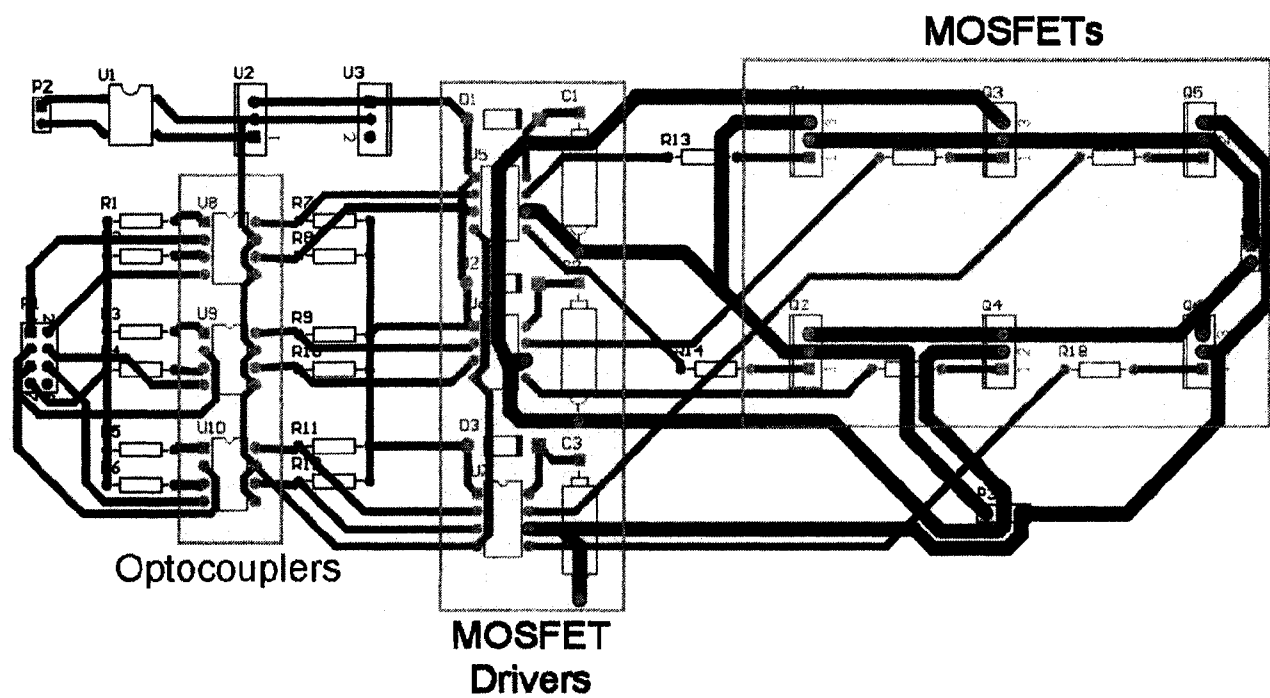


Fig. 8.16: PCB layout of the developed power electronic converter.

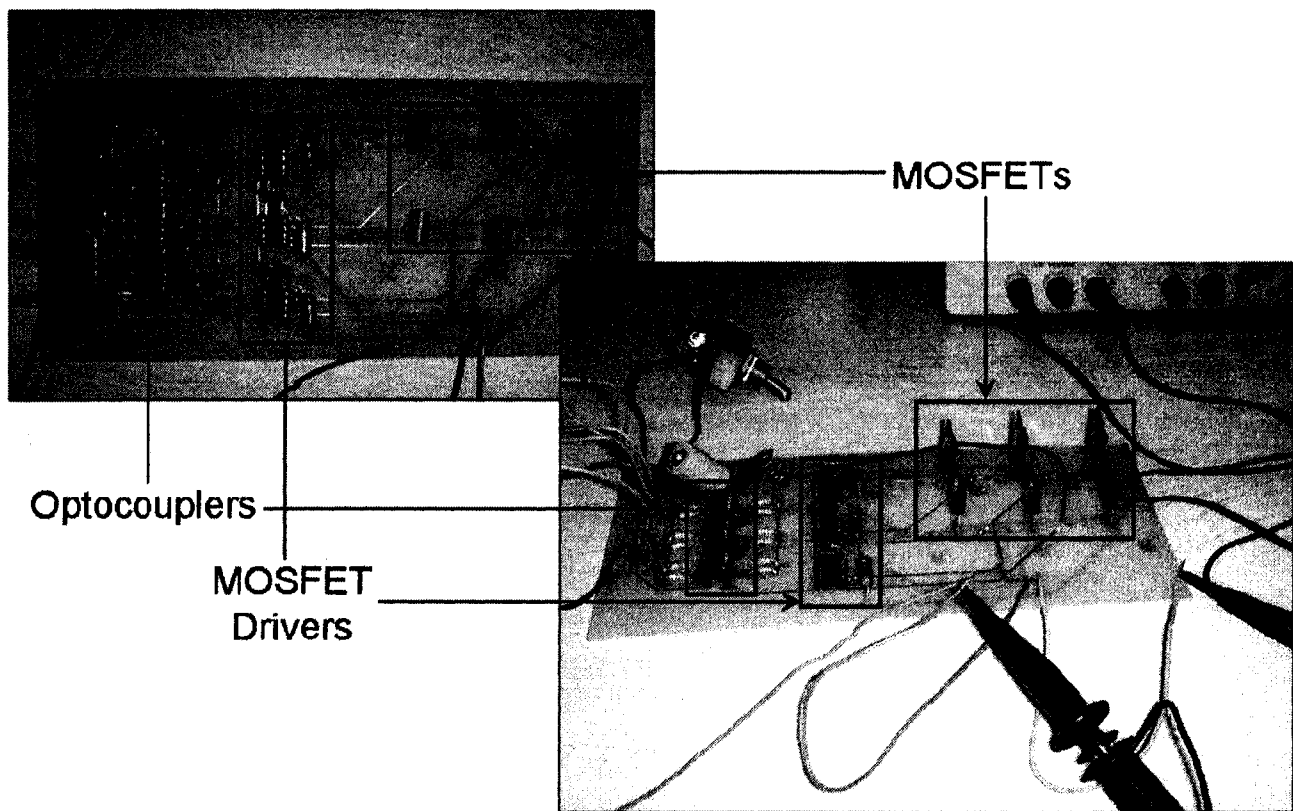


Fig. 8.17: Completed power electronic converter.



The PCB was fabricated and the components were soldered in place as shown in Fig. 8.17. Then the board was tested. The output of the 3 phase PWM inverter is shown in Fig. 8.18-8.21.

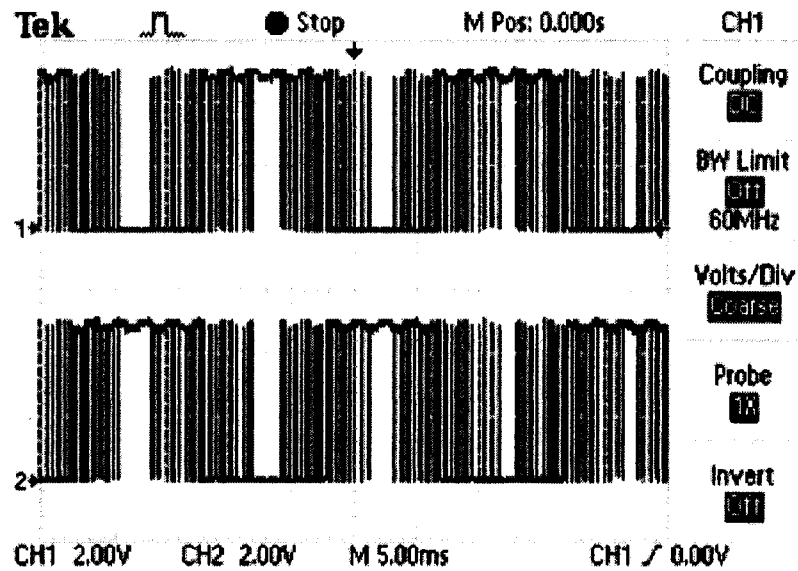


Fig. 8.18: PWM complementary output.

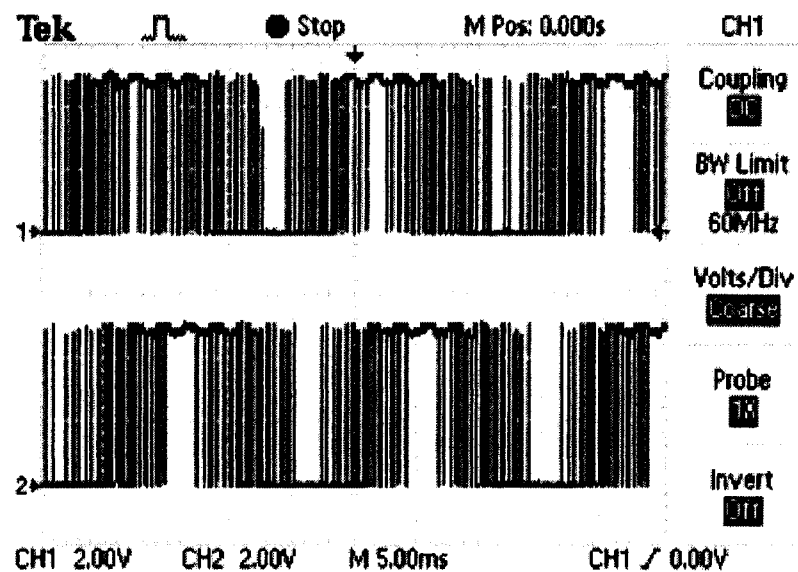


Fig. 8.19: PWM outputs shifted 120°.

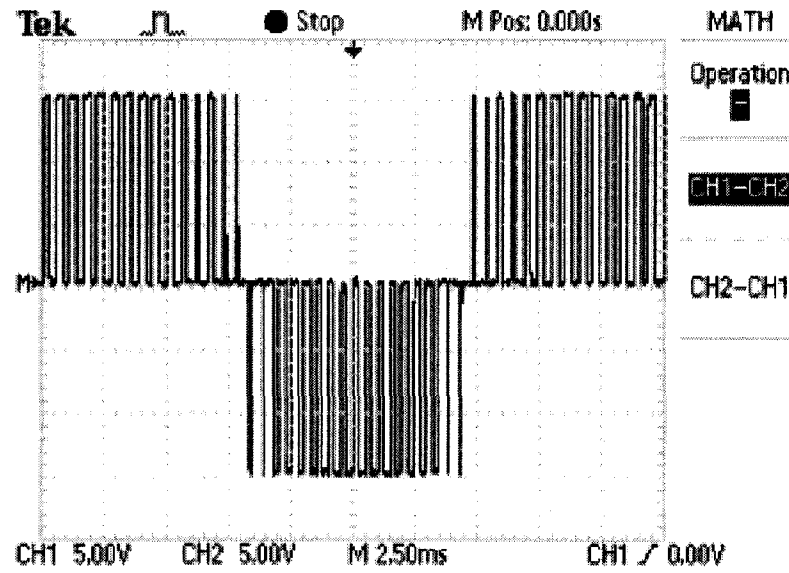


Fig. 8.20: Output line voltage for resistive load.

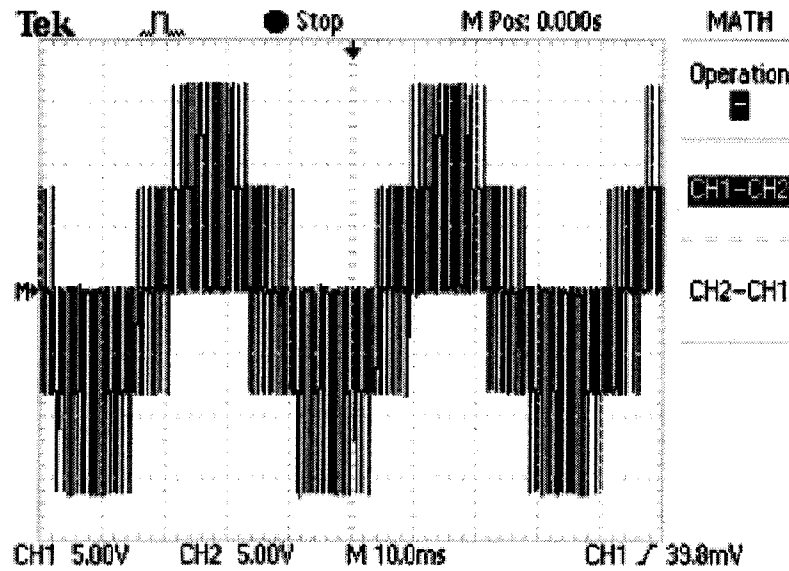


Fig. 8.21: Output phase voltage for resistive load.

## 8.5 Experimental results

The main objective is to validate the simulation results obtained in the previous chapters as well as to investigate the performance of the DFIG when using the different controllers. The controllers considered are those demonstrated in the previous chapters, namely, adaptive, fuzzy, and neuro-fuzzy. As shown in chapter 4, the exponential gain scheduler gave the best performance so it is the one considered for the adaptive gain

scheduler. For comparison, the performance of the above mentioned controllers is compared to the conventional PI controller with constant gains. The conventional PI controller has a proportional gain of 45 and an integral gain of 22.5.

All the stator and rotor currents are experimentally measured and recorded using Tektronix TDS1002 digital storage oscilloscope. The sampling frequency is 1.25 kHz. The microcontroller was programmed to perform the controller tasks and to calculate the gains depending on the control scheme whether it is a conventional PI, adaptive, fuzzy or neuro-fuzzy.

Numerous scenarios were considered and for illustration purposes two were chosen and will be demonstrated. The first scenario investigates the sub-synchronous operation of the DFIG with different controllers while the second scenario investigates the super-synchronous operation.

For the first scenario, speed changes from 1200 rpm to 1400 rpm. The resulting speed change for each controller is illustrated in Fig.8.22. It can be seen that conventional PI controller with constant gain has a rise time of 2.8s with 2% overshoot and 1.5% steady-state error while the adaptive PI gain scheduler employing the exponential characteristic has a rise time of 2.5s and a settling time of 6s with 1% overshoot and no steady-state error. On the other hand, the fuzzy PI gain scheduler has a rise time of 2s and a settling time of 3s with no overshoot and no steady-state error while the neuro-fuzzy PI gain scheduler has a rise time of 1.5s and a settling time of 2.8s with no overshoot and no steady-state error. These results are summarized in Table 8.7.

For the same scenario, the change in speed increased the stator active power production from 780W to 960W while the reactive power produced is kept constant at 800VARs. This increase in power production increased the stator current as shown in Fig. 8.23. At the rotor side, this increase in speed changed the rotor line and phase voltages as well as the rotor current as shown in Figs. 8.24 – 8.26 respectively.

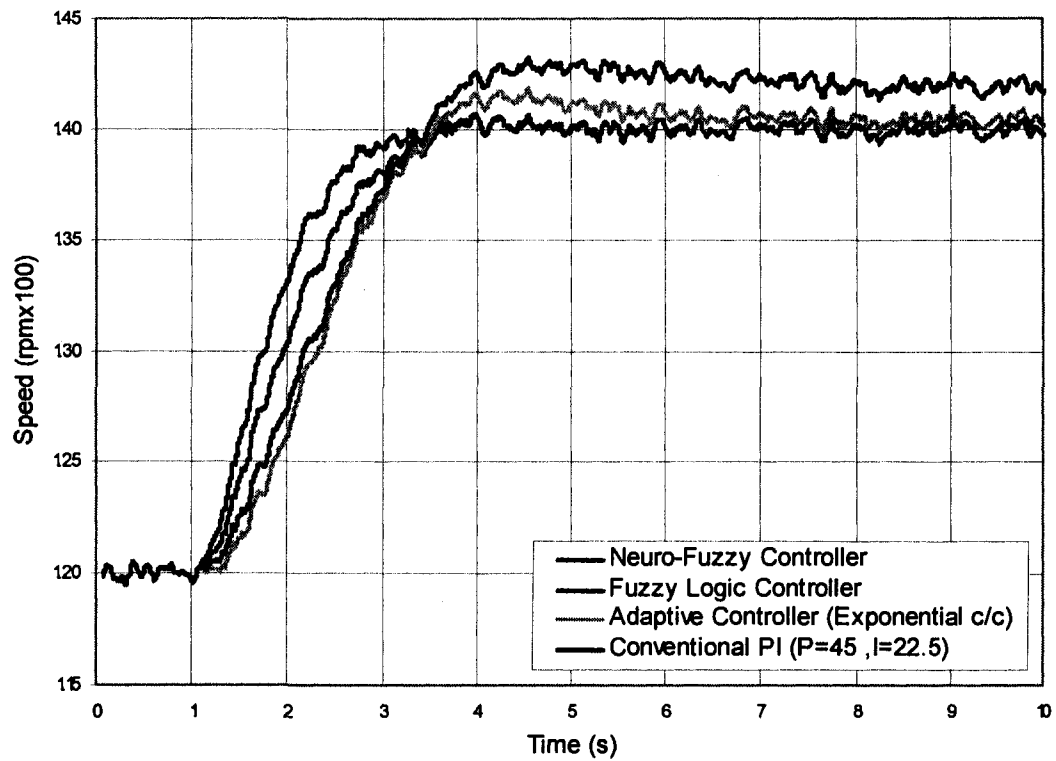
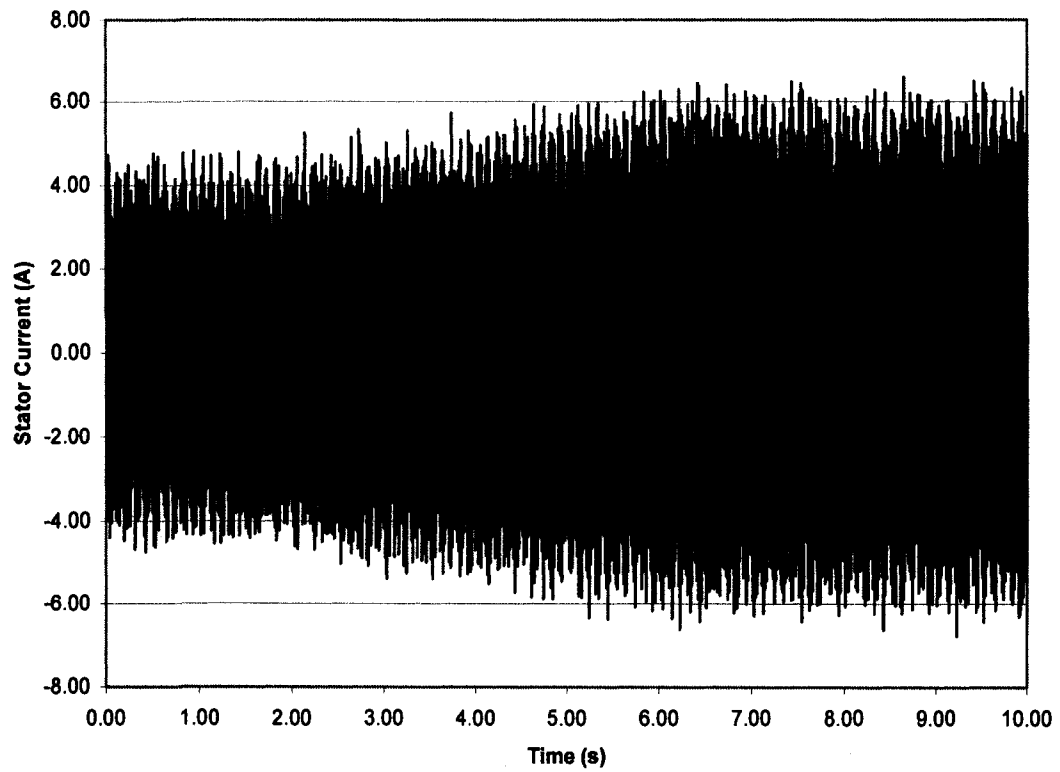


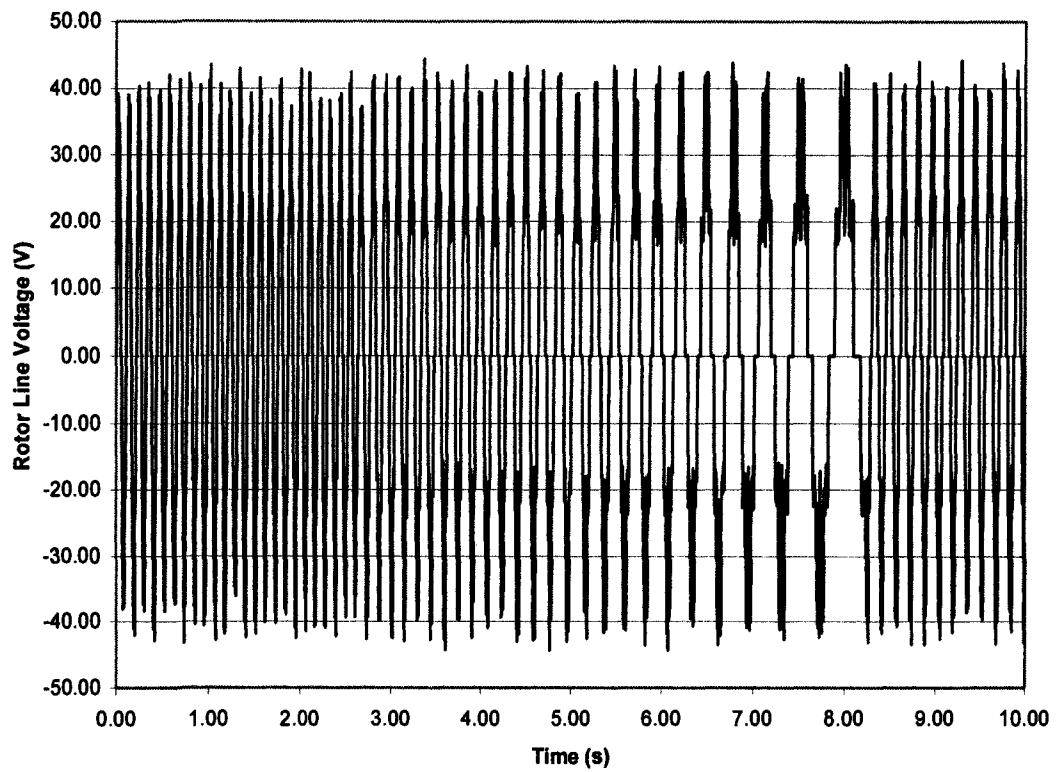
Fig. 8.22: Speed response for sub-synchronous operation.

Table 8.7: Controllers' performance for sub-synchronous operation.

Controller	Rise time (s)	Settling time (s)	Overshoot (%)	S.S. error (%)
Conv. PI	2.8	$\infty$	2	1.5
Adaptive	2.5	6	1	0
Fuzzy Logic	2	3	0	0
Neuro-Fuzzy	1.5	2.8	0	0



**Fig. 8.23: Stator current for sub-synchronous operation.**



**Fig. 8.24: Rotor line voltage for sub-synchronous operation.**

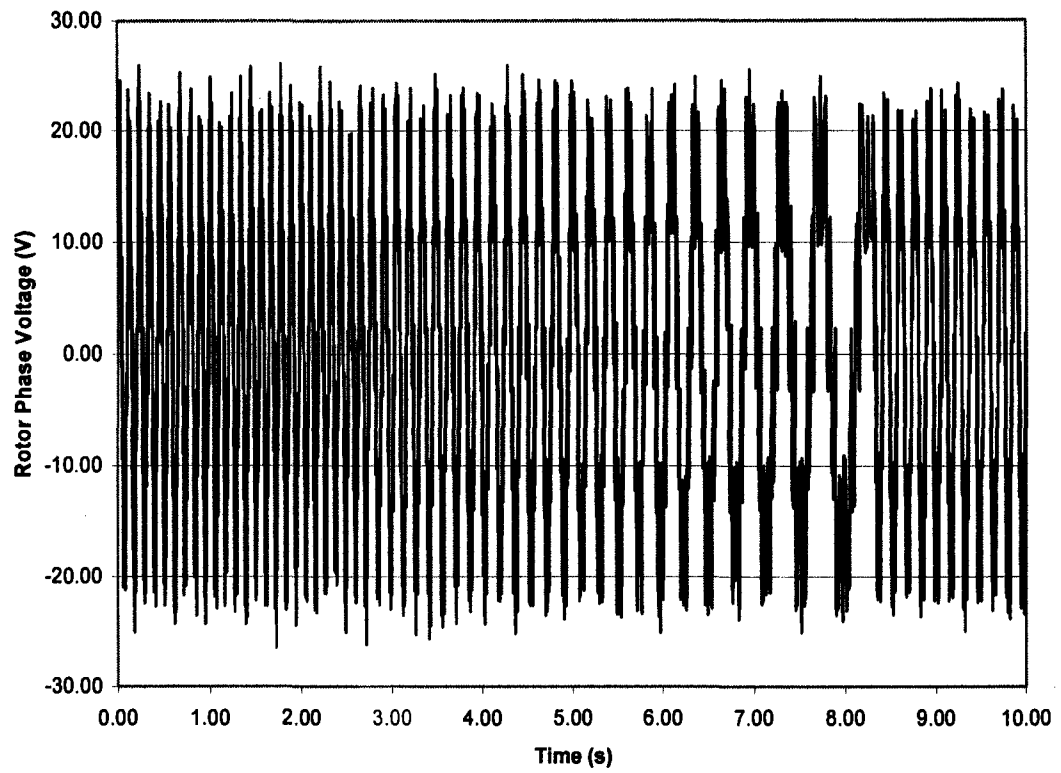


**Fig. 8.25: Rotor phase voltage for sub-synchronous operation.**

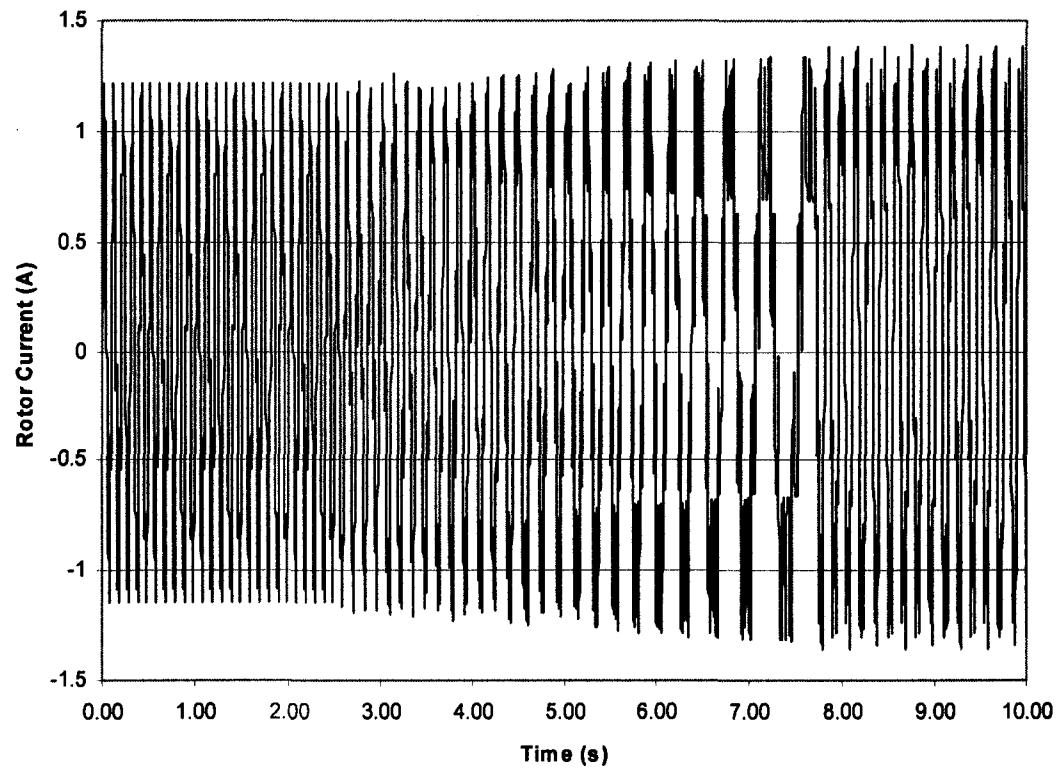


**Fig. 8.26: Rotor current for sub-synchronous operation.**

In the second scenario, the speed changes from 1600 rpm to 1900 rpm. The resulting speed change for each controller is illustrated in Fig.8.27. It can be seen that conventional PI controller with constant gain has a rise time of 3.8s and a settling time of 4.5s with no overshoot and no steady-state error which is the same performance achieved by the adaptive PI gain scheduler employing the exponential characteristic. On the other hand, the fuzzy PI gain scheduler has a rise time of 2.5s and a settling time of 4.5s with 0.6% overshoot and no steady-state error while the neuro-fuzzy PI gain scheduler has a rise time of 2.8s and a settling time of 4.5s with no overshoot and no steady-state error. These results are summarized in Table 8.8.

For the same scenario, the change in speed increased the stator active power production from 1320W to 1860W while the reactive power produced is kept constant at 1000VARs. This increase in power production increased the stator current as shown in Fig. 8.28. At the rotor side, this increase in speed changed the rotor line and phase voltages as well as the rotor current as shown in Figs. 8.29 – 8.31 respectively.

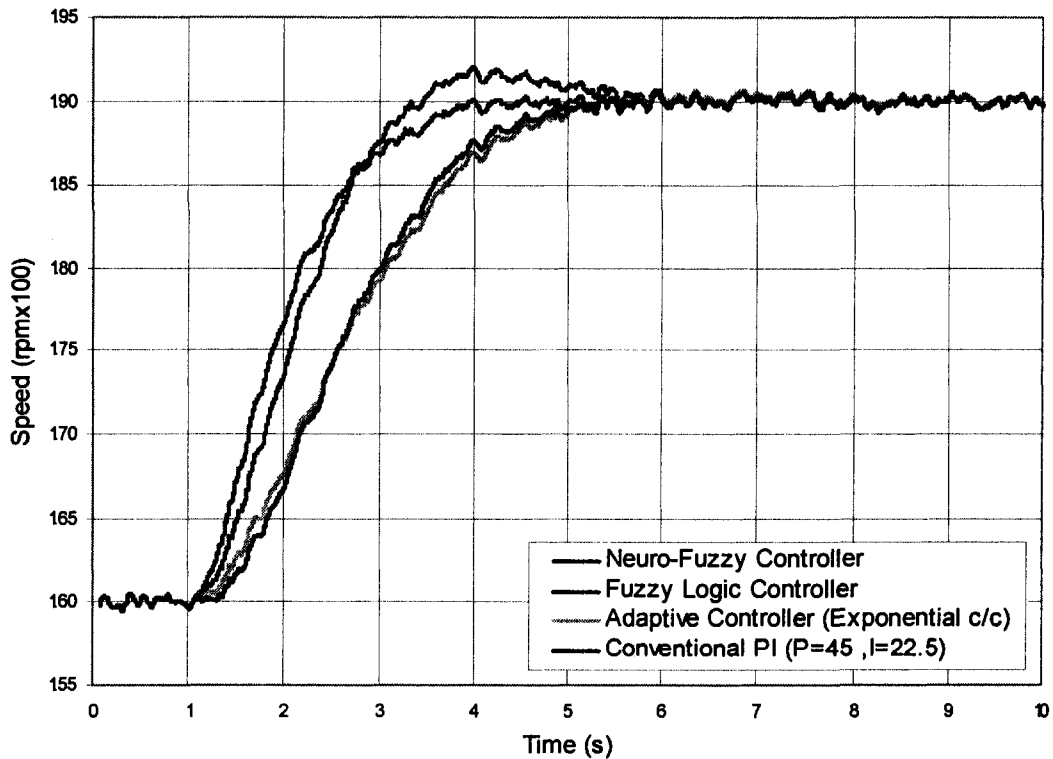
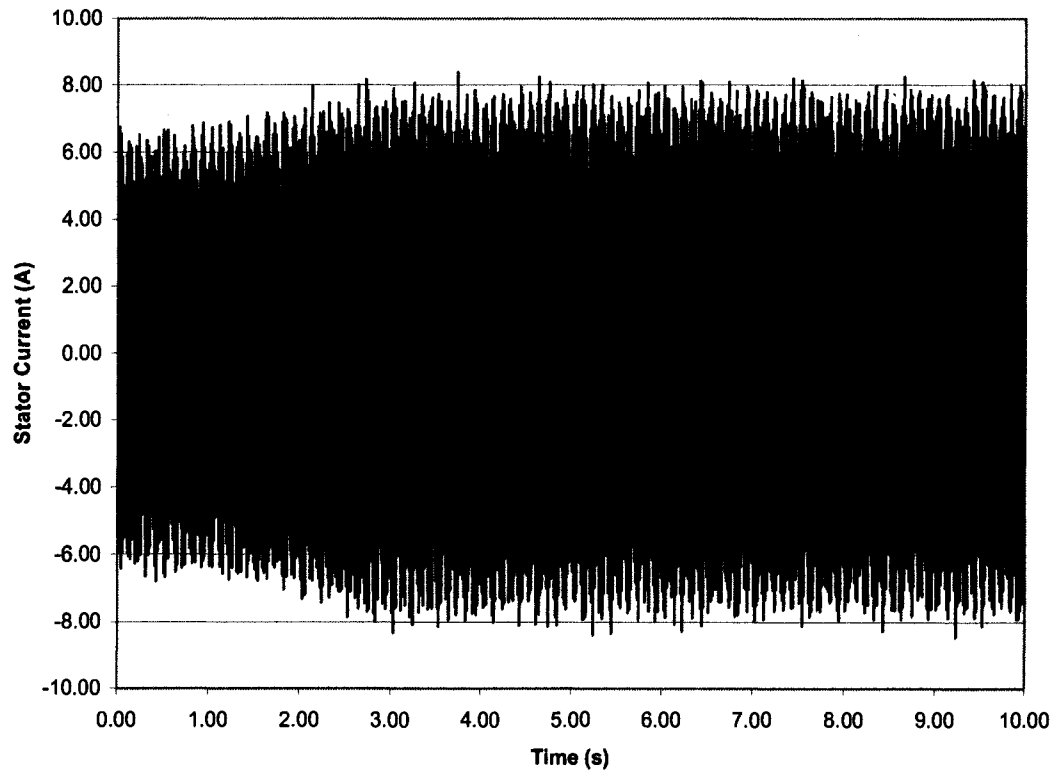


Fig.8.27: Speed response for super-synchronous operation.

**Table 8.8: Controllers' performance for super-synchronous operation.**

Controller	Rise time (s)	Settling time (s)	Overshoot (%)	S.S. error
Conv. PI	3.8	4.5	0	0
Adaptive	3.8	4.5	0	0
Fuzzy Logic	2.5	4.5	0.6	0
Neuro-Fuzzy	2.8	4.5	0	0



**Fig. 8.28: Stator current for super-synchronous operation.**



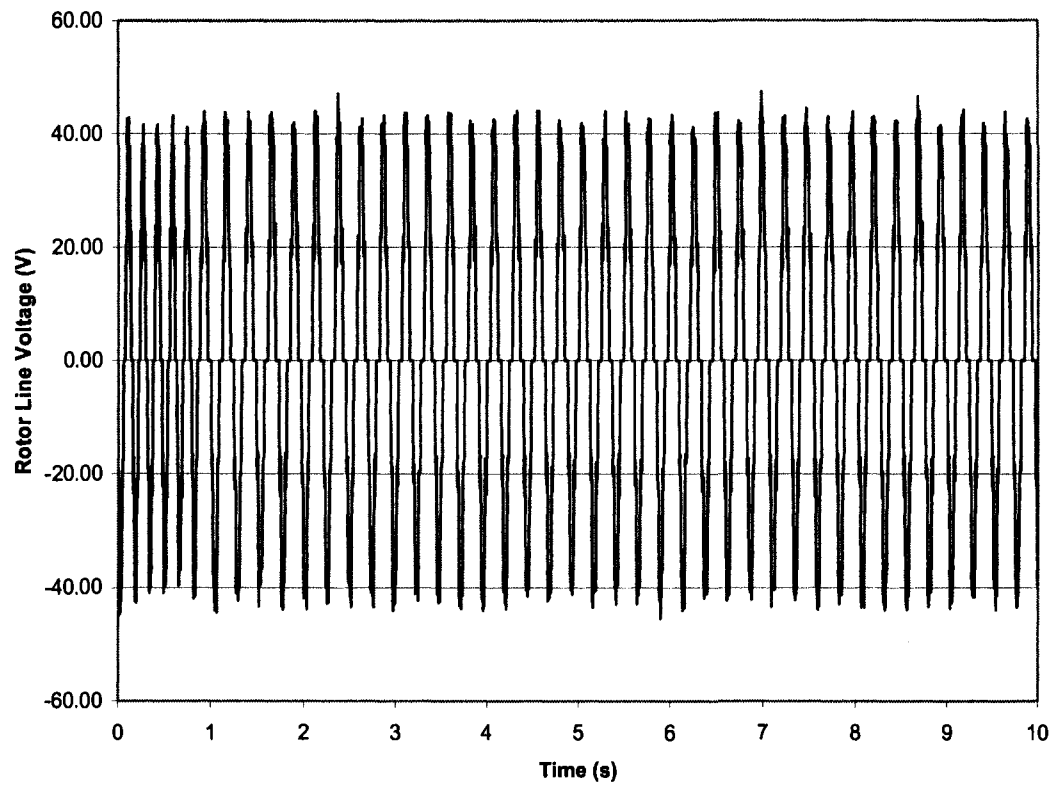


**Fig. 8.29: Rotor line voltage for super-synchronous operation.**

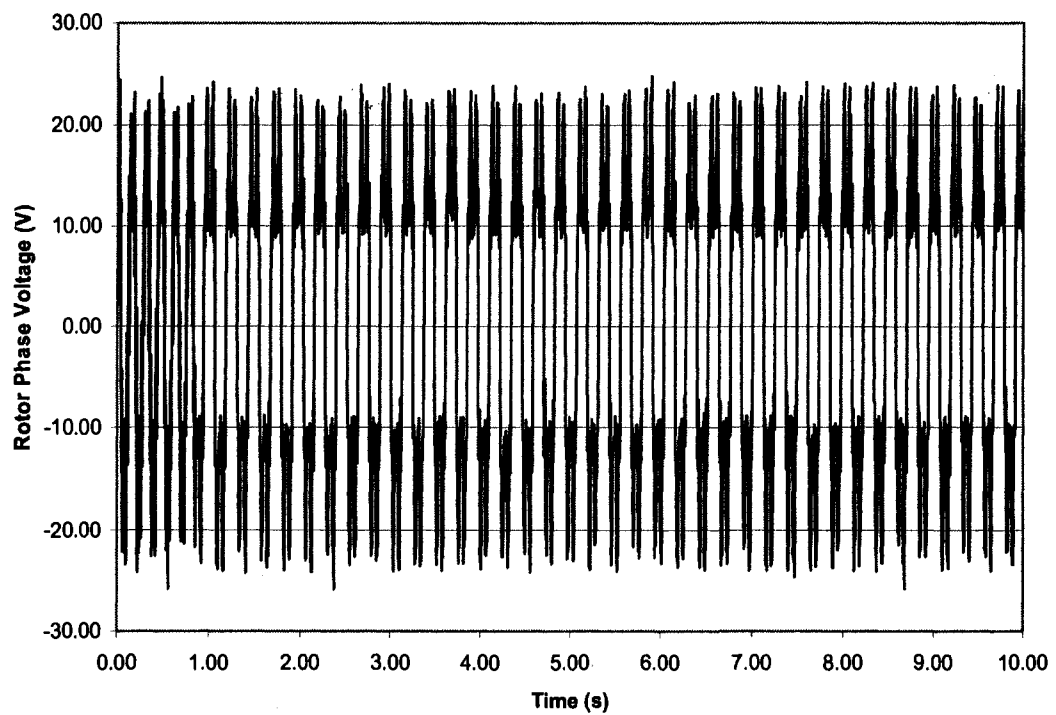


**Fig. 8.30: Rotor phase voltage for super-synchronous operation.**

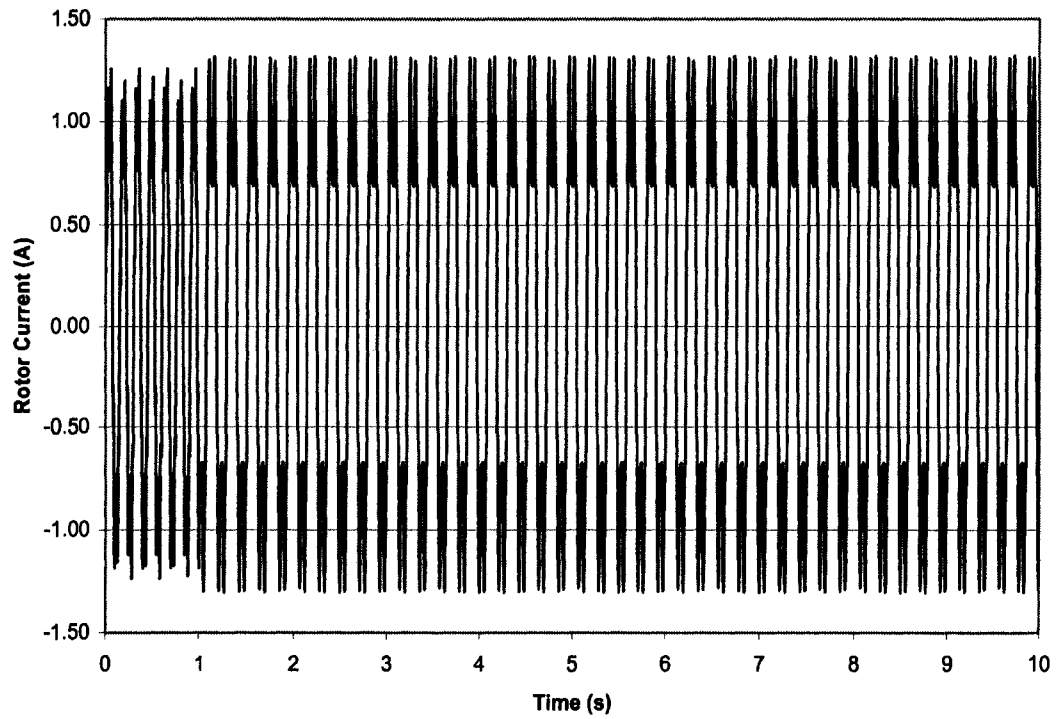


**Fig. 8.31: Rotor current for super-synchronous operation.**

## **8.6 References**

- [1] *IEEE Standard Test Procedure for Polyphase Induction Motors and Generators*, IEEE Standard 112-2004, 2004.

## **9 Conclusion and Future Work**

### **9.1 Conclusion**

This work represents contributions in different areas all related to the wind power and the increase interest in using DFIG in this particular field. First, the machine is modeled. Then, a more accurate model is developed which considers the saturation in the main and leakage flux paths. This model proves to be more realistic in simulating and predicting the machine behavior. Based on this model, three conference and one journal paper are published. Second, the wind driven DFIG system is build. Different control techniques are used and investigated. In the beginning, the adaptive control technique was employed then fuzzy logic and finally neuro-fuzzy. The results of each have been published in either a conference or journal papers. Based on these control techniques, two conference and one journal paper are published. Finally, an experimental setup was built, the process of selecting the components and the steps of building this experimental setup was discussed in details in chapter 8. The control techniques considered in the simulation investigations were employed practically through the programming of the microcontroller. The experimental results showed that:

- The developed machine model is accurate in predicting machine behavior under transient conditions.
- Vector control technique when applied at the rotor side of the DFIG is extremely efficient in controlling the machine generated active and reactive power.
- Vector control technique can be applied at the rotor side of the DFIG to control the machine speed and track the maximum power point curve.
- The tracking of the maximum power point curve maximizes the annual power production of the turbine.
- Applying the control scheme at the rotor circuit has several advantages.

- The control techniques considered in this work definitely gives better performance than the conventional PI controller with fixed gains.
- The complexity of the control system increases from adaptive control, fuzzy logic to neuro-fuzzy. As the complexity of the control technique increases, better performance is obtained.
- The system developer should balance the control performance required and the complexity of implementing, programming and tuning the control system.

## **9.2 Future work**

Wind turbines and wind farms are usually located in remote locations. This arises a whole set of problems facing the operation and the maintenance of wind farms.

The work presented here will be the basis to expand the research in wind power in different areas. Suggested future research areas are:

- Developing a monitoring system capable of predicting the failure in the major electrical components and preventing them.
- Developing a technique that employ an intelligent system which is capable of protecting the electrical system of the turbine based on current and voltage waveforms.
- Investigate the effect of mechanical system failures on the current and voltage waveforms.
- Based on the previous investigation, a novel protection technique may be developed to predict, prevent and pinpoint the location of mechanical failures.
- Improve the performance of the voltage source inverter by investigating new switching schemes such as space vector modulation and new converter topologies such as multi-level converters.

## 10 Vita Auctoris

<b>Name</b>	Hany Mohamed Abdullah Jabr Soloumah
<b>Place of Birth</b>	Alexandria, Egypt
<b>Year of Birth</b>	1978
<b>Education</b>	<i>Alexandria University, Egypt</i> 1995-2000 B.Sc. Honors <i>Alexandria University, Egypt</i> 2000-2003 M.Sc. <i>University of Windsor, Windsor, Ontario</i> 2004-2008 Ph.D.